POLITECNICO DI MILANO
School of Industrial and Information Engineering
Master of Science in Energy Engineering

PRELIMINARY MODELLING OF HYDROGEN PEMFC SYSTEM FOR AUTOMOTIVE APPLICATIONS FOCUSING ON AIR LOOP

Advisor:
Prof. Andrea Baricci
Co-Advisor:
Ing. Amedeo Grimaldi

Candidates:
Garancini Tommaso 875356
Montauti Marianna 875346

Academic Year 2018/2019

Acknowledgement

Abstract

Fuel cell systems represent a clean and efficient alternative to traditional ICEs for automotive application and an intensive research is under development by academia and manufacturers to make this technology competitive in the incoming years. Many issues still affect the spread of this technology, which can be summarised into degradation and cost issues. The overcome of these criticisms depends on understanding, predicting and controlling the behaviour of the fuel cell systems under fast transients of operating and load conditions. Many lumped parameters-based models of FC systems are currently available. They are based on semi-empirical relations which model fuel cell performance dependence on operating parameters. Very few system-level models extend their analysis to a deeper understanding of species transport within the component during operation. The aim of this work is to develop an innovative physical-based PEM fuel cell model to incorporate within the PEM system for automotive application, which allows to investigate the main transport mechanisms occurring inside the cell. Cathode and anode kinetics, gas species transport through the cathode GDL, mass transport through anode and cathode channels and water transport through the membrane are the main phenomena investigated. A physical, dynamic, 1D+1D, non-isothermal model has been implemented in Matlab-SIMULINK environment, to capture the transient behaviour of the cell. Air management, water management and thermal management system components are developed from semi-empirical components model. A comparison of two control approaches is reported, which aims to assess whether keeping stack pressure constant or variable is the best alternative in terms of water management and overall efficiency, when the system replicates a NEDC cycle.

KEY WORDS: PEMFC system, dynamic model, SIMULINK, air loop subsystem.

Sommario

I sistemi a celle a combustibile rappresentano un'alternativa pulita ed efficiente ai tradizionali motori a combustione interna per applicazioni automobilistiche. Un'intensa attività di ricerca è in fase di sviluppo da parte di università e produttori per rendere questa tecnologia competitiva negli anni a venire. Molte criticità incidono ancora sulla diffusione di questa tecnologia, che può essere riassunta in termini di degradazione e costo. Il superamento di questi problemi dipende dalla comprensione, dalla previsione e dal controllo del comportamento del sistema quando quest'ultimo è sottoposto a transitori di carico molto rapidi, tipico di applicazioni automotive. Al momento sono disponibili in Letteratura molti modelli a parametri concentrati di sistemi cella a combustibile. Si basano su relazioni semi-empiriche della cella che modellano la dipendenza dalle prestazioni del componente sui parametri operativi. Pochissimi modelli a livello di sistema estendono la loro analisi a una più profonda comprensione del trasporto delle singole specie all'interno della cella durante il funzionamento. Lo scopo di questo lavoro è quello di sviluppare un modello di cella a combustibile PEM basato sulla fisica da incorporare all'interno del sistema PEM per applicazioni automobilistiche. Esso consente di indagare i principali meccanismi di trasporto che si verificano durante un tipico funzionamento automotive. Cinetica catodica e anodica, trasporto di specie gassose attraverso il catodo GDL, trasporto di massa attraverso canali anodi e catodici e trasporto dell'acqua attraverso la membrana sono i principali fenomeni investigati. Un modello fisico, dinamico, 1D + 1D, non isotermico è stato implementato nell'ambiente Matlab-SIMULINK, per comprendere il comportamento transitorio. I componenti del sistema di compressione e umidificazione dell'aria e raffreddamento dello stack sono stati sviluppati partendo da modelli semi-empirici dei singoli componenti. Viene infine presentato un confronto tra due approcci di controllo, che mira a valutare quale, tra un controllo sulla Pressione a un valore costante o una variazione lineare della stessa con la potenza, è la migliore alternativa in termini di controllo del livello di umidificazione in membrana e di efficienza a livello di sistema, quando questo replica un ciclo NEDC.

Extended Abstract

INTRODUCTION

Global warming and air pollution in urban areas issues faced the necessity to move towards clean, environmentally friendly power sources. Transport sector is critical as it is responsible for 30% of global emissions. In this context, proton exchange membrane fuel cell is considered as one of the most promising alternatives to traditional internal combustion engines thanks to its high-power density, low temperature operation, fast start-up and low emissions. Automobile PEMFC constantly experience transient load conditions. Thus, it is important to investigate their principal dynamic mechanisms to understand the voltage response to load changes. *Pukrushpan et al.* developed a nonlinear fuel cell system dynamic model suitable for control study. The attention has been mainly focused on the air control management subsystem, while a lumped-parameter model has been developed to capture cell response to operating parameters variation. *Kang et Al.* developed a 1D dynamic model of a PEM fuel cell system for automotive application to investigate the dynamic response to current changes. The fuel cell stack is only discretized in the through-plane direction and it is therefore not able to capture variation along the in-flow direction.

The aim of this work is to develop a 1D+1D dynamic PEMFC system model with a focus on the air loop. The analysis has been organized starting from the main system component, i.e. the stack, with the aim to observe its peculiar phenomena and timescales, and through the addition of the other components of the air subsystem, trying to understand how they affect its performance, arriving, in the end, at the simulation of the global system, under a typical driving cycle**.**

MODEL DESCRIPTION

PEMFC stack

In this work, the cells are assumed to perform the same and can be lumped as a stack. The fuel cell model is an innovative 1D+1D, dynamic, non-isothermal model. The main transient phenomena investigated are mass transport of the species through anode and cathode channels in the in-flow direction and mass transport of species through GDL and membrane in the through-flow direction. For the membrane bot the drag and back diffusion mechanisms have been considered. Moreover, charge conservation equation including double layer effect has been considered in the catalyst layers. Channel volume, both at cathode and anode, has been divided into six layers to solve species distribution along the channels. Energy conservation equation has been solved per each layer. In addition, in order to investigate water species transport through the MEA, cathode GDL and membrane are discretized in 7x6 and 2x6 control volumes respectively. Each control volume is characterized by a single set of species activities, used to determine local operating features of the fuel cell. Control volumes are connected each other in the through-flow direction across MEA and along the channel direction to compute mass and species transport. Figure 1 shows a graphical representation of control volumes discretization.

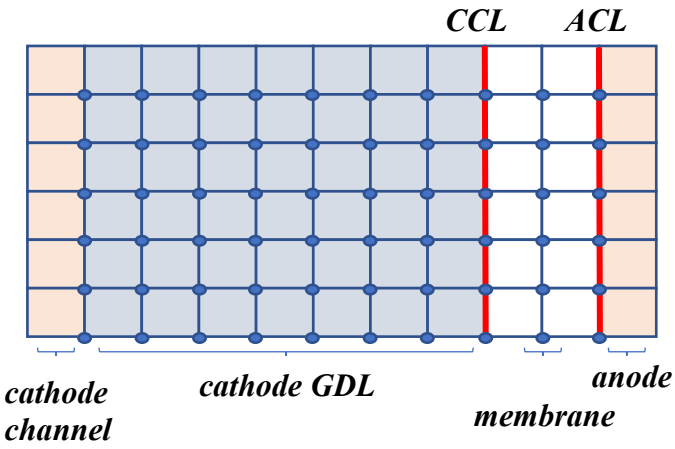

Figure 1 - Control volume discretization per each PEMFC unit

The main assumptions of the model are:

- Gas species are ideal gases;
- Liquid water saturation in the MEA has been neglected: water is assumed to be only in gaseous phase in the gas diffusion layer (GDL) and in dissolved phase in the membrane ionomer;
- Catalyst Layers, where the reactions occur, are interfaces;
- Micro porous layer has not been implemented: at cathode side the GDL is assumed to be directly in contact with the cathode catalyst layer.

MODEL VALIDATION

The stationary model has been validated on commercial cells of 25 cm^2, using Simulink *Parameter Estimation* toolbox. The GDL oxygen diffusion $D_{O2,GDL}$, the ORR kinetic constant Kr and the charge transfer coefficient α_{ORR} have been fitted so to reproduce the polarization curves for different inlet cathode RH, operating temperatures and pressures. Then, $D_{O2,GDL}$, as well as the geometric parameters, have been adjusted so to reach the performances of the automotive cells. The main results are shown below:

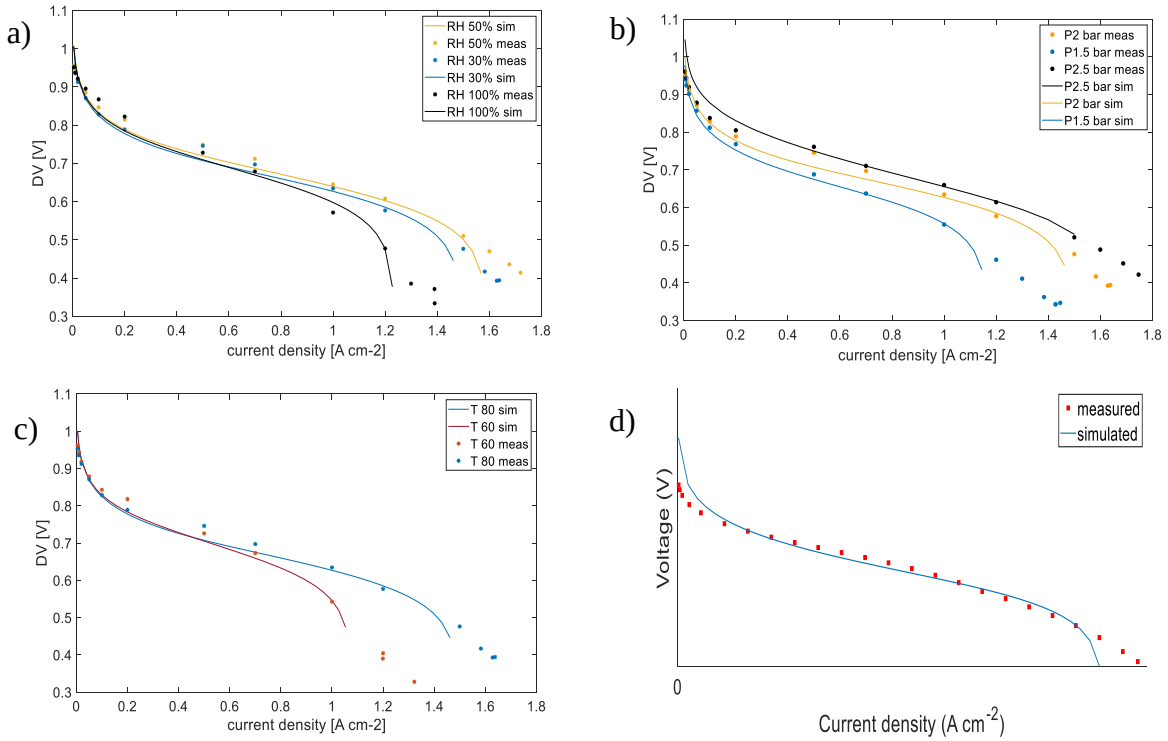

Figure 2 - Polarization curves fitting results at different RH (a), pressure(b), temperature(c), automotive curve(d)

PEMFC System

The dynamic model of PEMFC system includes the main balance of plant components of PEMFC systems for automotive application, schematically shown in Figure 2. The model consists of a compressor and a manifold system, which supply the required air to PEM stack. A plate-and-frame membrane humidifier allows the wet air out of the cathode side to humidify the dry air out of the supply manifold, before entering the cell. Thermal management system consists of a by-pass valve, a radiator and a fan. Proper control of the air inlet flow rate in the stack, pressure and coolant mass fraction entering the radiator has been implemented to meet performance requirements of the cell in automotive operation. Three main control loops have been used to regulate the air flow of the compressor, the

relative humidity and thermal cooling. Regulation is achieved by means of self-tuning PID controllers.

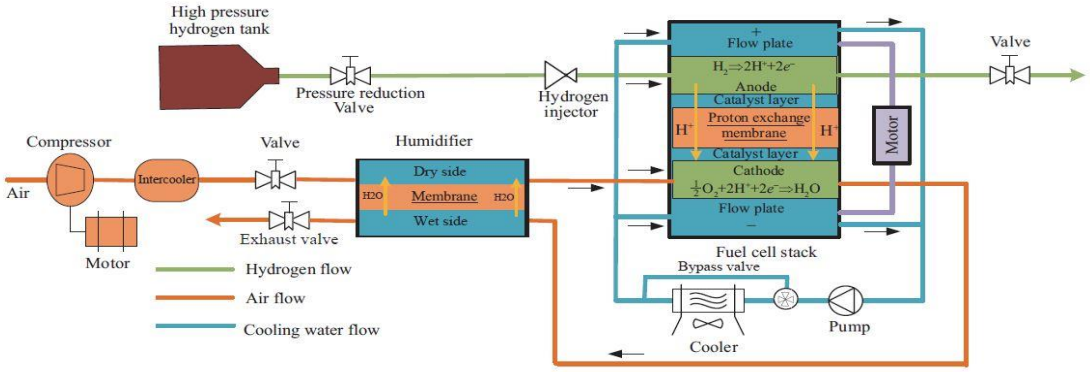

Figure 3 - PEMFC system scheme

BALANCE OF PLANT

The air supply system consists of air compressor and manifolds between the components. The compressor supplies the desired air flow rate to stack and, together with the back-pressure valve, it allows to increase air pressure which could lead to an improvement of the overall efficiency and power density of the FC stack. In this work, an expander is not included. The supply manifold lumps all the volumes associated with pipes and connections between the compressor and the stack, while the return manifold lumps volume of pipes at the outlet side of the stack.

Compressor Model. The compressor model is composed by two parts:

- a static compressor map, used to determine compressor efficiency, the air flow rate and the compressor ratio. Jensen & Kristensen method is used to model the compressor flow characteristic $W_{cp} = f(\omega_{cp}, \beta)$.
- A lumped rotational model is used to determine the dynamic behaviour of the compressor:

$$J_{cp}\frac{d\omega_{cp}}{dt} = (\tau_{cm} - \tau_{cp})$$

where τ_{cm} is the compressor motor torque and τ_{cp} is the load torque. The model proposed by Pukrushpan et Al. has been adopted. The power required by the compressor is calculated as:

$$P_{compr} = \dot{m}_{cp} c_{p,air} T_{cp,in}\left(\beta^{\frac{\gamma-1}{\gamma}} - 1\right)$$

Manifolds Model. The manifold model solves, both for the supply and the return manifolds, the mass conservation equation and the energy conservation equation.

The flow, exiting the supply manifold, is calculated by using a linear nuzzle flow equation, while regarding the return manifold, instead, the nonlinear nozzle equation is used to calculate the return manifold exit flow, as a function of the return manifold pressure and back-pressure valve opening area.

Temperature of the air, coming out from the supply manifold, is usually high due to increased pressure. It must be cooled down to prevent a damage in the FC membrane, through an intercooler, that has been assumed to cool down air to a temperature, lower than 80 °C, thus not to damage membrane.

Humidifier Model. A dynamic operating humidifier is needed to humidify the inlet air to the desired relative humidity before entering the stack. The water through the humidifier is assumed to be in vapour form. A plate-and-frame membrane humidifier has been used, with 35 channels per plate and 90 plates. A single *wet channel-membrane-dry channel* has been selected as a reference control volume (Figure 4). A lumped model has been implemented to calculate the amount of water transferred through the membrane, having as inlet flow rates the wet air exiting the stack for the wet side inlet and dry air exiting the compressor for the dry side inlet. In the ionomer control volume, the diffusion equation has been solved, while in the channels mass conservation equation and energy conservation equation have been implemented. An overall heat transfer coefficient has been estimated to quantify the heat transferred from the hot (wet) side to the cold (dry) side, considering that heat is transferred mainly by conduction in the membrane and convection through the channels.

Figure 4 - Humidifier control volume

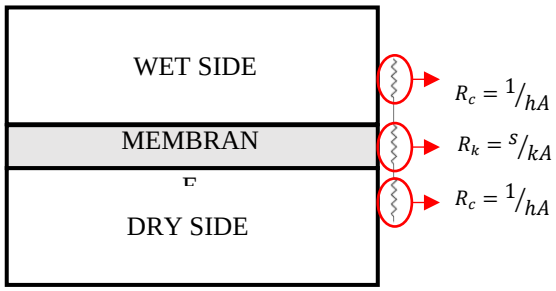

Radiator Model. The liquid radiator has been modelled as a one-dimensional crossflow louvered fin heat exchanger, the hot side is the coolant exiting the stack, while the cold side is forced air at ambient temperature. Jung and Assanis approach has been adopted.

Vehicle air flow and fan model. The vehicle air flow is modelled following the approach proposed by N-S-Ap, based on the pressure coefficients method. It computes the fan velocity, which is used to determine the velocity of air entering the radiator, used to define the heat transfer coefficient in the radiator.

RESULTS ANALYSIS

Effect of current density step change. The effect on the main parameters involved in water management has been analysed to obtain a first understanding of the complex phenomena involved in the fuel cell system. This analysis has been performed considering different current step changes. Here, it is reported the step from 0.4 A/cm^2 to 0.7 A/cm^2, showing the results for block 3, chosen as example.

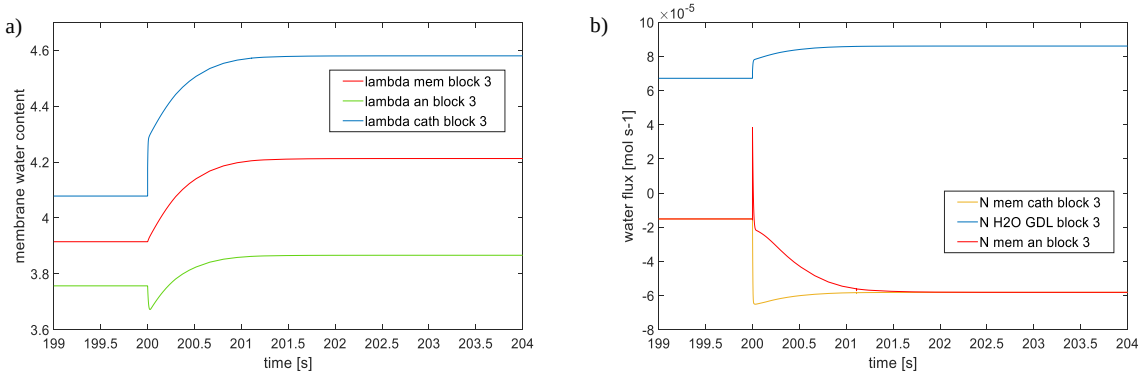

Figure 5 - Membrane water content (a) and membrane water flux (b)

As it is shown in Figure 5.a and Figure 5.b, two different time scales can be recognized after the step in current:

- Immediate response after the change in current, in which the drag effect is predominant, because of current change, and both net fluxes anode side and cathode side become positive: the water content increases on the cathode side and decreases on the anode side as more water is dragged by protons;
- The second one is due to water accumulation in the membrane: due to higher water concentration on the cathode side, back diffusion transport increases (net water fluxes become negative) at the anode side. A disequilibrium is created within the membrane, leading to an increase in water content on the cathode side.

Effect of geometric parameters variation

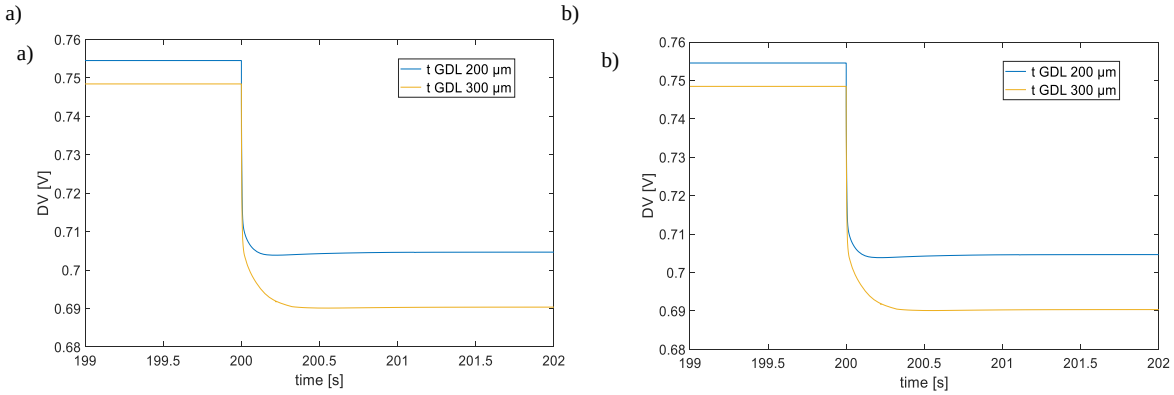

Figure 6 - Effect of change in GDL thickness (a) and membrane thickness (b) on cell voltage

This analysis has been performed at very high stoichiometry to neglect the effect of channel dynamics. Along the in-flow direction, all the channel layers have the same behaviour. The change in geometric parameters affects both transients' timescales and static performance:

- By decreasing the thickness of the gas diffusion layer (Figure 6.a) the time needed by the oxygen to diffuse to the cathode active sites decreases; steady-state condition of cell potential is reached faster, and the voltage is higher as $a_{O_2,CL}$ increases with decreasing thickness;
- Voltage is lower for larger membranes (Figure 6.b) the ohmic loss through the electrolyte is inversely dependent on membrane thickness. Moreover, transient is longer as more time is needed to protons to reach cathode active sites.

Channels Transient effect. At low stoichiometry, typical of automotive operation, the effect of channel transient is evident.

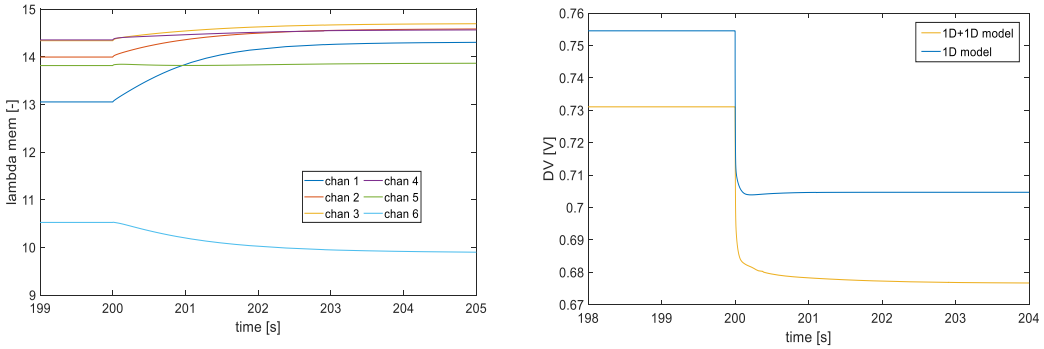

Figure 7 - Effect of channel transients on membrane water content (a) and cell voltage (b)

- Figure 7.a shows that membrane water content varies along the channel layers. The cathode inlet (block 1) and anode inlet (block 6) water fluxes are more relevant than the centre of the cell, this results in a slower dynamic. Anode inlet water content has

a negative slope, as the inlet is drying due to the predominant effect of electro-osmotic drag.

- Mass transport delay influences the cell potential, which, moreover, decreases with respect to the previous case (Figure 7.b): in fact, oxygen activities at the CCL dynamics are globally slower than the high-stoichiometry case.

Effect of humidifier dynamics. The dynamics of the humidifier influences the dynamics of the fuel cell stack, as inlet air takes about 2-5 sec to adapt to new condition, after current step. At the same time, the dynamics of the humidifier is influenced by stack transient response, as the air exiting the FC stack is not in steady state.

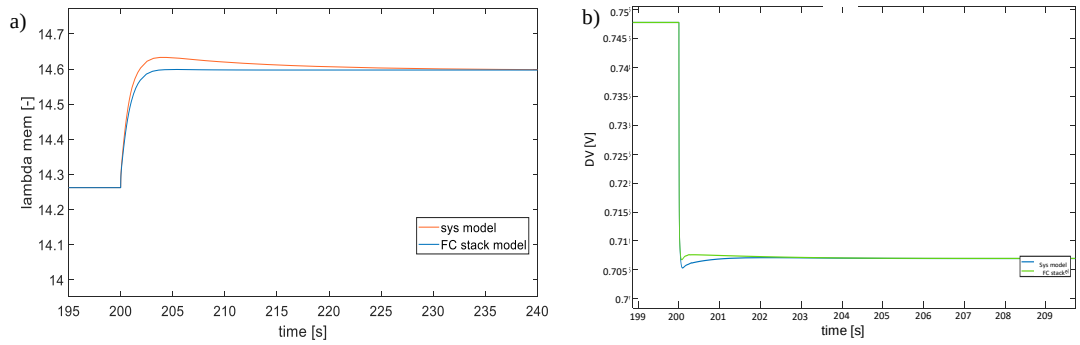

Figure 8 Effect of humidifier dynamics on membrane water content (a) and cell voltage (b)

The combined configuration results in an additional delay in membrane water content, which is linked to the required time for the channel to reach sufficient level of hydration (Figure 8.a). Moreover, after current step change, flow rate at the dry side of the humidifier increases promptly, but it takes some time to reach cathode manifold. It determines a certain time period in which oxygen concentration is not enough to react, resulting into an additional voltage undershoot, which can be observed in Figure 8.b

New European Driving Cycle (NEDC) Simulation Results. The New European Driving Cycle (NEDC) has been replicated by the system model, with the aim to understand stack and system performance, with great attention on the behaviour of the main variables involved in the water management. First, the system performance has been investigated by keeping the stack pressure constant at 2 bar, typical for automotive operation, through a controlled opening of the exhaust valve. Two main criticisms emerged: the system efficiency is low at low-load operation, mainly due to the high power required by the compressor, and strong dehydration of the membrane at the anode inlet layer at high-load operation occurred. A different alternative of removing pressure control, by keeping $A_{nozzle} = 0.01084\ m^2$, has been proposed and discussed.

At low load operation (about 0.1 A/cm^2), the power consumed by the compressor is halved in the variable-pressure case, where the system works at 1.2 bar, with respect to constant-pressure case. At high load operation the difference in the compressor consumption is instead negligible since also in the variable pressure case a 2 bar pressure is reached.

Humidifier operation comparison

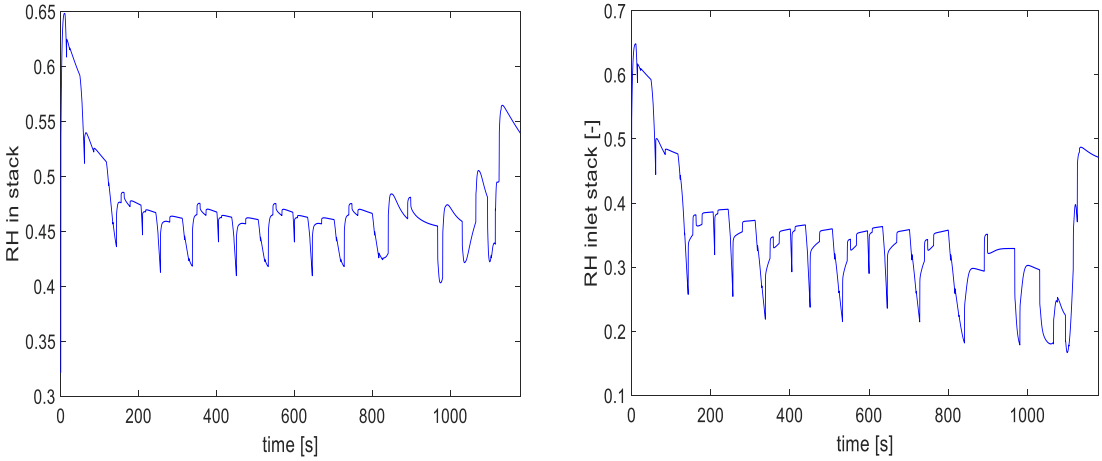

Figure 9 - Inlet Cathode relative humidity comparison

As shown in Figure 9, variable pressure regulation leads to lower cathode inlet RH values. Cross-sectional area opening control, in fact, is beneficial for water exchange mechanism within the humidifier, as expected with high pressure operation. Moreover, it leads to lower membrane water content in the fuel cell, which may accelerate degradation phenomenon.

Stack Performance

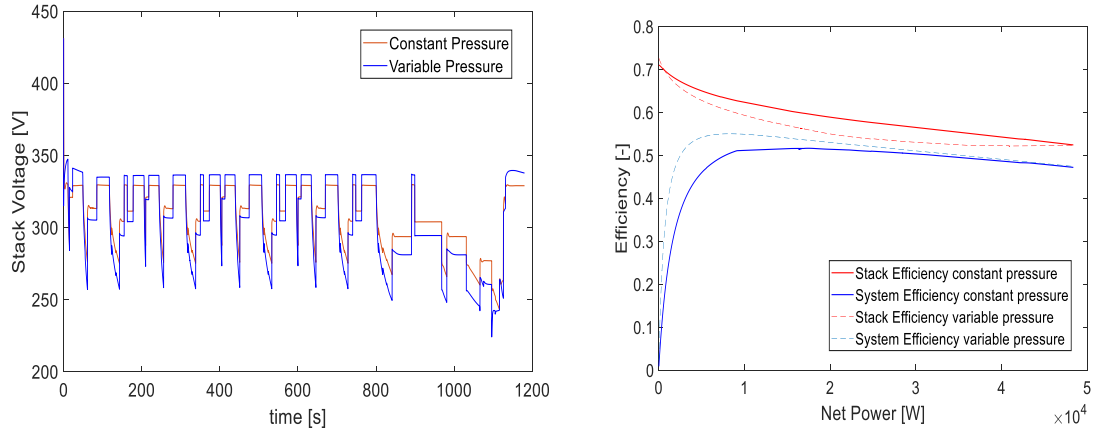

Figure 10 - Stack voltage and efficiency comparison

Figure 10 reveals that two different trends are evident:

- On one side, the reduction of the compressor consumption, occurring at low pressures, leads to a decrease of the gross power produced by the stack; the current generated by the stack is lower, hence the voltage tends to be higher;

- On the other side, low pressure operation, combined with low stack inlet RH, worsens the stack performances, leading to a reduction of the stack voltage;
- Stack efficiency is lower for the variable-pressure case due to lower pressure operation, and only at very high power the performances are comparable, as the stack pressures are similar;
- The system efficiency is globally higher, especially at low load operation: benefits derived from the lower compressor consumption overcome the negative effects on the stack and humidifier. Increasing the load, instead, the reduction of the stack efficiency becomes more relevant.

Conclusion. A PEMFC dynamic system model, focused on air loop, with a 1D+1D fuel cell dynamic model, has been implemented in Matlab-SIMULINK environment.

A preliminary analysis, focused on the effect of the change in geometric parameters and operating conditions on the performance of the PEMFC stack model, has been conducted by means of galvanostatic static and dynamic simulations. Moreover, the effect of mass transport along channels has been investigated. Then, the effect of coupling stack and humidifier dynamic models has been analysed.

The final chapter is focused on the analysis of the PEM system performance, when a NEDC is simulated. Two different control strategies have been adopted: a constant-pressure control and variable pressure control. In the first case, keeping pressure constant at high values is beneficial for the stack performance and humidification, but it requires high compressor consumption at low load. With variable pressure regulation, instead, compressor consumes less at low load, but working at this condition is trivial for the stack and the humidification system, e.g. the effect of membrane dehydration has been captured. As a result, system efficiency is higher in the variable-pressure regulation, while the first alternative leads to higher stack efficiency.

The strength of the model is the ability to perform a system analysis but without losing accuracy on the PEM cell unit.

The model has not been fully validated: a complete experimental set-up apparatus would be required to calibrate the main variables to achieve a high-fidelity model. Moreover, the implementation of liquid water model in the cell is recommended to increase accuracy. Hybridization mechanism, as well as hydrogen loop, are out of the current work. Future integration would be helpful to better simulate real PEM system behavior under automotive operation.

Contents

Introduction

The urgency of reducing the CO2 emissions of road transport through, combined with the vulnerable supply and price volatility in the world oil market, have motivated researchers and policy makers to seek alternatives to gasoline and diesel fuel. Of the suitable alternative solutions, hydrogen fuel cells are one of the most promising replacements of the internal combustion engine. The fuel cells convert the chemical energy of hydrogen into generate electricity, generating heat and water. The fuel can be generated from renewable energy through electrolysis of water and stored on-board the vehicle in high pressure tanks.
The prospect of a clean, widely available transportation fuel has prompted much of the research on hydrogen fuels. Several major automotive manufactures, including Ford, General Motors, Honda, Hyundai, Toyota and Volkswagen are starting to bring fuel cell vehicles on the market. The interest received by PEMFC technology is due to several unique features, such as high efficiency and power density, low emissions, (< 100 °C), quiet operation, fast start-up, fast response to load changes and modularity. A significant advantage of hydrogen fuel cells compared to other electrical powertrains, such as batteries, are extended range and reduced refuelling times. However, there are still important issues to be addressed: absence of distribution network for hydrogen, that hinders a capillary diffusion of this technology, high cost and degradation.

Thesis Outline

The aim of the work is to develop a dynamic model of PEM fuel cell system, mainly focusing on the air loop system, able to capture the principal dynamic phenomena involved. The thesis has been structured in the following chapters:

- Chapter 1: after a brief introduction on the over the PEM fuel cells fundamentals, the main subsystems composing the fuel cell system, such as the air management subsystem, the water management subsystem and the thermal management subsystem, are presented. A literary review of the main components involved in the system is needed, so the main dynamic models of PEM fuel cell, the principal dynamic models of each subsystem as well as the main fuel cell dynamic system models, are discussed.

- Chapter 2: The PEM fuel cell model developed in this work is described, focusing on the main dynamic phenomena involved, such as the oxygen transport, the water management and the reactants flow along the channels. A static validation of the model is performed, so the main parameters and constants affecting the cell operation has been fitted. The transient responce predicted by the model have been compared with the experimental data, highlighting and explaining the main differences between the two.
- Chapter 3: The BOP model is discussed; the main components forming each subsystem have been modelled, such as the power model, the compressor and manifolds model, the humidifier model and the cooling system model, including the radiator and the fan.
- Chapter 4: The PEM fuel cell static and dynamic operation is studied by means of galvanostatic simulations. First, the 1D model has been investigated, focusing mainly on the water and oxygen dynamics. A parametric analysis about the influence of geometric configuration on the cell performances and behaviour has been performed. Then, the attention has been focused on the 1D+1D dynamic model, highlighting how the reactant transport along the channels influences cell operation, with great attention on water transport inside the cell; both static and dynamic simulation have been performed. Furthermore, the humidifier operation has been investigated. After a brief static analysis on the component itself, dynamic analysis aiming at investigating how the stack and the humidifier are correlated and reciprocally influenced, has been conducted.
- Chapter 5: The main control systems implemented in this work are presented and discussed. Then, the NEDC driving cycle has been simulated, showing the main results. The attention has been mainly given on how the PEM fuel cell stack reacts to rapid external load variations, showing how the oxygen transport and mainly the water management inside the cell are influenced by the system operation. Two different control strategies have been implemented, the constant pressure regulation and the variable pressure regulation; stack and system efficiencies have been compared and discussed, showing pros and cons of each strategy adopted.

Chapter 1. State of the Art and Literature Review

1.1 PEMFC fundamentals

Proton Exchange Membrane Fuel Cell (PEMFC) is an electrochemical device that converts directly the chemical energy of hydrogen into electrical energy. As this conversion does not occur in the presence of a combustion or a thermodynamic cycle, efficiency is typically higher than traditional Internal Combustion Engines (ICEs). Moreover, PEMFCs represent a great promise in automotive applications due to their low temperature operation and fast start-up.

The cell is fed with hydrogen at the anode side and with air at cathode side. It generates power by oxidizing hydrogen and producing water.

At the negative side positive ions and electrons are produced by means of the so-called Hydrogen Oxidation Reaction (HOR); the electrons flow in the external circuit, while the positive ions flow throughout the polymer electrolyte membrane. Then positive and negative ions recombine with oxygen at the cathode side generating water and heat, by means of a reaction generally called Oxygen Reduction Reaction (ORR).

$$H_2 \rightarrow 2H^+ + 2e^- \quad (HOR)$$

$$\frac{1}{2}O_2 + 2e^- + 2H^+ \rightarrow H_2O + Heat \quad (ORR)$$

$$H_2 + \frac{1}{2}O_2 \rightarrow H_2O + Heat + Electrical\ current \quad (Global\ reaction)$$

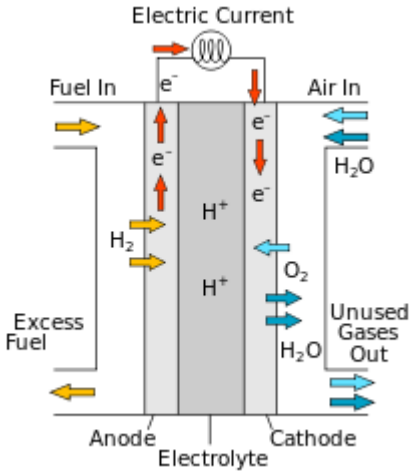

Figure 11 PEM fuel cell scheme

The cell is made up of different parts, respectively:

- Bipolar plates: which act as a reactant distributor as well as provide electrical conductivity to extract the useful electrical work. They are typically made of graphite, or other corrosion-resistant metal, and they need to contact both the GDL and the external circuit.
- Channels: where the reactants flow, air at cathode and hydrogen at anode sides respectively. Channels are obtained at the internal face of bipolar plates, and different shapes can be adopted, such as parallel, interdigitated or serpentine.
- Gas Diffusion Layer (GDL): typically made of a porous carbon paper/carbon felt, typically 200 – 300 μm thick. It allows the diffusive flow of reactants from the channels towards the active sites and removes water from the system. Moreover, it gives mechanical support to the membrane and it provides a conductive path between the CL and the current collector.
- Micro porous layer (MPL): is placed between GDL and CL. This domain region presents different properties but same physics as GDL, with a typical thickness of about 40 - 60 μm and a lower porosity with respect to GDL. It allows a better physical contact between GDL and CL, preventing GDL structure to damage CL region or catalyst to penetrate deeply inside diffusion layers. It improves not the electric contact between the two and it enhances water management.
- Catalyst Layer (CL): a porous electrode, typically some tens of μm of thickness, containing carbon-supported platinum mixed with polymer electrolyte, where the electrochemical reactions occur. The presence of the Catalyst is necessary so to reduce the activation energy required for the reactions even at low temperature, and to speed up the reaction rates.
- Polymer Electrolyte Membrane: it separates the positive side with the negative side. It has the function of conducting protons efficiently and preventing electrons and reactants transport between the two electrodes. It is usually made of a sulfonated tetrafluoroethylene-based fluoropolymer-copolymer, ionically conducting but electrically insulating, usually called Nafion®.

GDL, CL and membrane are collectively known as Membrane Electrode Assembly (MEA), which represents the core of the fuel cell. Since power density of a single cell is very low (from 0 to 1 W/cm2 as the typical range), in practical applications many cells are connected

in series so to achieve the desired power; then, the whole system is closed by a left and a right end plate, respectively. The assembly is called fuel cell stack (Figure 12).

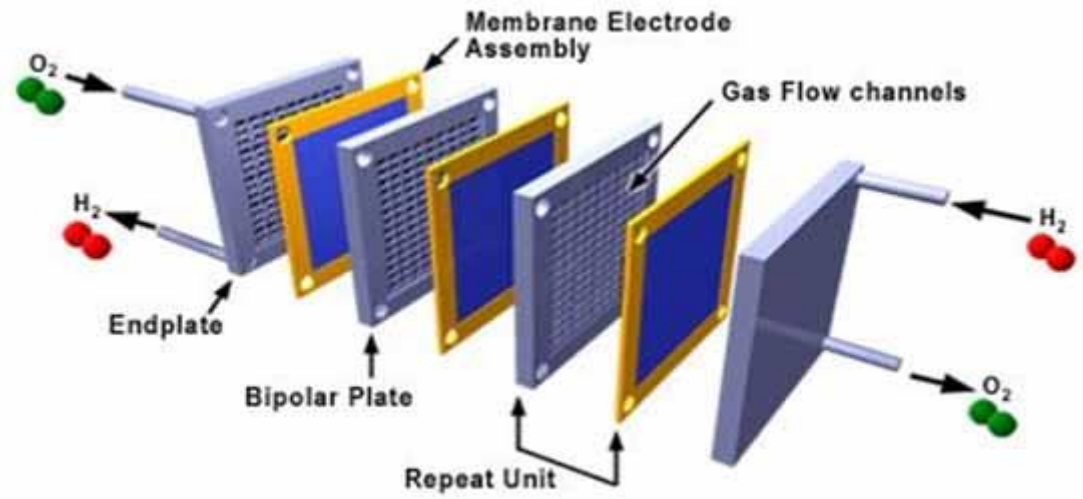

Figure 12 Fuel cell stack assembly scheme

1.2 Fuel cell system fundamentals

To power an automotive vehicle, the fuel cell stack needs to be integrated with other components. The main subsystems, forming the fuel cell system, are the reactant management subsystem, the water management subsystem, thermal management subsystem and power management subsystem [1]. The figure below (Figure 13) shows a schematic representation of the system. In this section, each subsystem is briefly presented, explaining the major flows involved and the main connections with the other subsystems.

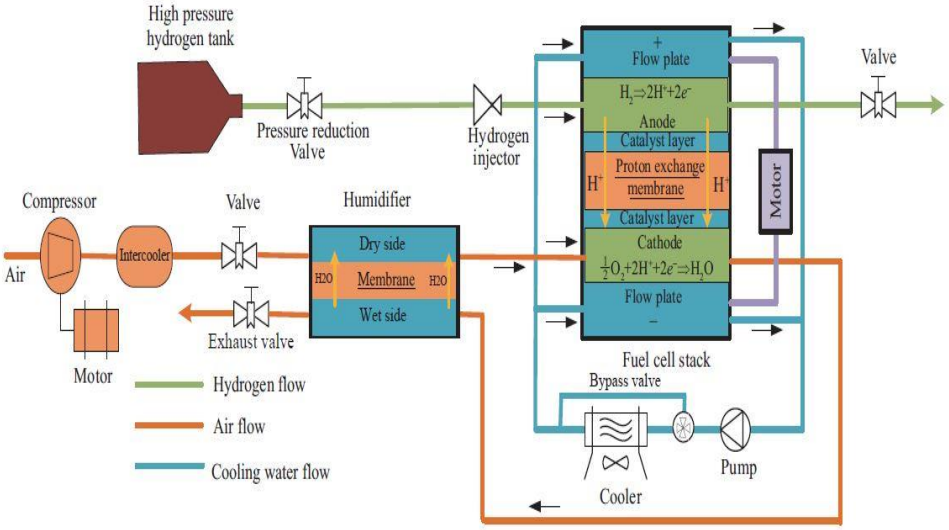

Figure 13 PEMFC system scheme

Reactant management subsystem

Reactant management subsystem consists of hydrogen supply loop and air supply loop. Air loop subsystem is composed by the compressor, the supply manifold and the return manifold. Since the vehicle traction motor draws current, oxygen is depleted in the fuel cell stack, so air is constantly required; the air management subsystem aims to provide the requested air flow to the cathode side. A voltage command is used in the compressor so to ensure the desired air quantity at the required pressure. Operation at high pressure significantly improves the reaction rate, and thus the power density and the efficiency of the cell [2]. Once compressed, the air flows in the supply manifold, which represents the system of pipelines and connections between the compressor and the stack. At the outlet of the fuel cell system, the waste air is carried to the return manifold, which aims to reject the exhaust air to the external environment.

Hydrogen supply subsystem, instead, has not been investigated in this work, and hydrogen is assumed to be immediately fed to anode side at fixed relative humidity and pressure.

Water management subsystem

The aim of the water management subsystem is to maintain hydration of the polymer membrane and to balance water/usage consumption in the system. It is well known that dry membrane causes high ohmic losses, while flooding worsens the cell operation, thus management of the amount of water involved in the cell is crucial to grant a proper

performance of the stack. The water management subsystem is composed by the humidifier, which aims to increase the cathode inlet RH.

Thermal management subsystem

The thermal management subsystem aims to control that the stack temperature is kept in a safe range. Since heat is released during the fuel cell operation, the stack tends to heat up with time. So, a cooling system is needed to avoid excessive temperatures. The thermal management subsystem includes the radiator and the vehicle air flow model.

Power management subsystem

The power management subsystem aims to control the power interaction between the PEMFC stack and the battery. It includes voltage regulators, DC/DC converters, chopper circuits. In this model, this subsystem has not been implemented, as the hybridization management investigation is out of the present work.

1.3 Literature review

During the recent years, several fuel cell models have been proposed by different authors. This chapter has been organized as follow:

- First, a review of the principal fuel cell models is presented. After a review on the steady-state models, widely abundant in literature, the attention has been focused on the dynamic models, capable of describing the cell transient behaviour during load variations, typical of the automotive operation.
- Then, an analysis of the main fuel cell subsystems, such as the air supply management subsystem, the water management subsystem and the thermal management subsystem is performed, focusing both on the component modelling and on the control strategies adopted.
- At the end, the principal fuel cell system dynamic models are presented.

As suggested by [3], three main forms of fuel cell modelling are present in the academic literature: physical models, semi-empirical models and fully empirical models. This work will focus on physical/semi-empirical models, as they represent a good compromise between accuracy and computational cost.

1.3.1 FC model review

Steady state models

Steady-state models are abundant in the academic literature. Springer *et al.* [4] presented an isothermal, 1D steady-state model of PEMFC with Nafion 117 membrane. The model was mainly focused on describing the water transport mechanism across the cell, considering the effects of water diffusion coefficients, electro-osmotic drag coefficients, water absorption and membrane conductivities, while the water saturation was neglected. Fuller and Newman [5] developed a two phase flow model, investigating the beneficial effects of the introduction of a MPL into the MEA, always in a steady state operation. Their results show how the MPL leads to an increase of the performance of the cell, because of better oxygen transport and structural stability. An higher level of accuracy was reached by Amphlett *et al.* [6], who considered Stefan-Maxwell and Nerst-Planck equations to better capture the physical phenomena involved. Some semi-empirical relations have been used, since the increase of number of variables considered. Wang and Wang [7] proposed a CFD model, in order to better understand the influence of the flow field geometry on the cell operation.

Dynamic models

As already mentioned, just a few PEMFC dynamic models are present in literature. One of the first fuel cell dynamic model was presented by Amphlett *et al.*[8], who developed a 1D non isothermal model, with the aim of investigating how the temperature variation influences the cell performance. Ceraolo *et al.*[9] developed a dynamic model, in MATLAB-SIMULINK environment, focusing their attention mainly on the oxygen dynamics in the GDL and on the charging/discharging effect of the double layer at the cathode side. Jieran *et al.*[10] proposed a similar model, showing how the internal microstructural state of the gas diffusion layer can affect seriously the oxygen dynamics. Moreover, the water accumulation in the membrane has been considered in the analysis. A more complete model was developed by Pathapati *et al* [11], which included the dynamics of the flow and pressure in the channels.

1.3.2 Fuel cell system components model review

Air supply management subsystem

Even though air compressors for traditional vehicles and fuel cell vehicles share many similarities, a fuel cell vehicle cannot directly employ the effective and mass-produced traditional vehicles' air compressors. This is because the fuel cell vehicles have special requirements, such as oil free, low flow rate with high pressure ratio, high efficiency, and low weight and volume. These air compressors include screw compressor with expander, roots compressor with expander, turbo-compressor, and scroll compressor with expander. Results show that the turbo-compressor and the roots compressor/expander have higher performance compared to the others in the aspects of input power, system efficiency, weight, and volume. However, the two of them also show some defects, since the turbo-compressor has a limited turndown ratio due to the surge, while the roots compressor has a limited pressure ratio and pulsation characteristics [12].

In this work, following the approach proposed by [13], a centrifugal compressor based on an Allied Signal compressor has been modelled.

The control of the reactants supply is of relevant importance for conceiving PEMFC power systems [14]. It has been acknowledged that oxygen excess ratio control is one of the most important actions to enhance protection and performance of fuel cells. A sliding mode control achieved by adjusting the compressor supply voltage was assisted with a nonlinear observer predicting the oxygen excess ratio and improved with a novel tuning procedure [15]. In a second work, a feedforward fuzzy-PID control was proposed; the model used for

designing the oxygen excess ratio controller included cathode and anode mass flow transients, membrane hydration dynamics, as well as the fuel cell BOP simulation, the controller was developed to adapt the PID parameters to achieve the regulation of the air flow rate using on-line fuzzy logic optimization loop. Another typical control strategy adopted in literature involves the cross-sectional area of the back pressure valve; [16] implemented a PID controller, capable of adjusting the cross-sectional area so to maintain the requested stack pressure. In this work both the compressor supply voltage and the back-pressure valve control have been implemented.

Water management subsystem

There exist two types of humidification systems for PEMFC, namely internal and external. Among the internal humidification systems there are stack-integrated membrane humidifiers, steam or liquid water injection humidifiers, and membrane additives and porous absorbent sponges. The principal disadvantage of internal humidification is the limit of the total cathode outlet water available, determined by the fuel cell conditions, especially at higher flow rates [17]. In this work the attention has been focused on the external humidification systems.

Studies involving various types of humidifiers have been conducted in order to control the temperature and relative humidity of the supply air [14] [18]. Extensive studies have been also conducted on bubbling, water spray, enthalpy wheel, and membrane humidifiers. From these types, membrane humidifiers are the most suitable for PEMFC vehicles due to their fast response and simplicity [19].

Recently, case studies have been carried out to apply membrane humidifiers to PEMFC systems. Membrane humidifiers are categorized as either shell-and-tube or plate-and-frame membrane humidifiers depending on the shape [20]. Kang [21] investigated the performance of a shell-and-tube membrane humidifier for PEMFC vehicles. However, the shell-and-tube membrane humidifier has the disadvantages of a bulky volume and difficulty in mass production. Accordingly, studies on the plate-and-frame membrane humidifier are underway to overcome these drawbacks.

Ahluwalia [22] conducted static and dynamic tests on a plate-and-frame membrane humidifier. Even though these studies developed a finite-difference model, the heat transfer, which is a main dynamic mechanism in the plate and- frame humidifier, was not considered. Yun *et al.*[19] developed a one-dimensional heat transfer in the plate, one-dimensional heat

and mass transfer in the membrane, and one-dimensional channel in the plate-and-frame membrane humidifier.

Based on the proposed model, the dynamic response of the plate-and-frame membrane humidifier for PEMFC vehicles was analysed under various operating conditions. This work mainly follows the approach of [19], who developed a pseudo-multi-dimensional dynamic model was developed for predicting the dynamic response of a plate-and-frame membrane humidifier with a plate domain.

Different control strategies, which aim to regulate the inlet RH in the fuel cell stack, are proposed and discussed in the academic literature. [17] proposed to regulate the back-pressure valve in the return manifold, so to keep high inlet relative humidity levels, while [23] designed a non-linear control strategy based on second order sliding mode, in which the variation of the stack inlet RH is achieved by means of a resistor placed in the humidifier itself and by the back-pressure valve in the exhaust system. In this work no humidifier control strategy has been implemented.

Thermal management subsystem

Three main PEMFC cooling system techniques are presented in literature: the air cooling, the liquid cooling and the evaporative cooling [16]. The differences between air and liquid cooling are briefly discussed, while the evaporative cooling technique has not been investigated in this work.

In low power fuel cell systems (<100W) which do not require external humidification it is possible to remove heat through a combination of airflow through the cathode and natural convection from the surface, this is the simplest form of thermal management since no additional components are required [24].

As heat generation increases with power, the cathode stoichiometry required to maintain thermal balance also increases, removing more water vapour from the cell and drying the membrane. Eventually it becomes more practical to separate the cooling air ow from the reactant air ow to maintain membrane humidification [25]. The separate cooling air flow passes through channels between the bi-polar plates, removing waste heat through forced convection. An additional fan is required compared to passive cooling, variations in the fan voltage can be used to regulate the stack temperature. This solution ca be applied just to small size systems; in fact, the flow rate of air between the cells of a larger stack would induce significant pressure loss and an infeasible parasitic load [16]. So, to power a conventional passenger vehicle, a liquid cooling solution is adopted. In a liquid cooled

PEMFC system the waste heat from the electrochemical reaction is removed by passing a liquid cooling medium through channels in the bi-polar plates. The heated liquid coolant is then cooled in a separate heat exchanger, usually the radiator. Once cooled, the coolant returns to a tank where it is then pumped back into the fuel cell stack, completing the coolant loop. The design of liquid cooled fuel cell stacks has received significant attention in the literature, particularly relating to the optimization of the coolant channel geometry, referred to as the coolant flow field [26].

The purpose of the thermal management system in a liquid cooled fuel cell is to maintain the stack temperature within acceptable limits, this is achieved by regulating the temperature and flow rate at which the coolant enters the fuel cell stack. A low coolant inlet temperature will remove more heat from the stack although at the expense of increasing the thermal gradient within the stack, conversely a higher coolant inlet temperature will reduce heat transfer from the stack to the coolant but reduce the thermal gradient within the stack. Similarly, an increased coolant ow rate will both improve the heat transfer coefficient and reduce the thermal gradient across the stack but at the expense of increased parasitic load [16].

Several different regulation strategies can be found in literature. [27] proposed to control the inlet coolant temperature regulating the heat exchanger fan speed and coolant flow rate, while an alternative method of regulating stack temperature is to modify the flow rate of coolant exposed to the external heat exchanger through a variable radiator by-pass valve [28]. In this work, both a bypass valve and a fan speed control have been implemented.

1.3.3 FC system dynamic models review

Rabbani *et al* [29] developed a control-oriented model in Aspen Plus Dynamics, which accommodates electrochemical, thermal, feed flow and water crossover models in addition to two-phase calculations at fuel cell electrodes. The model parameters have been adjusted specifically for a 21.2 kW Ballard stack. Controls for temperatures, pressures, reactant stoichiometry and flows are implemented to simulate the system behaviour for different loads and operating conditions. The attention has been mainly focused on the thermal management strategy, which greatly influences the stack performances.

Pukrushpan *et al.*[13] developed a nonlinear fuel cell system dynamic model suitable for control study. The transient phenomena captured in the model include the flow characteristics and inertia dynamics of the compressor, the manifold filling dynamics, and

consequently, the reactant partial pressure. The attention has been mainly focused on the air control management subsystem.

Ashley Fly [16] proposed a fuel cell dynamic system model, focusing on different cooling techniques. The cases of air cooling, liquid cooling and evaporative cooling are compared, showing advantages and disadvantages of each configuration, as well as the different control strategies adopted. A liquid radiator and a vehicle air flow/fan steady-state models are presented and discussed.

1.4 Aim of the work

In the academic literature different PEM fuel cell dynamic models are present, which analyze the main dynamic phenomena involved, such as the oxygen and water transport. On the other hand, the PEM fuel cell system models found in literature are mainly focused on the system point of view, highlighting how the control strategies affect the operation of the whole plant. These works typically imply a lumped 1D model for the fuel cell stack, neglecting all the phenomena linked to the to the reactants transport across the channels, that greatly influence the stack dynamics, and particularly the water management inside the cell. These phenomena, e.g anode dehydration or water flux evolution along the channels,,are not visible in a 1D model. The aim of this work is to develop a PEM fuel cell dynamic system model, mainly focused on the air loop, including a 1D+1D dynamic PEM fuel cell stack model, able to capture the phenomena exposed above. The analysis has been organized starting from the PEMFC stack, with the aim to observe its peculiar phenomena and timescales, and through the addition of the other components of the air subsystem, trying to understand how they affect its performance and dynamic behaviour, arriving, in the end, at the simulation of the global system, under a typical driving cycle. In detail, the following steps are followed:

- First the attention has been focused on the fuel cell, analysing its dynamic behaviour by means of galvanostatic step simulations;
- Then, the interaction with the humidifier has been studied, analysing how the dynamics are interconnected;
- At the end, the whole system has been simulated, aiming at distinguishing the effect of each component of the system and how it interplays with each phenomenon of the PEMFC (water management, oxygen distribution, local temperature).

Chapter 2. PEMFC Model Formulation

This chapter introduces the physical concepts and governing equations used for the implementation of the mathematical PEM fuel cell model.

- First, all the assumptions at the basis of the model are listed.
- Then, all the equations describing the main phenomena are reported per each domain component of the MEA.
- At the end, a description of experimental set-up and the procedure used to validate the model are reported.

2.1 Mathematical Model and Assumptions

In order to investigate physic and electrochemical phenomena which occur inside the PEM fuel cell, multi-component gas species transport, multiphase water transport, phase change processes, electrochemical reaction kinetics, charge and energy transport. Clearly, a complete modelling of all the phenomena involved would be not applicable in practice, and the introduction of some assumptions is necessary.

In this work, a dynamic, 1D+1D, non-isothermal model of the cell has been modelled in MATLAB-Simulink environment. It considers:

- cathode and anode kinetics
- mass transport phenomena occurring at the cathode GDL
- mass transport phenomena at the channels, both at anode and at cathode sides.
- Water transport throughout the membrane.

The main assumptions are:

- Gas species behave as ideal gases;
- Gas flow in the channels is laminar, due to small Reynolds numbers;
- Diffusion media and catalyst layers are homogeneous and isotropic;
- Contact resistance among the layers is neglected;
- Liquid water saturation level in the GDL has been neglected: water is assumed to be present only in dissolved phase;
- MPL has not been implemented: at cathode side GDL is assumed to be directly in contact with the CCL;
- Catalyst layers are interfaces;

The voltage of the cell can be expressed as the combination of three terms, by means of the following equation:

$$\Delta V_{cell} = (E^{+} + \eta^{+}) - (E^{-} + \eta^{-}) - \eta_{el}$$

In particular, $(E^{+} + \eta^{+})$ represents the cathode contribute, $(E^{-} + \eta^{-})$ the anode contribute, generally almost negligible, and η_{el} the voltage loss due to the presence of the electrolyte.
Inside each domain region containing a fluid phase, continuity equation is solved in order to grant global conservation of mass:

$$\varepsilon^{eff} \frac{\partial \rho_g}{\partial t} + \nabla \cdot (\rho_g \vec{u}g) = Sm$$

Where ρ_g is the density of the ideal mixture, $\vec{u}g$ is the velocity vector, ε^{eff} is the effective porosity of medium for gas phase transport and Sm is the source term, which represents generation or consumption of mass related to electrochemical reactions occurring within the domain.
Moreover, as mixture is composed of different species, continuity equation is solved per each species:

$$\frac{\partial(\varepsilon^{eff} x_k)}{\partial t} + \nabla \cdot (\rho_g \vec{u}g x_k) = \nabla \cdot \vec{j}_k + S_k$$

Where x_k is the mass fraction of the k-species, $\vec{j}_k$ is the mass diffusive flux vector and S_k is the source term, which represents the generation or consumption of the k-species.
Transport of charge species occurs through the solid phase or through the electrolyte thanks to the presence of a potential field, electric and protonic, respectively.
Governing equations of charge transport for electrones and protons are, respectively:

$$-C_{DL} \frac{\partial \eta}{\partial t} + \nabla \cdot \overrightarrow{J_s} = S_{\Phi_s}$$

$$C_{DL} \frac{\partial \eta}{\partial t} + \nabla \cdot \overrightarrow{Jm} = S_{\Phi_m}$$

Where C_{DL} is the double layer capacitance and η is the local overpotential. $\overrightarrow{J_s}$ and $\overrightarrow{Jm}$ are the electronic current densities through solid phase and protonic current density through the

electrolyte. According to Ohm's law, electronic and protonic current density can be written as:

$$\overrightarrow{J_s} = \sigma_s \nabla \phi_s$$

$$\overrightarrow{J_m} = \sigma_m \nabla \phi_m$$

Where ϕ_s and ϕ_m are the electric and protonic potential, σ_s and σ_m are the electric conductivity of solid material and protonic conductivity of electrolyte.
S_{Φ_s} and S_{Φ_m} are the source terms associated with HOR and ORR reaction rates, defined as

$$S_{\Phi_s} = \begin{cases} i_a \; anode \; CL \\ -i_c \; cathode \; CL \end{cases}$$

$$S_{\Phi_m} = \begin{cases} -i_a \; anode \; CL \\ i_c \; cathode \; CL \end{cases}$$

While in all other regions they are null since no electrochemical reactions occur.

2.1.1 1D+1D cell Model

The current model was developed to dynamically resolve local states and operating features of the fuel cell. It was developed in Matlab-SIMULINK framework. All the components are discretized in space using control volumes. In this way, equations can be described in terms of ordinary differential equations that can be solved in Simulink: each of the control volumes is characterized by a single lumped set of temperature and activity of species conditions used to determine thermodynamic properties of the discretized fuel cell. Individual nodes are therefore connected each other, in order to account for heat and mass transport between adjacent nodes.

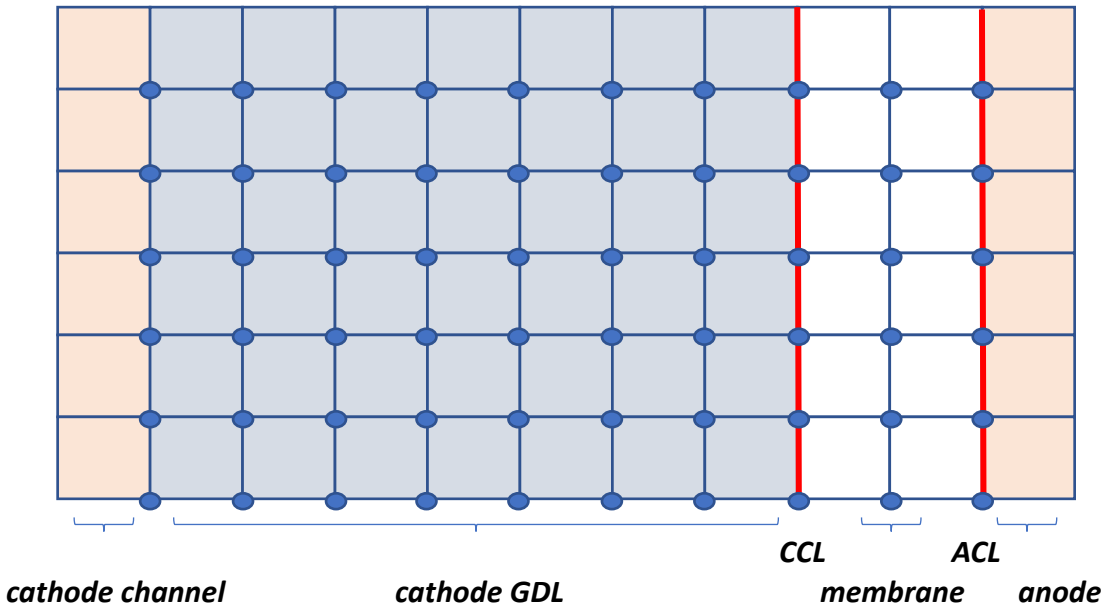

Figure 14 PEMFC discretization

In particular, the cell has been discretized perpendicular to the flow as well as in the flow plane direction to solve the local states, making the model semi-2D. Six control volumes in the flow parallel direction were chosen because both operating voltage and local current are governed by local species mole fractions at the triple phase boundary and by membrane hydration mechanism, which can only be investigated by looking at the local heat transfer, electrochemistry and water transport.

Moreover, in order to investigate the local mole fractions at the triple phase boundary, seven GDL control volumes at the cathode side and two membrane control volumes were implemented. This kind of discretization is beneficial to more accurately model the extent of membrane hydration: this makes it possible to account for water formation, osmotic drag, back diffusion and water accumulation within the fuel cell.

To simulate the geometric configuration of fuel cell channel paths, 15 individual small channels are lumped together, into single flow channels in each of the channel nodes used in the model. A deeper analysis of geometric paths is out of the investigation.

2.1.2 Fuel Cell Stack Model

Each of the cells in the stack is assumed to operate identically, so a single cell simulation is used to calculate fuel cell stack performance. As it is very difficult to simulate the cell to cell variation of temperature, the stack is assumed to simply to be an extension of unit fuel cells,

with no mass and temperature transfer among cells. Thus, the voltage of the stack is simply calculated as:

$$\Delta V_{stack} = \Delta V_{cell} * n_{cells}$$

2.2 Components Model

2.2.1 Catalyst layers

Each catalyst layer is made up of three phases: an ionomer phase, a carbon phase and pores (void spaces). At the cathode, the ionomer phase allows the conduction of H^+ ions coming from the membrane to the reaction sites. The carbon phase conducts electrons, while oxygen and water flow through the pores. The catalyst layer can be thought as a collection of agglomerates separated by pores, in which the ionomer surrounds the carbon-supported platinum particles. The oxygen flows though the pores and then diffuses through the ionomer phase to reach the Pt reaction sites. When it combines with protons and electrons the reduction reaction occurs and water is formed. Then, water dissolves into the ionomer and flows though the pores out of the CL.

In a narrow region of the interface between the electrode and the electrolyte a very thin electric double layer exists. Electrons collect on the surface of the catalyst particles, while Hydrogen ions, which are attracted to the electrons, collect on the electrolyte surface and the accumulation of electrons and ions at the catalyst-electrolyte interfaces generates a voltage. The double layer acts as a capacitor which charges/discharges when current changes. Purkuspan et Al. [30] estimated the dynamics of this term to be extremely fast.

The model assumes CL to be an interface, thus effects related to the thickness of the CL were not investigated.

Cathode catalyst layer

The cathode CL model receives the following inputs (Figure 15):

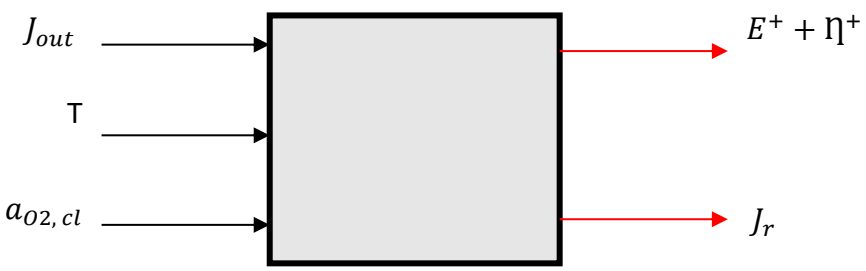

Figure 15 Cathode catalyst layer model scheme

- the external current density J_{out}, coming from the vehicle model;
- the temperature of the stack T, coming from the thermal model
- the oxygen activity at cathode CL $a_{O2,cl}$, coming from the GDL model.

The values calculated by the model are:

- the cathode voltage $E^+ + \eta^+$, needed to evaluate the cell voltage ΔV
- J_r, which is the current density required at the cathode CL to perform the ORR.

The model solves the following equation, which gives the CCL dynamics:

$$J_{out} = J_r + J_{DL}$$

With

$$J_{DL} = C_{dl}\delta_{cl}\frac{d\,(E^+ + \eta^+)}{dt}$$

In particular δ_{cl} is the length of the CL and C_{dl} is the capacity of the Double Layer (DL), that describes the effect determined by the interface between electrolyte and electrode inside pore volume of CL and thus it provides information about the extent of Pt/carbon coverage by ionomer.

J_{DL} represents the flux of electrons coming from the discharge of the Double Layer, not associated with any consumption of oxygen; since the ORR is far from the equilibrium, it is reasonable to assume Tafel Equation to be valid, so J_r can be expressed as:

$$J_r = -4\,F\,Kr\,ECSA\,Pt_{Loading}\,a_{O2,cl}\,e^{\frac{-(E^+ + \eta^+)}{b}}$$

Where F is the Faraday constant, Kr is the kinetic constant of the ORR, $ECSA$ is the electrochemical active surface area, $Pt_{Loading}$ represents the amount of platinum inside the electrodes and b is the Tafel Slope, which can be expressed as:

$$b = \frac{R\,T}{\alpha_{ORR}\,F}$$

Where R is the gas universal constant, T is the cell temperature and α_{ORR} is the ORR charge transfer coefficient.

Anode catalyst layer

Figure 16 Anode catalyst layer model scheme

The anode CL model takes as input (Figure 16):

- the external current density J_{out}
- the stack temperature T
- the hydrogen activity a_{H2}, coming from the anode channel model

The block provides the anode potential $E^- + \eta^-$ as the only output, required to calculate the cell voltage ΔV.

Since HOR is close to the equilibrium, the anode kinetics must be modelled by means of the complete Butler Volmer equation:

$$J_{out} = ECSA\, Pt_{Loading}\, F \left(K_o\, a_{H2}^{0.5}\, e^{\frac{(E^- + \eta^-)\,\alpha_{HOR}\,F}{R\,T}} - K_r\, a_{H+} e^{\frac{(E^- + \eta^-)\,(\alpha_{HOR}-1)F}{R\,T}} \right) + C_{dl}\delta_{cl}\frac{d\,(E^- + \eta^-)}{dt}$$

here K_o is the kinetic constant of the oxidation process, a_{H2} is the hydrogen activity at the anode CL, α_{HOR} is the HOR charge transfer coefficient, K_r is the kinetic constant of the reduction process and a_{H+} is the activity of positive ions produced by means of HOR at anode CL. Since the HOR kinetics is extremely fast (1e-9 s) it is reasonably possible to neglect the time-dependent term, and so assume steady state behaviour at anode side. Since at the anode side the cell is typically fed with high hydrogen concentration and because of the very small incidence of the anode contribute (in the order of 1-10 mV typically) in the evaluation of the cell potential, it has been decided to neglect the diffusive flow of hydrogen from the channel to the CL, and so the anode GDL has not been modelled. In this way a_{H2} at the ACL is assumed to be equal to $a_{H2,ch}$.

2.2.2 Cathode gas diffusion layer

Oxygen is consumed by ORR at the cathode CL: this creates a concentration gradient between the cathode channel, where air is flowing, and the CL, leading to a flow of oxygen throughout the GDL. The flux is directed from the channel, where the concentration is higher, to the CL, where the concentration is lower. With the approximation of dilute mixture, the flux of gaseous species is descripted by the Fick's Law. It is formulated as

$$N_i^g = -D_{i,m}^{g,eff} \nabla C_i^g$$

Where $D_i^{g,eff}$ is the effective diffusivity of gas species in the mixture, corrected for porous media:

$$D_i^{g,eff} = D_i^g \varepsilon^{1.5}$$

The dependency of diffusion coefficient on pressure and temperature can be computed by different relations, such as the approximate one of Chapman-Enskog.
In order to have more representative dynamic of species diffusion though the GDL, even an accumulation term has been considered in the mass conservation equation. Then, even a water flow GDL model has been presented; it considers the water vapor present in the air flowing in the channel, the water produced at the CCL by the ORR, and the net water flux through the electrolyte.

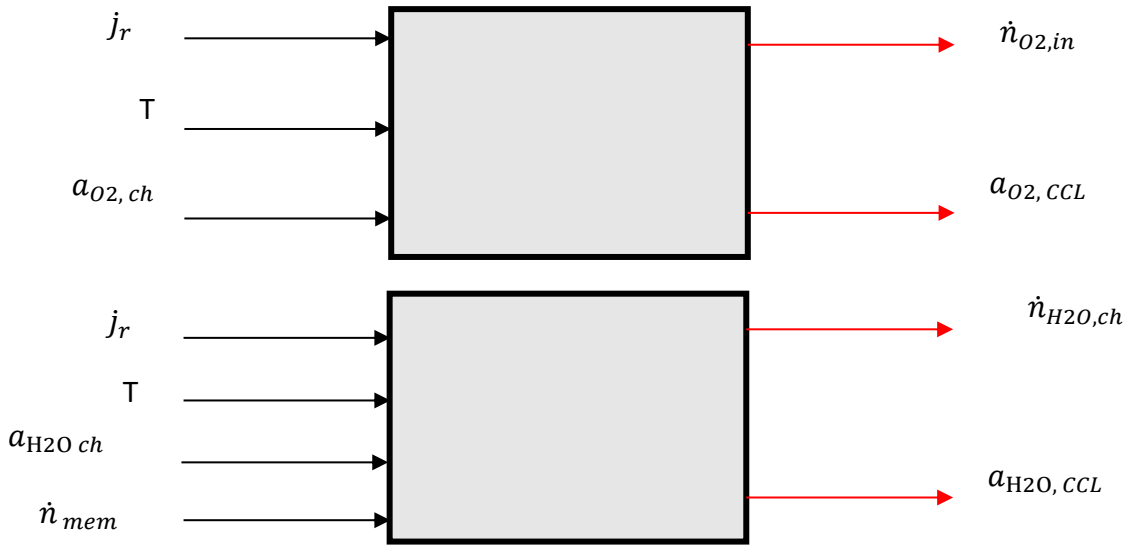

Figure 17 oxygen and water transport across GDL model scheme

In order to solve oxygen transport at the Cathode GDL, the model takes as input (Figure 17):

- the oxygen activity in the cathode channel inlet $a_{O2,ch}$;
- the stack temperature T;
- $\dot{N}_r$, equal to the flow rate of oxygen required by the cathode catalyst layer to have ORR.

The outputs of the block are:

- the oxygen activity at the cathode CL $a_{O2,cl}$;
- oxygen flow rate coming from the cathode channel N_{in}, equal to the sum of the flow rate of oxygen $\dot{N}_r$ and the amount of oxygen accumulated in the GDL volume.

The model solves the following mass conservation equation:

$$\frac{J_r}{4\,F} + \frac{P_{ref}}{R}\,\delta_{gdl}\,\frac{d}{dt}\left(\frac{a_{O2}}{T}\right) = \frac{D_{O2}}{\delta_{gdl}}\,\frac{P_{ref}}{RT}\,\left(a_{O2,ch} - a_{O2,cl}\right)$$

The following relation is valid:

$$\dot{n}_{in} = \frac{J_r}{4\,F} + \dot{n}_{acc}$$

Where

$$\dot{n}_{acc} = \frac{P_{ref}}{R}\,\delta_{gdl}\,\frac{d}{dt}\left(\frac{a_{O2}}{T}\right)$$

From the equation (number) it is possible to distinguish:

- $\dot{N}_r = \frac{J_r}{4\,F}$ is the flux of oxygen required by the ORR.
- $\frac{P_{ref}}{RT}\,\delta_{gdl}\,\frac{d}{dt}\left(\frac{a_{O2}}{T}\right)$ represents the mass accumulated in the GDL volume
- $\frac{D_{O2}}{\delta_{gdl}}\,\frac{P_{ref}}{RT}\,\left(a_{O2,ch} - a_{O2}\right)$ represents the diffusive term, evaluated with Fick's law of diffusion, under the hypothesis of linear oxygen concentration gradient in the GDL

In particular P_{ref} is the reference pressure of the system, δ_{gdl} is the GDL length, D_{O2} is the oxygen diffusivity through the GDL and $a_{O2,ch}$ is the oxygen activity in the cathode channel. From the time-dependent term, it is possible to obtain the oxygen activity profile:

$$\frac{P_{ref}}{R}\,\frac{\delta_{gdl}}{T}\,\frac{da_{O2}}{dt} = \frac{D_{O2}}{\delta_{gdl}}\,\frac{P_{ref}}{RT}\,\left(a_{O2,ch} - a_{O2}\right) - \frac{J_r}{4\,F} + \frac{P_{ref}}{R}\,\frac{\delta_{gdl}}{T^2}\,a_{O2}\,\frac{dT}{dt}$$

As previously mentioned, the cathode GDL has been split in several blocks and in each of them the equation previously presented has been solved. The last block evaluates $a_{O2,cl}$ and $\dot{N}_r$, which clearly corresponds with the J_r calculated in the cathode CL model.
The water flow cathode GDL model presents the following inputs:

- J_r, coming from the cathode CL model;
- The water activity in the cathode channel $a_{H_2O,ch}$, coming from the cathode channel model;
- The net water flux flowing in the membrane, evaluated at the cathode side $N_{memb,cath}$;
- The temperature of the stack T;

While the two outputs are:

- $N_{H_2O,GDL}$, which represents the sum between $N_{memb,cath}$ and the water produced at cathode CL by ORR. $N_{mem,cath}$ is assumed positive when it is moving in the anode-cathode direction. As one water molecule is produced per 2 electrons consumed in the ORR reaction:

$$N_{H_2O,GDL} = N_{memb,cath} + \frac{J_r}{2F} A_{to\ GDL}$$

- $a_{H_2O,cath}$ which represents the water activity at the cathode CL needed in the membrane model.

2.2.3 Membrane

Water management is a critical issue for the performance of a PEMFC. Improper water management leads to membrane dehydration or electrodes flooding:

- The membrane needs to be kept properly hydrated in order to avoid the decrease of conductivity, leading to an increase of ionic resistance and ohmic loss: it results in a drop of the cell potential and power loss;
- When the membrane is fully saturated with water, water bands are formed and this leads to flooding effect, which worsens the performance of the cell;

There is still low consensus about the mechanism of water transport in proton-conducting membrane. It is still not clear the phase in which water is present inside the ionomer, whether it is liquid or dissolved phase. In this model, water is assumed to be in dissolved phase, as a result of chemical interaction with the ionic groups and protons travelling through the

membrane.

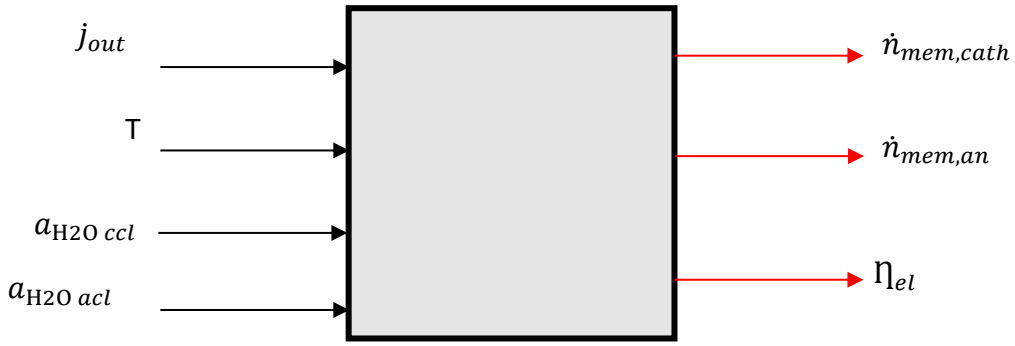

Figure 18 membrane model scheme

The membrane model receives as input (Figure 18):

- the stack temperature T;
- the external current density J_{out}
- the cathode water activity $a_{H_2O,ccl}$, coming from the water GDL cathode model;
- the anode water activity $a_{H_2O,an}$, coming directly from the anode model;

The following values are calculated:

- the voltage drops across the membrane η_{el}, required to evaluate the cell voltage ΔV;
- the medium water content λ_m, defined as the ratio of the number of water molecules and the number of ionic groups SO_3^- present in the membrane;
- the net water flux flowing to cathode CCL, $N_{memb,cath}$;
- the net anode water flux $N_{memb,an}$, coming from the anode channel.

There are two main mechanism of water transport across a polymer membrane: electro-osmotic drag and back diffusion.

Electro-osmotic drag

The electro-osmotic drag refers to the flux of water molecules transferred from anode to cathode, which are dragged by the protons moving through the membrane. The amount of water transported is proportional to the so-called electro-osmotic drag coefficient η_d, which is defined as the number of water molecules carried by each proton; it has been shown that this coefficient is linearly dependent on the local water content, so the equation suggested by Springer et al.[4] has been adopted:

$$\eta_d = \frac{2.5}{22}\lambda$$

Many correlations are present in literature for the evaluation of the local water content λ as a function of the water vapour activity a_w, defined as the ratio between the water partial pressure and the saturation pression.

In this work, it has been decided to adopt the equation suggested by Weber and Newmann [31] that takes into account the Schroeder's paradox.

$$\lambda = 0.3 + 6a_w\,[1 - \tanh(a_w - 0.5)] + 5.1612\,\sqrt{a_w}\left[1 - \tanh\left(\frac{a_w - 0.89}{0.23}\right)\right]$$

The molar flux associated with this phenomenon is given by the following equation:

$$N_{H_2O,drag} = \eta_d\,\frac{J_{out}}{F}$$

Back diffusion

At cathode catalyst layer, water production by ORR and electro-osmotic drag may lead to a large amount of water, thus a concentration gradient may arise from CCL to ACL. This concentration gradient generates a reverse diffusive water flux in the membrane, known as back diffusion flow. Springer et al.[4] suggests the following expression to evaluate this molar flux, based on the Fick's law of diffusion

$$N_{H_2O,back\,diff} = -\frac{\rho_m}{E_w} D_w \nabla\lambda$$

Where ρ_m is the density of dry membrane, $E_w$is the equivalent molecular weight of dry membrane and D_w is the water diffusivity across the membrane. Springer et al.[4] suggest a semi-empirical expression of D_w [$\frac{m^2}{}$s] as a function of temperature.

$$D_w = D_\lambda\, exp\left[2416\,\left(\frac{1}{303} - \frac{1}{T}\right)\right]$$

$$D_\lambda = \begin{cases} 10^{-10} & if\ \lambda < 2 \\ 10^{-10}(1 + 2(\lambda - 2) & if\ 2 \le \lambda \le 3 \\ 10^{-10}\big(3 - 1.67(\lambda - 3)\big) & if\ 3 < \lambda < 4.5 \\ 1.25 * 10^{-10} & if\ \lambda \ge 4.5 \end{cases}$$

Combining the two contributes and approximating the water concentration gradient to be linear over the membrane thickness t_m, it is possible to quantify the net water flow across the membrane, considering positive values in the direction from anode to cathode.

$$N_{mem} = \left[\eta_d \frac{J_{out}}{F} - \frac{\rho_m}{E_w}\frac{D_w}{t_m}(\lambda_{cath} - \lambda_{an})\right] \times A_{to\ GDL}$$

Then, with the aim of achieving a higher model precision, the membrane has been ideally divided into two blocks; in each block both electro-osmotic drag and back diffusion fluxes have been evaluated, and the difference between these two net flows is equal to the accumulation term, which acts like an ideal capacitor placed in between the two. The equations implied are:

$$N_{memb,an} = \left[\eta_{an}^{d}\frac{J_{out}}{F} - \frac{2\rho}{E_w}\frac{D_w}{t_m}(\lambda_m - \lambda_{an})\right] \times A_{to\ GDL},\quad \eta_{an}^{d}\ and\ D_w\ values\ at\ \frac{\lambda_m + \lambda_{an}}{2}$$

$$N_{memb,cath} = \left[\eta_{cath}^{d}\frac{J_{out}}{F} - \frac{2\rho}{E_w}\frac{D_w}{t_m}(\lambda_{cath} - \lambda_{mem})\right] \times A_{to\ GDL},\quad \eta_{cath}^{d}\ and\ D_w\ values\ at\ \frac{\lambda_m + \lambda_{cath}}{2}$$

Then the mass conservation equation has been implemented and solved:

$$N_{H2O,acc} = \frac{\varepsilon\rho}{E_w} t_m \frac{d\lambda_m}{dt} = N_{memb,an} - N_{memb,cath}$$

The lumped water content evolution on time $\lambda_m = f\ (t)$ can be estimated, and by means of that, the membrane conductivity σ can be evaluated to determine the extent of ohmic losses.

Ohmic loss

η_{el} represents the ohmic loss due to the resistance of the polymer membrane to transfer of protons from the negative pole of the cell to the positive one. The voltage drop that corresponds to this loss is proportional to the current density:

$$\eta_{el} = R_m J_{out}$$

R_m is the membrane resistance, which can be expressed with the ratio between t_m , which is the membrane thickness, and σ, that is the membrane conductivity.

$$R_m = \frac{t_m}{\sigma}$$

The membrane conductivity σ is a function of the medium water content in the membrane λ_m, which is defined as the ratio of water molecules to the number of charge ($SO_3^- H^+$) sites and the cell temperature T, by means of the following semi-empirical equation [4]

$$\sigma = (0.005139\ \lambda_m - 0.00326) \exp\left[1268\ \left(\frac{1}{303} - \frac{1}{T}\right)\right]$$

2.2.4 Channels

Cathode Channel

The cathode channel model consists of a mass balance equation, which considers all the fluxes exchanged in the control volume. The mass flows exchanged with the MEA are $\dot{N}_{O2,GDL}$, that is the flux of oxygen is required at cathode CL by the ORR, $N_{H_2O,GDL}$, that is the water flux entering the channel. The schematic representation of the inputs and output of the model is shown in Figure 19:

Figure 19 cathode channel model scheme

The block receives as inputs:

- the oxygen and water partial pressure entering in the channel $y_{O_2,ch,in}$ and $y_{H_2O,ch,in}$;
- the inlet air molar flux $\dot{N}_{air,in,ch}$;
- the inlet oxygen flow rate $\dot{N}_{O2,GDL}$, which comes from the GDL;
- the water flux throughout the GDL $\dot{N}_{H2O,GDL}$, calculated in the water GDL model;
- the temperature of the stack T;
- the pressure of the stack P, which is the output of the compressor-manifold model;

The main outputs of the block are:

- the oxygen activity of the channel $a_{O_2,ch}$,
- the outlet air molar flux $\dot{N}_{air,ch,out}$, implied in the humidifier model;
- the water molar fraction in the channel $y_{H_2O,ch}$

Under the assumptions that species behave as ideal gases, the moles of a specie i can be simply written as:

$$N_i = \frac{PVy_i}{RT}$$

Three equations have been implemented in the model, the oxygen mass balance, the water mass balance, and the global one.

$$\frac{dN_{O2}}{dt} = \frac{P_{ref}V}{R}\frac{d}{dt}\left(\frac{a_{O2,ch}}{T}\right) = \dot{N}_{O2,in,ch} - \dot{N}_{O2,out,ch} - \dot{N}_{O2,GDL}$$

$$\frac{dN_{H2O}}{dt} = \frac{P_{ref}V}{R}\frac{d}{dt}\left(\frac{a_{H_2O,ch}}{T}\right) = \dot{N}_{H_2O,in,ch} - \dot{N}_{H_2O,out,ch} + N_{H_2O,GDL}$$

$$\frac{dN_{air}}{dt} = \dot{N}_{air,in,ch} - \dot{N}_{O2,GDL} + \dot{N}_{H2O,GDL} - \dot{N}_{air,out}$$

Anode Channel

In the anode channel a flux of hydrogen with a defined relative humidity is flowing. It comes with a precise value of pressure P_{an}, determined by the presence of the hydrogen tank and its valve, not modelled in this thesis. As for the cathode channel model, the anode channel model takes into account all the fluxes involved, the inlet fluxes, the amount of hydrogen required by the anode CL to perform the HOR $\dot{N}_{H2,HOR}$, the anode net water flow $\dot{N}_{memb,an}$, the mass accumulated in the volume and the outlet fluxes. The block representing the inputs and output of the model is shown in Figure 20:

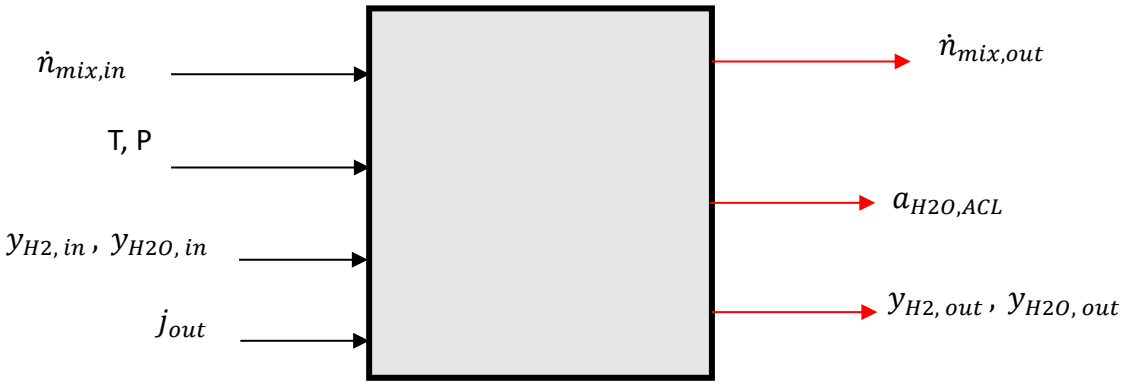

Figure 20 anode model scheme

The quantities required by the block are:

- the molar flux of hydrogen mixture required by the anode $\dot{N}_{an,in}$, that is a function of the external current density required by the power model

$$\dot{N}_{an,in} = \frac{A_{to\ GDL}\, J_{out}\, \lambda_{an}}{2F\, y_{H2,in,an}}$$

Where λ_{an} is the hydrogen stoichiometry ratio, and $y_{H2,in,an}$ is the inlet molar fraction of hydrogen.

- the net anode water flux $\dot{N}_{memb,an}$, coming from the membrane model; it is considered as a negative contribute, as water fluxes across the membrane are considered positive when directed from anode to cathode;
- the inlet water activity at the anode channel $a_{H_2O,an,in}$, defined as

$$a_{H_2O,an,in} = \frac{RH_{an}\, P_{sat}(T)}{P_{ref}}$$

- the temperature of the stack T
- the external current density J_{out}
- the anode pressure P_{an}, from which it is possible to evaluate $y_{H_2O,an,in}$ and $y_{H2,in,an}$:

The outputs of the model are:

- the water anode activity in the channel $a_{H_2O,an}$, required by the membrane;
- the outlet anode molar flux $\dot{N}_{an,out}$
- the hydrogen activity in the anode channel a_{H_2}, needed by the anode CL model, simply evaluated as

$$a_{H_2} = 1 - a_{H_2O,an}$$

The following mass conservation equations, under the assumption of ideal mixture of ideal gases, have been implemented: the water mass balance and the global mass conservation equation.

$$\frac{dN_{H2O}}{dt} = \frac{P_{ref}V}{R}\frac{d}{dt}\left(\frac{a_{H_2O,an}}{T}\right) = \dot{N}_{H2O,in,ch,an} - \dot{N}_{memb,an} - \dot{N}_{H2O,out,ch,an}$$

$$\frac{dN_{mix}}{dt} = \dot{N}_{an,in,ch} - \dot{N}_{H2,HOR} - \dot{N}_{memb,an} - \dot{N}_{an,out,ch}$$

2.3 Energy Model

Thermal management is a key aspect which affects the performance of the FC stack. As water saturation pressure is a non-linear function of temperature, water management is closely linked to thermal management. Moreover, temperature affects equilibrium and kinetic properties.

Various phenomena are responsible for heat production in the FC:

- Ionic resistivity of the membrane $Q_{mem} = \frac{{j_{cell}}^2}{\sigma_{mem}}$
- Ionic resistivity of the current collector $Q_{cc} = \frac{{j_{cell}}^2}{\sigma_{cc}}$. This effect is neglected in the model.
- Electrochemical reactions: even in fully reversible conditions, both oxygen reduction at cathode and hydrogen oxidation at anode side produce heat. In the current model, heat production is associated to ORR reaction since overpotential of HOR is negligible.
- Water sorption and desorption at the GDL/membrane interfaces: being water liquid in the membrane layer and gaseous in the backing layers, sorption and desorption phenomena are responsible for heat production and absorption, respectively. As liquid water formation has not been modelled, this thermal effect has not been considered, and the hypothesis that heat production and absorption compensate has been made.

The heat produced is rejected through the cooling system, in order to keep the stack temperature within a proper range of $70 - 90\,°C$. The higher temperature is limited by material properties, while lower temperature worsens the kinetics of the reaction.

The dynamic thermal model solves the following equation:

$$C\frac{dT_{st}}{dt} = \frac{j_{out}}{2F}\left(\Delta H_{HOR} - (E^{+} + \eta^{+})\right) - \frac{{j_{cell}}^2}{\sigma_{mem}} - \dot{Q_{cool}}$$

T_{st} is assumed to be the same along per each channel layer, neglecting the temperature gradient along the plane direction, so that the temperature at the Bipolar Plates is assumed to be equal to the temperature of the MEA. Thermal model has been solved along all the discretized control volumes in the flow direction, as different local properties affect heat generation.

The thermal capacitance of the cell has been estimated as the sum of materials and gases thermal capacitances present in each component of the cell.

The heat produced by the cell is rejected by liquid coolant which passes though cooling channels. A deep investigation of cooling geometry, which strongly affect the performance, would require a 3D analysis of different configurations. The model approximates the cooling path as a series of tubes parallel to channel tubes in which the coolant flows inn co-flow configuration with the cathode flow direction. A deeper explanation of coolant side is in chapter 3.

2.4 Model Validation

2.4.1 Calibration of polarization curves

Simulink *Parameter Estimation* toolbox has been used to fit simulated with measured data. It uses optimization techniques to estimate model parameters: in each optimization iteration, it simulates the model with the current parameter values. It computes and minimizes the error between the simulated and measured output until it finds a minimum local.

In this analysis, fitted parameters and parameters used to estimate and validate the model with experimental data are:

- Kr: cathode kinetic constant;
- Alfa: charge transfer coefficient;
- Oxygen Diffusivity through the GDL;
- Membrane conductivity;

A clear and methodical procedure has been adopted to fit the model with experimental data:

1. Fitting of the reference curve (at Stack Pressure of 2 bar, Temperature 80°C and RH cat 30%)
2. Fitting of Oxygen Diffusivity by varying RH;
3. Fitting of Oxygen Diffusivity and Kr by varying Temperature;
4. Linear Regression to find a linear relation between the Fitted Parameters and external properties;
5. Fitting of a Pol-Curve of an Automotive Fuel Cell: Adjustment of the functions to include improvements.

Validation is performed against experimental data recorded in a previous work. The membrane type employed for experiments is Nafion XL. It is mechanically reinforced through the addition of a microporous PTFE-rich support layer. Shi et al. [32] concludes that this reinforcement is responsible of a smaller increase in water uptake with respect Nafion 212 and, therefore, the effective through-plane length of membrane needs to be increased than the geometrical one to consider this effect. An addition of 10 μm is assumed to geometrical length of Nafion XL, equal to 27.5 μm.

First, the reference curve has been fitted by varying all the parameters involved (Figure 21) The reference curve has been recorded at cathode inlet RH of cat 30%, temperature 80°C and pressure 2bar.Fitted parameters values are reported in Table 1

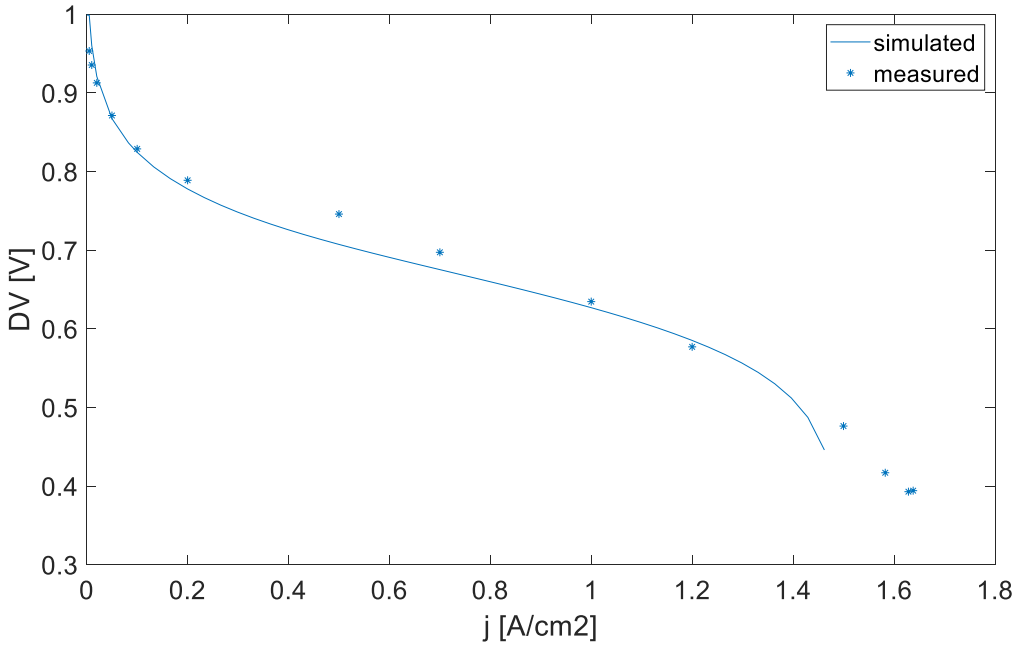

Figure 21 Reference curve fitting

Fitted Parameters	After Fitting
Kr	117
Alfa	0.55
Oxygen Diffusivity through the GDL [m2/s]	1.675e-6
Membrane Conductivity gain coefficient	1.67

Table 1 Fitted parameters values

Curves at different RH, temperature and pressure have been fitted by varying the GDL diffusivity, while by changing temperature both Diffusivity and Kr were fitted.

Figure 23, Figure 24 and Figure 25 show that the model replicates quite well the experimental trends of the polarization curves at different operating conditions. An experimental correlation has been found which expresses the oxygen diffusivity in the GDL as a function of the mean RH in cathode channel, temperature and pressure by using the *Regress* function in MATLAB. Linear regression results:

$$D_{O2,GDL} = {D_{O2,GDL}}^{0} + k_1\left(\overline{RH}_{ch} - {\overline{RH}_{ch}}^{0}\right) + k_2(T - T^0) + k_3\left(\frac{P}{P^0} - 1\right)$$

The fitting coefficients are reported in Table 2

Parameter	Value
$D^0\ \left[m^2/s\right]$	1.88E-6
RH^0	0
$T^0\ [K]$	353.15
$P^0\ [bar]$	1
k_1	1.7018E-7
k_2	2.89E-9
k_3	-2.14E-7

Table 2 fitting coefficients

Finally, the experimental relation and the new fitted parameters were used to validate the simulated polarization curve when passing to automotive geometric typical lengths, reported in Table 3

Geometry	Before	Automotive
A mem	25 cm^2	237 cm^2
N ribs	3	15
Membrane thickness	30 µm	10 µm
Nr. Cells	1	370

Table 3 Geometric parameters PEMFC

The new Diffusivity equation becomes:

$$D_{O2,GDL,AUTOMOTIVE} = 1.5 * D_{O2,GDL}$$

Figure 22 shows that the simulated polarization curve fits quite well a typical automotive polarization curve:

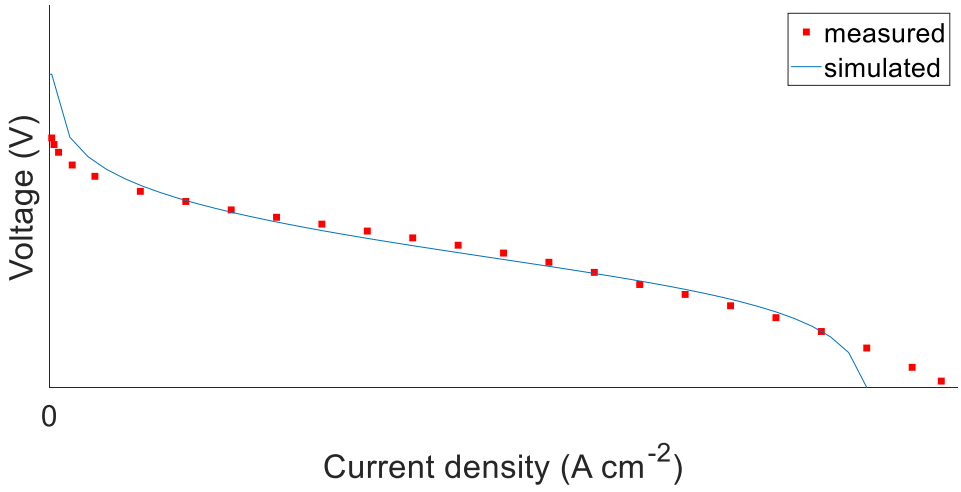

Figure 22 polarization curve typical of automotive operation

2.4.2 Effect of operating parameters

The effect of operating temperature, pressure and inlet cathode relative humidity has been investigated in this section, with the aim to understand the extent of the change of the polarization curve, representative of the change in performance of the cell, with respect to the change of operating parameters.

Effect of operating temperature on fuel cell performance

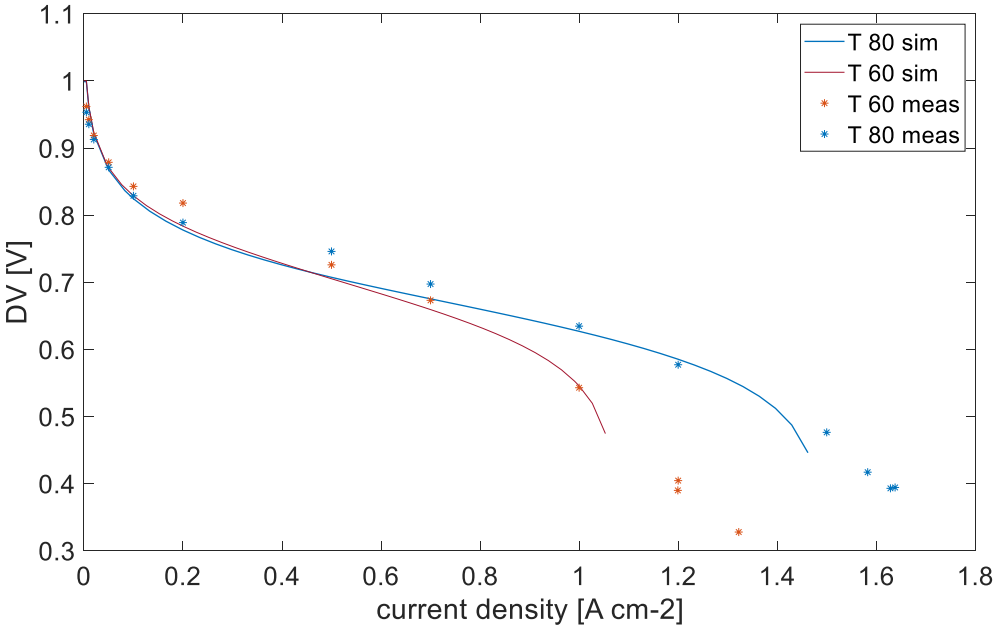

Figure 23 Temperature effect on PEMFC performance

Figure 23 illustrates the polarization curves of a fuel cell at operating temperatures of $60°C$ and $80°C$, with anode and cathode stoichiometric ratio of 2-4, respectively. These curves indicate that FC performance (higher voltage, higher limiting current) improves with increasing temperature. This increase is linked with the increase in gas diffusivity and membrane conductivity at higher temperatures.

Literature suggests the existence of an optimal temperature $\sim 80°C$ which maximises fuel cell performance [33]:

- Water more easily condenses at lower temperatures: water flooding worsens gas transport through the GDL/CL. Thus, gas diffusivity is improved at higher temperatures;
- Membrane conductivity decreases at higher temperatures because of the decrease in relative humidity of reactant gases which reduces the water content in the membrane.

The ionic resistance increases as the membrane dries out and this leads to a reduction of current and water production. The reduced water production causes the membrane to dry out even faster.

Effect of pressure on fuel cell performance

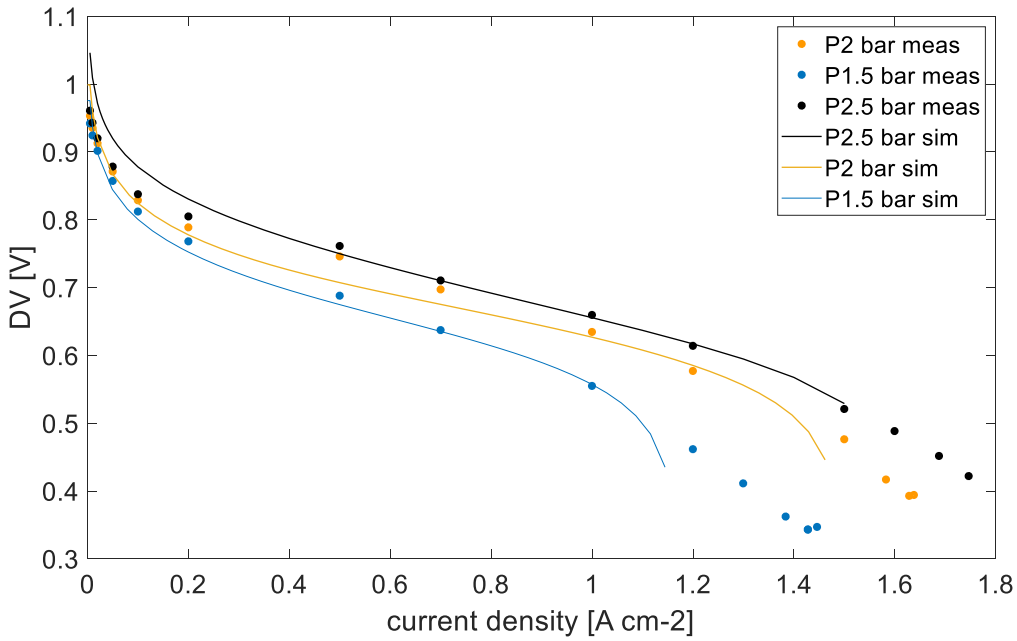

Figure 24 effect of pressure on PEMFC performance

The operating pressure affects several transport parameters, which are crucial for the fuel cell operation. The pressure of anode and cathode sides were kept the same in this analysis. Figure 24 illustrates that an increase in the pressure shifts the polarization curve up, increasing the potential at the same current. Moreover, the limiting current increases with increasing pressure. In fact, the operating pressure leads to [34]:

- Partial pressure of the reactant gases increases with increasing operating pressure;
- Open circuit voltage increases with increasing pressure, but this variation would have small effect;
- Higher pressure helps to force the oxygen and hydrogen into contact with the electrolyte, which leads to a reduction of the mass transport loss.

Effect of Cathode Relative Humidity on fuel cell performance

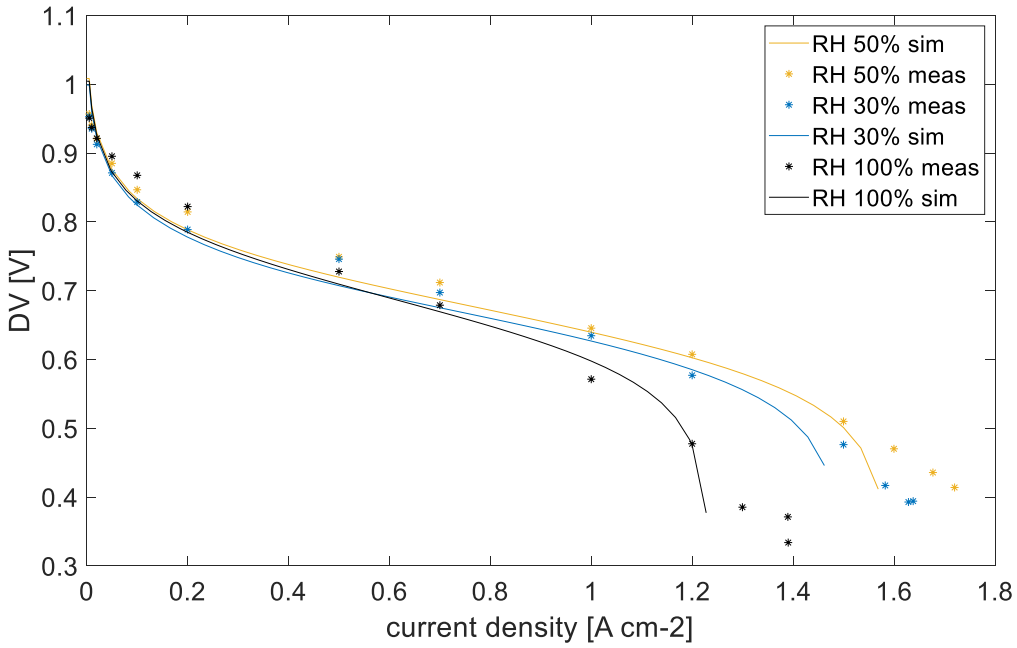

Figure 25 Effect of cathode relative humidity on FC performance

Figure 25 illustrates that the cell performance increases with increasing relative humidity of air at low current density. However, limiting current increases by decreasing relative humidity [35].

- Membrane ion conductivity linearly depends on the average water uptake. At fixed anode inlet RH, the increasing cathode inlet RH increases average membrane uptake, thus reducing membrane ionic resistance. Performance improves at low current density.
- Cathode reaction side accumulates liquid water which blocks pores and prevents oxygen from reaching the active sites of the CL: water flooding effect is reduced when RH cathode decreases, which leads to an improvement of cell performance at low voltage.

2.4.3 Dynamic Fitting

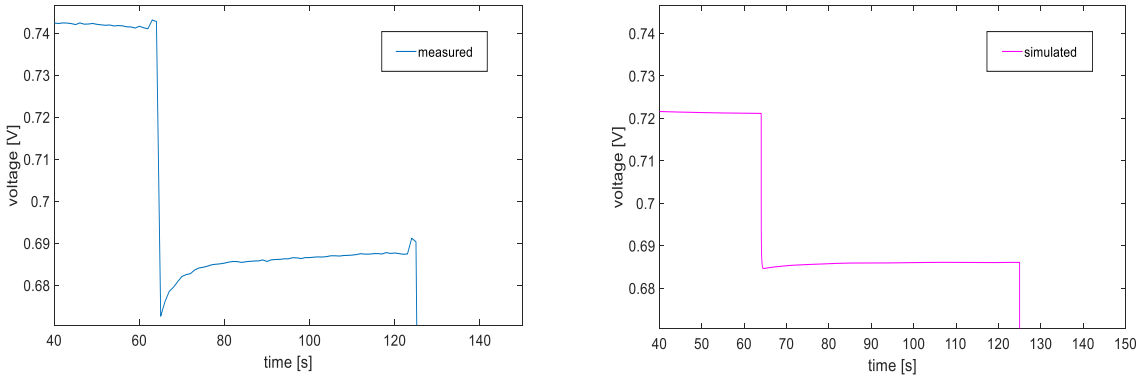

Figure 27 undershoot behaviour comparison simulated and measured voltage difference

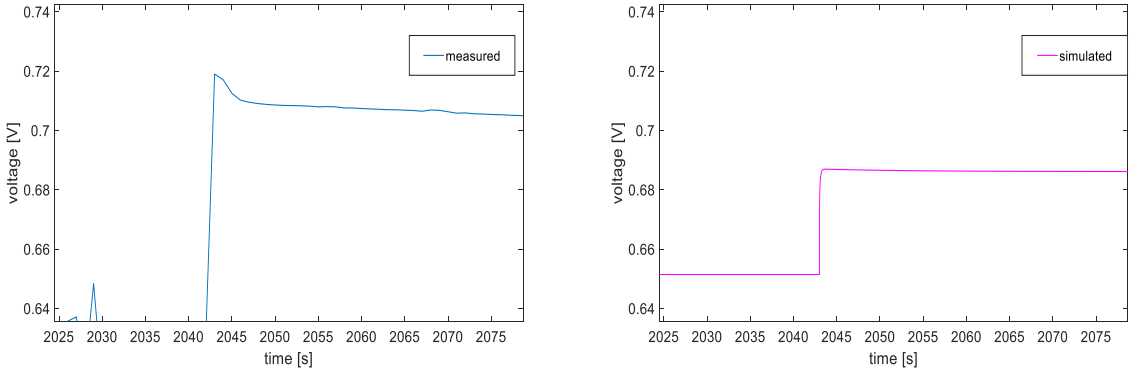

Figure 26 overshoot behaviour comparison simulated and measured voltage difference

The typical response of fuel cell voltage to a step change in external load is captured by the model: Figure 27 shows that after a step increase in current, voltage initial drop (*undershoot*) is then recovered and the cell reaches its steady-state value. The magnitude of voltage undershoot is $20 - 30\ mV$ and the recovery period may last for several seconds, depending on the step size and operating conditions. Figure 26, instead, captures that after a step decrease in current, instead, voltage immediately increases (*overshoot*), then it takes few seconds to settle down to its steady-state value. Literature identified several mechanisms as responsible for these transient responses. A relationship between voltage undershoot/overshoot and the change in membrane water content has been captured [36]:

- The primary mechanism for voltage undershoots is the dry-out of the membrane at the anode side: it causes an instantaneous decrease of membrane ion conductivity. Back-diffusion of water from the cathode helps in hydrating membrane, leading to a gradual recovery of cell voltage.

- Overshoot, instead, is linked with excess water present in the membrane after a step downwards in current, causing a period of high ionic conductivity. As excess water flows out of the membrane, voltage gradually decreases and reaches its steady state value.

Many other phenomena are responsible for transient behaviour. The discrepancy between the model results and the experimental results can be explained by analysing the impact of five assumptions made on the dynamics of the cell:

- The effect of cathode catalyst layer thickness;
- Effect of liquid water transport;
- Effect of temperature gradient within the cell;
- Effect of Balance of Plant transients;

Effect of cathode catalyst layer thickness

The model assumes the catalyst layers to be an interface. This assumption is acceptable as catalyst layers are $5-10\,\mu m$ thin, but species transport is the most complex due to the presence of multiple phases in the active sites. When the current increases, flux of protons together with molecules of dissolved water flow through the membrane, from anode to cathode. At cathode catalyst layer side, the humidity is higher near the membrane, and the reaction tends to occur close to it. It means that electrons and oxygen molecules need to move through a longer path to let the reaction occur. It results in a higher overpotential, with a local decrease in voltage.

Effect of cathode flooding

The present work assumes equilibrium rate of water uptake by the membrane. The actual concentration of water is assumed to be equal to the equilibrium concentration of water in the membrane. Thus, the contribution of liquid water has been neglected in the model. When liquid water is formed, major transport limitations occur in the GDL: the presence of liquid water blocks the pores and limits oxygen gas transport. [36].

Effect of temperature gradient within the cell

This work assumes the temperature to be the same along the MEA direction per each channel discretization. Since temperature gradient of few degrees from the hottest site to the bipolar plate, this assumption is acceptable.

But then the reaction occurs, locally the temperature at the CCL performs a pick, which dries the CCL more, leading to a decrease of CCL conductivity.

Effect of Balance of Plant transients

Even if experiments are carried out by anticipating/delaying the change at the air intake system with respect to the upwards/downwards step change in current to minimize the effect of air supply delay, this effect may not be negligible and may influence the transients. Instead, the model assumes instantaneous change in air supply during the step change.

Chapter 3. System model

In this section the models of the main components forming the balance of plant are presented. In Figure 28, a general scheme showing the principal interactions between each single model is shown. The chapter is organized as follow:

- First, the vehicle model is presented: it converts the speed vehicle in power required by the stack;
- Then, all the component models involved in the air loop are discussed. After the compression, the inlet air flows in the supply manifold; since the air required by the stack is typically lower than the one developed by the compressor, a bypass valve is needed. Then, once humidified, the air enters the stack, where the power requested by the vehicle model is produced. The air flow exiting the stack enters the wet side of the humidifier and, once mixed with the air bypassing the humidifier+stack system, it reaches the return manifold.
- At the end, the models involved in the cooling system are explained. The thermal power generated by the stack is removed by the cooling system; the heat exchange between the stack and the coolant is discussed in the thermal model. Then, the radiator model and the vehicle air flow and fan model are presented.

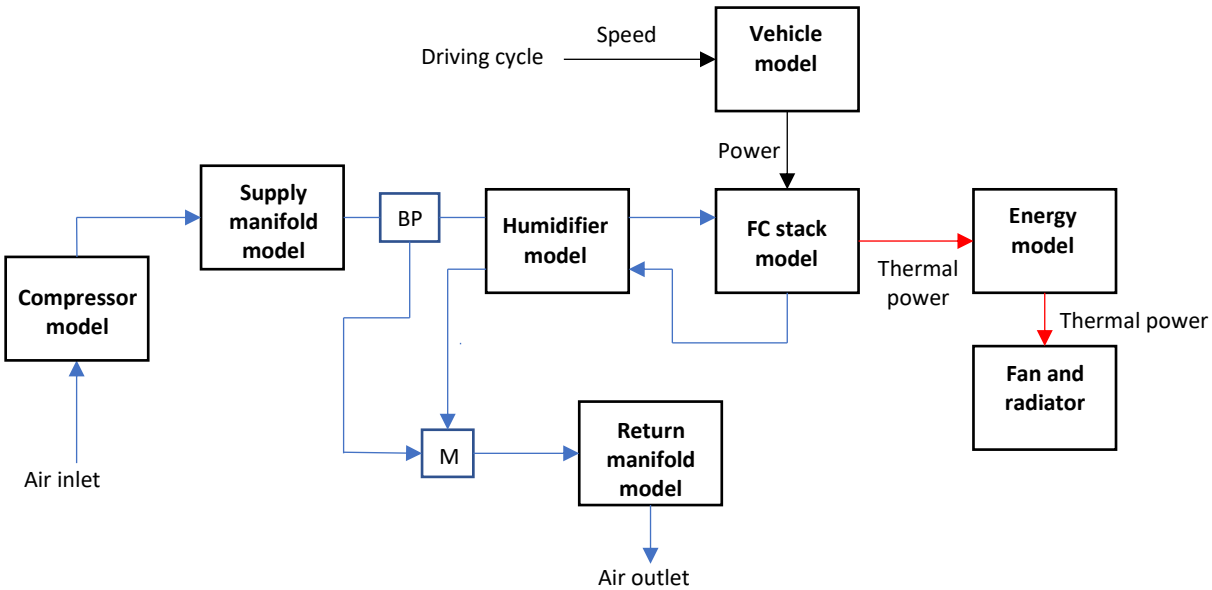

Figure 28 PEMFC system model interactions

3.1 Vehicle model

A vehicle model is required to convert vehicle speed from common driving cycles into power required by the fuel cell stack. For this work a backwards facing driveline model has been used. The model receives the vehicle speed time trace, coming from the driving cycle, and gives as output the power required by the fuel cell stack [16].

The following relation is used to evaluate the tractive effort F_t, which is the force required by the vehicle to achieve a desired speed V:

$$F_t = m\frac{dV}{dt} + \frac{1}{2}\rho C_D A_f V^2 + mga_{tyre} + Vb_{tyre} + mg\ sin\theta$$

Where m is the vehicle mass, ρ is the air density, C_D is the vehicle drag coefficient, A_f is the vehicle frontal area, a_{tyre} and b_{tyre} are the tyre friction coefficients and θ is the road gradient, not considered in this analysis. The parameters used in this equation are reported in Table 4. Then the net power required by the vehicle is evaluated as:

$$P_{vehicle} = \frac{F_t V}{\eta_{trasm}}$$

The total transmission efficiency is set to 85 %, based on typical efficiencies for the DC/DC converter and motor. The fuel cell stack must provide also the power required by the auxiliaries, mostly the power absorbed by the compressor (which represents the most relevant share) and the power required by the fan. A constant share of 500 W is considered, which accounts for all the other auxiliaries involved in the system. The effective power required by the stack is:

$$P_{stack,eff} = P_{vehicle} + P_{compr} + P_{fan} + P_{const,aux}$$

The fuel cell stack model finds the proper conditions of current density and voltage which ensures the desired power. The vehicle model used assumes that all the power required by the vehicle is supplied only by the fuel cell stack, even if in practice the fuel cell is typically hybridized with a battery to smooth transient load profiles and to improve the operation of the powertrain. Future works will deal with this aspect, which was not investigated in this work. Moreover, to prevent the request for negative currents during the deceleration phase, $P_{vehicle}$ is restricted to positive values only, so that the minimum effective power requested by the stack is the one required by the auxiliaries. Main parameters are reported in Table 4:

Parameter	Value
m [kg]	1500
a_{tyre} [-]	0.01
b_{tyre} [-]	0.01
C_D [-]	0.33
A_f [m2]	2.2

Table 4 vehicle model experimental parameters

3.2 Compressor Model

The compressor model is composed by two parts, the first is a static compressor map which determines the compressor efficiency, the compression ratio and the air flow rate. Then, these values are needed in the second part, which represents the compressor and motor inertia; therefore, the compressor speed is evaluated, used in the compressor map to find the air mass flow rate. The approach proposed by [2] is followed.

Compressor model map

The inputs of the block are:

- the compressor blade tip speed U_c;
- the pressure in the supply manifold P_{sm};

while the outputs are:

- the air mass flow rate $\dot{m}_{cp}$;
- the compressor ratio β, which can be defined as the ratio between the pressure in the supply manifold, equal to the exiting pressure of the compressor, and the inlet pressure in the machine.

$$\beta = \frac{p_{sm}}{p_{cp,in}} = \frac{p_{cp,out}}{p_{cp,in}}$$

- the compressor efficiency η_{cp};

Supplying the compressor flow map in the form of a lookup table is not well-suited for dynamic simulations, since the data extrapolation is not reliable [37]. Therefore, a nonlinear curve fitting method is used to model the compressor characteristics; the Jensen & Kristensen method [38] has been implied in this model. The dimensionless head parameter ψ has been evaluated as:

$$\psi = \frac{c_p\, T_{cp,in}\left(\beta^{\frac{\gamma-1}{\gamma}} - 1\right)}{\frac{1}{2}U_c^2}$$

Where c_p is the air specific heat at constant pressure, $T_{cp,in}$ is the inlet compressor temperature, $p_{cp,in}$ is the inlet compressor pressure, equal to the ambient pressure, $p_{cp,out}$ is the outlet compressor pressure and γ is the ratio between the specific heat at constant pressure and the one at constant volume. Then, the normalized compressor flow rate Φ has been defined:

$$\Phi = \frac{\dot{m}_{cr}}{\rho_{air}\ \frac{\pi}{4}\ D^2\ U_c}$$

In particular $\dot{m}_{cr}$ is the corrected air mass flow rate, defined as $\dot{m}_{cr} = \dot{m}_{cp}\sqrt{\theta}$, where θ is the corrected temperature, with $\theta = T_{cp,in}/288\ K$; these corrected values are used so to reflect the eventual variations of the inlet conditions of the compressor. The other parameters involved are the air density ρ_{air}, the compressor diameter D and the compressor blade tip speed U_c. Since the air mass flow rate is unknown, a relation between the normalized compressor flow rate Φ and the dimensionless head parameter ψ is required:

$$\Phi = \Phi_{max}\left[1 - e^{\beta_{mach}\left(\frac{\psi}{\psi_{max}} - 1\right)}\right]$$

Where Φ_{max}, β_{mach} and ψ_{max} are polynomial functions of the inlet Mach number M

$$\Phi_{max} = a_4M^4 + a_3M^3 + a_2M^2 + a_1M + a_0$$

$$\beta_{mach} = b_2M^2 + b_1M + b_0$$

$$\psi_{max} = c_5M^5 + c_4M^4 + c_3M^3 + c_2M^2 + c_1M + c_0$$

The inlet Mach number is defined as

$$M = \frac{U_c}{\sqrt{\gamma\ R_{air}\ T_{cp,in}}}$$

Where R_{air} is the air gas constant. The regression coefficients a_i, b_i and c_i are obtained by curve fitting of the compressor map of an Allied Signal Compressor for automotive

application, given in Table 5 [38]. So, once evaluated Φ_{max}, β_{mach}, ψ_{max}, and ψ,, the air mass flow rate can be easily calculated.

Parameter	Value
a_4	-3.69906 × 10^{-5}
a_3	2.70399 × 10^{-4}
a_2	-5.36235 × 10^{-4}
a_1	-4.63685 × 10^{-5}
a_0	2.21195 × 10^{-3}
b_2	1.76567
b_1	-1.34837
b_0	2.44419
c_5	-9.78755 × 10^{-3}
c_4	0.10581
c_3	-0.42937
c_2	0.80121
c_1	-0.68344
c_0	0.43331

Table 5 compressor model regression coefficients

Compressor efficiency model

The third output of the compressor map model is the compressor efficiency. In this thesis the Casey and Robinson approach for the design of centrifugal compressor characteristics has been used [39]. The compressor performance is based on the evaluation of four key nondimensional parameters, the normalized flow rate (also called flow coefficient) Φ, the dimensionless head ψ, the inlet Mach number M and the compressor efficiency η_{cp}, rather than the geometry of the machine. This method can be applied to a wide range of stage types, but the attention has been mainly focused on the turbocharger style impellers with vaneless diffusers, a typical solution adopted in the automotive sector. The following relation between efficiency, flow coefficient and inlet Mach number, suggested by Rodgers[39], has been used

$$\frac{\eta_{cp}}{\eta_{cp,peaak}} = f\left(\frac{\Phi}{\Phi_c}, M\right)$$

Where $\eta_{cp,peaak}$ is the compressor peak efficiency, equal to 0.8, and Φ_c is the chocked flow coefficient, equal to Φ_{max} .The relation, useful to calculate the compressor efficiency, depends on the ratio between the flow coefficient Φ and the flow coefficient evaluated at the peak efficiency, Φ_{peak}

$$if\ \frac{\Phi}{\Phi_{peak}} < 1, \qquad \frac{\eta_{cp}}{\eta_{cp,peaak}} = \left[1 - \left(1 - \frac{\Phi/\Phi_c}{\Phi_{peak}/\Phi_c}\right)^D\right]^{\frac{1}{D}}$$

$$if\ \frac{\Phi}{\Phi_{peak}} > 1, \qquad \frac{\eta_{cp}}{\eta_{cp,peaak}} = \left[(1-G) + G\left(1 - \frac{\Phi/\Phi_c - \Phi_{peak}/\Phi_c}{1 - \Phi_{peak}/\Phi_c}\right)^H\right]^{\frac{1}{H}}$$

Where:

- D coefficient is related to the variation of the shape of the efficiency curve for different Mach numbers in the low flow coefficient region; it mainly considers the increase of incidence losses occurring at high speeds;
- H coefficient has a similar function to the exponent D, but it is involved in the high flow coefficient region;
- G coefficient, also function of the inlet Mach number, is necessary so that the efficiency at maximum flow coefficient Φ_c is equal to $(1 - G)$, rather than zero.

Casey-Robinson model provides the experimental asymptotic values of D, H, G, as well as $\frac{\Phi_{peak}}{\Phi_c}$, which are summarized in Table 6:

Quantity	**At low Mach numbers**	**At high Mach numbers**
D	$D_{LO} = 2.1$	$D_{HI} = 1.7$
H	$H_{LO} = 2$	$H_{HI} = 3.5$
G	$G_{LO} = 2$	$G_{HI} = 0.3$
$\frac{\Phi_{peak}}{\Phi_c}$	$\left(\frac{\Phi_{peak}}{\Phi_c}\right)_{LO} = 0.5$	$\left(\frac{\Phi_{peak}}{\Phi_c}\right)_{HI} = 0.9$

Table 6 compressor efficiency model experimental coefficients typical of turbocharger style impellers with vaneless diffusers

Then, using these coefficients it is possible to evaluate

$$D = (1 - P)D_{LO} + PD_{HI}$$

$$H = (1 - P)H_{LO} + PH_{HI}$$

$$G = (1 - P)G_{LO} + PG_{HI}$$

$$\frac{\Phi_{peak}}{\Phi_c} = (1 - P)\frac{\Phi_{peak}}{\Phi_c}_{LO} + P\frac{\Phi_{peak}}{\Phi_c}_{HI}$$

Where P is the s-shaped logistic function and varies from 0 to 1 increasing the inlet Mach number; it blends the values of the parameters given in Table 6 between the low Mach number asymptote (subscript LO) and the high Mach number asymptote (subscript HI).

$$P = \frac{1}{1 + e^{-t}}$$

Where t is function of the inlet Mach number M and 3 given experimental parameters, typical of turbocharger stages, reported in the Table 7[39]

$$t = (M - B)(AM + C)$$

Parameter	Value
A	0.05
B	1.15
C	4.5

Table 7 compressor efficiency model experimental parameters 2

So, once known the values of D, H, G and Φ_{peak}/Φ_c, the compressor efficiency can be evaluated.

Compressor and motor inertia model

The compressor and motor model is used to evaluate the compressor speed by means of a balance between the torque generated by the motor and the one required by the compressor [2]. The value required by the block are:

- The voltage required by the electric motor to drive the compressor V_{cm}: it comes from a PID controller, which regulates V_{cm} to obtain the air mass flow rate needed by the fuel cell stack. The control strategy is presented and analysed in the chapter 5. The amount of air required by the single cell to perform ORR is:

$$\dot{m}_{air,in,ch} = \frac{A_{cell}\, J_{out}\, \lambda_{cath} MM_{air}}{4F\, y_{O2,dry,in}}$$

Where λ_{cath} is the oxygen stoichiometry ratio, MM_{air} is the air molecular weight and $y_{O2,dry,in}$ is the molar fraction of oxygen in ambient air.

- The pressure in the supply manifold P_{sm},
- The air mass flow rate exiting the compressor $\dot{m}_{cp}$,
- The compressor efficiency η_{cp},
- The compression ratio β,

The outputs of the block are:

- The compressor blade tip speed U_c, needed in the compressor map model
- The outlet air temperature $T_{cp,out}$
- The power absorbed by the compressor P_{compr}

The compressor speed ω_{cp} has been evaluated by means of the following equation:

$$J_{cp} \frac{d\omega_{cp}}{dt} = \left(\tau_{cm} - \tau_{cp}\right)$$

Where J_{cp} is the inertia of the compressor-motor block, τ_{cm} and τ_{cp} are the torque given by the motor and the one required by the compressor, respectively. They can be evaluated as:

$$\tau_{cm} = \eta_{cm} \frac{k_t}{R_{cm}} \left(V_{cm} - k_v \omega_{cp}\right)$$

$$\tau_{cp} = \frac{c_{p,air}}{\omega_{cp}} \frac{T_{cp,in}}{\eta_{cp}} \left(\beta^{\frac{\gamma-1}{\gamma}} - 1\right) \dot{m}_{cp}$$

Where η_{cm} is the compressor-motor electrical efficiency, while k_t, k_v and R_{cm} are motor constants.

Experimental parameters used for the implementation of the compressor motor inertia model are reported in Table 8.

The compressor blade tip speed U_c, required in the compressor map model, is computed as:

$$U_c = \omega_{cp} \frac{D}{2}$$

Then, even the outlet air leaving the compressor can be quantified:

$$T_{cp,out} = T_{cp,in} + \frac{T_{cp,in}}{\eta_{cp}}\left(\beta^{\frac{\gamma-1}{\gamma}} - 1\right)$$

The last output of the compressor and motor inertia model is the power absorbed by the compressor, which represents the most important share in the auxiliary consumption. It can be obtained as:

$$P_{compr} = \dot{m}_{cp} c_{p,air}\left(T_{cp,out} - T_{cp,in}\right)$$

In Figure 29 compression ratio and compressor efficiency are reported at different compressor speeds. It is evident that, with the experimental parameters implemented, a minimum air mass flow rate is needed by the compressor, so to maintain an acceptable value of efficiency, and thus of air outlet temperature and power consumption. The minimum air mass flow rate has been set equal to 20 g/s.

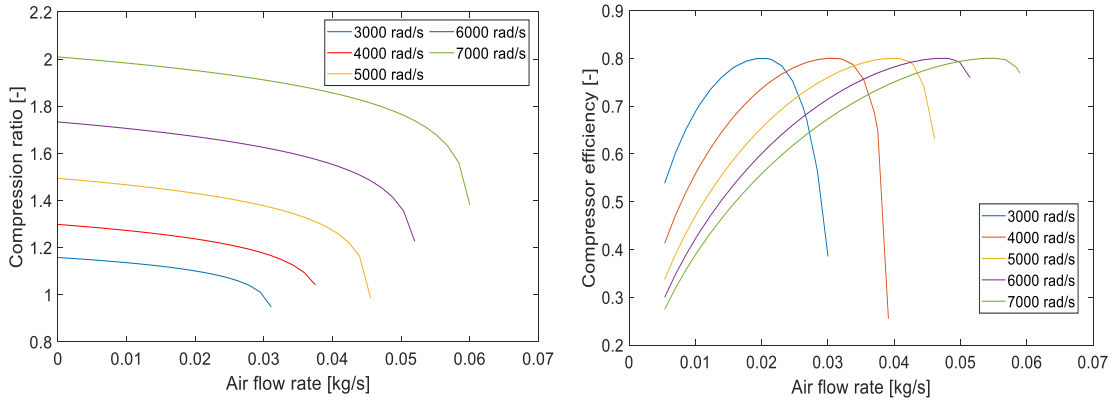

Figure 29 compression ratio and compressor efficiency for different compressor speeds.

Parameter	Value
k_v [V/(rad/s)]	0.0153
k_t [Nm/A]	0.0153
R_{cm} [Ω]	0.8298
η_{cm} [-]	0.98
D [m]	0.2286
J_{cp} [kg m^2]	5 x 10^{-5}
$V_{sm}[m^3]$	0.02
$V_{rm}[m^3]$	0.005
$C_{D,rm}[-]$	0.0124
$k_{nozzle,sm}$[kg/(Pa s)]	0.3629 x 10^{-5}

Table 8 compressor motor and manifolds parameters

3.3 Manifolds dynamic model

The manifold model represents the dynamics associated to the movement of air throughout the pipes and connections between each component. The air developed by the compressor doesn't reach immediately the stack, but it is slightly delayed by the presence of the manifolds volume. The supply manifold volume includes the volume of the pipes between the compressor and fuel cell stack, while the return manifold represents the pipeline at the fuel cell stack exhaust system. For both manifolds the mass conservation equation and the energy balance is implemented:

$$\frac{dm}{dt} = \dot{m}_{in} - \dot{m}_{out}$$

$$\rho c_{v,air} V \frac{dT}{dt} = \dot{m}_{in} c_{p,air}\left(T_{in} - T_{ref}\right) - \dot{m}_{out} c_{p,air}\left(T_{out} - T_{ref}\right)$$

Where m is the mass accumulated in the volume, V is the manifold volume, while $\dot{m}_{in}$ and $\dot{m}_{out}$ are the air mass flow rates entering and leaving the manifold, respectively. Applying the ideal gas law to the mass balance, it is possible to derive the following relation:

$$\frac{V}{R_{air}} \frac{d}{dt}\left(\frac{P}{T}\right) = (\dot{m}_{in} - \dot{m}_{out})$$

Where R_{air} is the gas constant and V is the manifold volume. Differentiating this expression, the pressure evolution can be evaluated as:

$$\frac{dP}{dt} = \frac{R_{air} T}{V}\left[(\dot{m}_{in} - \dot{m}_{out}) + \frac{P}{T^2}\frac{dT}{dt}\right]$$

The outlet flow of the manifold $\dot{m}_{out}$, which represents the third and last unknown term of the block with P and T, is calculated using the nozzle flow equation. The flow characteristic is divided into two regions, commonly named as sub-critical and critical region, by the critical pressure ratio:

$$\left(\frac{P_2}{P_1}\right)_{cr} = \left(\frac{2}{\gamma + 1}\right)^{\frac{\gamma}{\gamma - 1}}$$

Where P_2 is the downstream pressure and P_1 is the upstream one. In the case of $\gamma = 1.4$, the critical pressure ratio is equal to 0.528. If the pressure drop between the manifold and the

nozzle outlet is less than the critical pressure ratio, the flow is in sub-critical conditions and the mass flow rate is calculated from:

$$\dot{m}_{out} = \frac{C_D A_T P_1}{\sqrt{R_{air} T_1}} \left(\frac{P_2}{P_1}\right)^{\frac{1}{\gamma}} \left\{ \frac{2\gamma}{\gamma - 1} \left[1 - \left(\frac{P_2}{P_1}\right)^{\frac{\gamma-1}{\gamma}} \right] \right\}^{\frac{1}{2}} \quad for \ \frac{P_2}{P_1} > \left(\frac{2}{\gamma+1}\right)^{\frac{\gamma}{\gamma-1}}$$

C_D is the nozzle discharge coefficient and A_T is the opening area of the nozzle. For critical (or choked) flow, the following equation is used:

$$\dot{m}_{out,choked} = \frac{C_D A_T P_1}{\sqrt{R_{air} T_1}} \gamma^{\frac{1}{2}} \left(\frac{2}{\gamma+1}\right)^{\frac{\gamma+1}{2(\gamma-1)}} \quad for \ \frac{P_2}{P_1} \leq \left(\frac{2}{\gamma+1}\right)^{\frac{\gamma}{\gamma-1}}$$

If the pressure difference between the upstream and the downstream pressure is small, the flow is always in sub-critical condition, and the flow rate can be obtaining as

$$\dot{m}_{out} = k_{nozzle}(P_1 - P_2)$$

Where k_{nozzle} is the nozzle constant.
Experimental parameters used for the implementation of the manifolds' models are reported in Table 8.

3.3.1 Supply manifold model

The inputs of the supply manifold model are:

- The compressor air outlet temperature $T_{cp,out}$,
- The air flow rate leaving the compressor $\dot{m}_{cp}$,
- The stack pressure P_{stack}

While the outlet ports of the block are:

- The supply manifold pressure P_{sm}, needed in the compressor model for the evaluation of the compression ratio
- The air flow rate exiting the manifold $\dot{m}_{sm,out}$, directed to the bypass valve
- The air temperature in the supply manifold T_{sm}

Since the pressure drop between the supply manifold and the stack is very small, it can be assumed that the flow rate exiting the volume is always in sub-critical condition, and thus

the nuzzle linear equation can be implied. So, the model solves the following system of three equations:

$$\frac{dP_{sm}}{dt} = \frac{R_{air}T_{sm}}{V_{sm}}\left[\left(\dot{m}_{cp} - \dot{m}_{sm,out}\right) + \frac{P_{sm}}{{T_{sm}}^2}\frac{dT_{sm}}{dt}\right]$$

$$\rho c_{v,air} V_{sm}\frac{dT_{sm}}{dt} = \dot{m}_{cp}c_{p,air}\left(T_{cp,out} - T_{ref}\right) - \dot{m}_{sm,out}c_{p,air}\left(T_{sm} - T_{ref}\right)$$

$$\dot{m}_{sm,out} = k_{nozzle,sm}(P_{sm} - P_{stack})$$

So P_{sm}, T_{sm} and $\dot{m}_{sm,out}$ can be easily calculated.

3.3.2 Return manifold model

The return manifold model receives as inputs the inlet mass flow rate $\dot{m}_{rm,in}$ and the inlet temperature $T_{rm,in}$, , giving the stack pressure P_{stack} as the only output. Like the supply manifold model, mass and energy balance equations have been implemented, the only difference is the relation used for the evaluation of the outlet air mass flow rate: since the pressure drop between the return manifold pressure and the discharge pressure, assumed equal to P_{atm}, is relatively high, critical flow equations must to be used, instead of the linearized nuzzle equation.
So globally the blocks solve the following system:

$$\frac{dP_{rm}}{dt} = \frac{R_{air}T_{rm}}{V_{rm}}\left[\left(\dot{m}_{rm,in} - \dot{m}_{rm,out}\right) + \frac{P_{rm}}{{T_{rm}}^2}\frac{dT_{rm}}{dt}\right]$$

$$\rho c_{v,air} V_{rm}\frac{dT_{rm}}{dt} = \dot{m}_{rm,in}c_{p,air}\left(T_{rm,in} - T_{ref}\right) - \dot{m}_{rm,out}c_{p,air}\left(T_{rm} - T_{ref}\right)$$

While for the outlet air mass flow rate:

$$\dot{m}_{out,rm} = \frac{C_{D,rm}\, A_{T,rm}\, P_{rm}}{\sqrt{R_{air} T_{rm}}} \left(\frac{P_{atm}}{P_{rm}}\right)^{\frac{1}{\gamma}} \left\{ \frac{2\gamma}{\gamma - 1} \left[1 - \left(\frac{P_{atm}}{P_{rm}}\right)^{\frac{\gamma-1}{\gamma}} \right] \right\}^{\frac{1}{2}} \quad for \quad \frac{P_{atm}}{P_{rm}} > \left(\frac{2}{\gamma+1}\right)^{\frac{\gamma}{\gamma-1}}$$

$$\dot{m}_{rm,out,choked} = \frac{C_{D,rm} A_{T,rm} P_{rm}}{\sqrt{R_{air} T_{rm}}} \gamma^{\frac{1}{2}} \left(\frac{2}{\gamma+1}\right)^{\frac{\gamma+1}{2(\gamma-1)}} \quad for \quad \frac{P_{atm}}{P_{rm}} \leq \left(\frac{2}{\gamma+1}\right)^{\frac{\gamma}{\gamma-1}}$$

3.4 Bypass model

Since the air mass flow rate leaving the supply manifold is typically higher than the air mass flow rate required by the stack, a bypass valve must be placed after the supply manifold. In particular, when the power required by the stack is relatively small, and thus even the air mass flow rate needed, most of the air coming from the supply manifold is bypassed; when the power required by the stack becomes relevant, and so even the air mass flow rate required, the bypass valve is closed and all the air mass flow rate provided by the manifold enters the stack, once has been humidified. So:

$$\dot{m}_{air,dry,in,hum} = \dot{m}_{sm,out} - \dot{m}_{bypass} \qquad if\ bypass\ valve\ is\ open$$

$$\dot{m}_{air,dry,in,hum} = \dot{m}_{sm,out} \qquad if\ bypass\ valve\ is\ closed$$

3.5 Humidifier model

The model is based on a plate-and-frame membrane humidifier, with multiple membranes channels and plates. It is a heat and mass exchanger with a Nafion membrane installed in between wet and dry channels.

The model takes the air out of the FC stack as the input of the wet side and the air out of the intercooler as the inlet of the dry side. Since the model of the intercooler was not implemented, air temperature at the dry side is kept fixed to a value of 50°C, lower than the stack temperature.

Air out of the dry side enters then the FC stack, while air out of the wet side is mixed with the excess air out of the compressor before entering the return manifold.

Geometric parameters, such as the channel width, height and length were determined from previous studies [19]. Values are shown in Table 9:

Parameter	Value
Channel width [mm]	3 mm
Channel height [mm]	3 mm
Channel length [mm]	322 mm
Plate thickness [mm]	1 mm
Membrane thickness [mm]	0.03 mm

Table 9 humidifier model geometric parameters

Moreover, the number of plates and channels in a plate were determined to meet the humidification requirements of the system. Further details are reported in chapter 4.

The numerical model is based on the following assumptions:

1) Air flow is incompressible and laminar;
2) Phase change is neglected;
3) Vapor diffusion is only in the normal direction;
4) Physical properties are constant along the length of the humidifier;

Figure 30 shows a schematic representation of the computational domain of the humidifier:

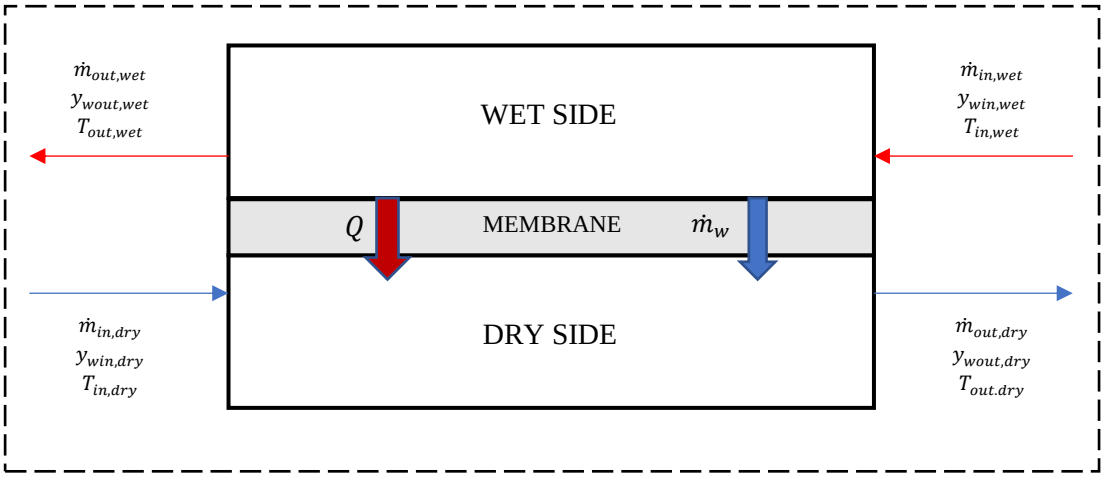

Figure 30 control volume of humidifier model

The flow rate of air through both channels is computed as:

$$\dot{m}_{w,ch} = \frac{\dot{m}_w}{n_{plates} n_{ch,plate}}$$

Heat and mass equations are defined within the framework (Figure 30), according to the hypothesis that all the modules of the humidifier have the same behaviour.[22]

The primary mechanisms for heat and mass transfer are convection in the channels and solid phase diffusion in the ionomer layer.

Ionomer phase

Water transport in the ionomer is described in terms of water uptake (λ), defined as:

$$\lambda = \frac{n_{water}}{kg_{eq}}$$

The same empirical equation of the PEMFC membrane is used to determine λ as a function of RH. Since the ionomer layer is very thin, water and heat transport in the x-direction are ignored, while the following diffusion equation describes the water transport in the y-direction:

$$\frac{\partial \lambda}{\partial t} = \frac{\partial}{\partial y}\left(D_\lambda \frac{\partial \lambda}{\partial y}\right)$$

Where membrane Diffusivity is a function of water uptake, and the same experimental equation of the membrane in the PEMFC model has been adopted.

The energy equation in the ionomer includes both heat transfer through conduction and the contribution of water transport, but ignores the effect of phase change:

$$C_m \frac{\partial T_m}{\partial t} = \frac{\partial}{\partial y}\left(k_m \frac{\partial T_m}{\partial y}\right) - MM_v J_m c_{p,v} \frac{\partial T_m}{\partial y}$$

$$J_m = -\frac{\rho_m}{EW} D_\lambda \frac{\partial \lambda}{\partial y}$$

A lumped-parameter model is adopted to solve λ and T_m at the middle of the ionomer layer.

Channel Phase

A lumped parameter model has been adopted to solve the mass and energy equations and the middle of the channel. Mass transport in e y-direction is neglected in the channel, thus the water activity at the boundary between the channel and the membrane is assumed to be equal to the water activity at the centre of the bulk flow. Mass equation in the channel describes the water transport in the x-direction:

At the wet side:

$$\frac{dN}{dt} = \dot{N}_{in} - \dot{N}_{in} - \dot{N}_{wtr}$$

$$\frac{dN_w}{dt} = \dot{N}_{w,in} - \dot{N}_{w,out} - \dot{N}_{wtr}$$

At the dry side:

$$\frac{dN}{dt} = \dot{N}_{in} - \dot{N}_{in} + \dot{N}_{wtr}$$

$$\frac{dN_w}{dt} = \dot{N}_{w,in} - \dot{N}_{w,out} + \dot{N}_{wtr}$$

The accumulation term considers the evolution of both temperature and pressure in time, as they are not constant, but they depend on thermal cooling system of the PEMFC stack and the pressure control, respectively.

On the contrary, a temperature gradient in the y-direction is considered, which includes both the effect of convective transfer but ignores the effects of phase change and water transport.

At the wet side:

$$\rho \tilde{c}_{eq} V \frac{dT_{wet}}{dt} = \dot{N}_{in} \tilde{c}_{p,eq} \left(T_{in} - T_{ref}\right) - \dot{N}_{out} \tilde{c}_{p,eq} \left(T_{out} - T_{ref}\right) - hA(T_{wet} - T\_ch_m)$$

At the dry side:

$$\rho \tilde{c}_{eq} V \frac{dT_{dry}}{dt} = \dot{N}_{in} \tilde{c}_{p,eq} \left(T_{in} - T_{ref}\right) - \dot{N}_{out} \tilde{c}_{p,eq} \left(T_{out} - T_{ref}\right) + hA\left(T_{dry} - T_{ch,m}\right)$$

Where

$$\tilde{c}_{p,eq} = y_{dryair} \tilde{c}_{p,dryair} + y_v \tilde{c}_{p,v}$$

In a fully developed laminar flow:

$$Nu = 3.61$$

$$h = \frac{NuD_h}{k}$$

Where D_h is the hydraulic diameter and k is the thermal conductivity[40].

3.6 Mixer model

Before entering the return manifold, the wet air leaving the humidifier and the mass flow rate which has bypassed the fuel cell stack are mixed together. Stationary mass and energy balance have been implemented:

$$\dot{m}_{rm,in} = \dot{m}_{air,out\ hum,wet} + \dot{m}_{bypass}$$

$$\dot{m}_{rm,in} c_p \left(T_{rm,in} - T_{ref}\right) = \dot{m}_{out,hum} c_p \left(T_{out,wet} - T_{ref}\right) + \dot{m}_{bypass} c_p \left(T_{sm} - T_{ref}\right)$$

So, the values of $\dot{m}_{rm,in}$ and $T_{rm,in}$ can be easily calculated.

3.7 Energy model

The waste heat produced by the fuel cell stack is removed by passing a liquid cooling through channels in the bipolar plates. The following hypothesis have been set:

- The heat exchange is homogeneous along the rib direction;
- The stack is assumed to be at the same temperature, as already explained in the fuel cell model;
- The heat generated by the single fuel cell stack is split equally between the anode bipolar plate and the cathode bipolar plate;
- the coolant temperature is the same among all the cooling channels.

Under these assumptions, the heat rejection in a single cell is representative for the whole stack thermal behaviour. At the coolant side, the following differential equation has been solved[41]:

$$\rho c_w V \frac{dT_{cool,out}}{dt} = \dot{m}_w c_w \left(T_{cool,out} - T_{cool,in}\right) - UA\Delta T_{ml}$$

Where $\dot{m}_w$ is the coolant flow rate divided by the number of cells, ΔT_{ml} the logarithmic temperature difference between the cell and the coolant inlet and outlet, respectively; V is the coolant channels volume and UA is the overall heat transfer coefficient[40].

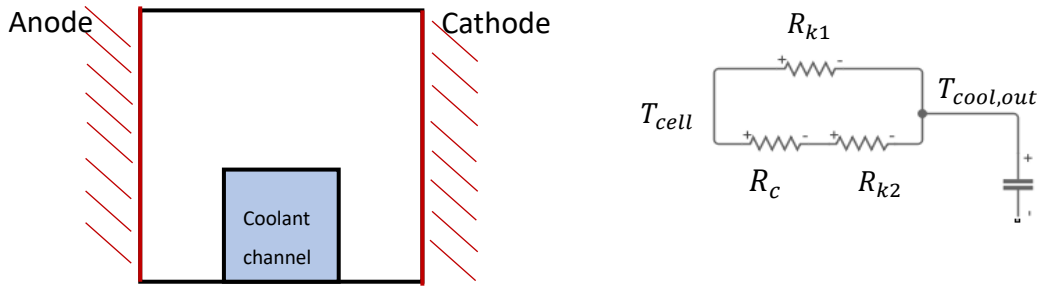

Figure 31 Energy model coolant side control volume and equivalent electric circuit

The total thermal resistance has been estimated focusing on a single rib-channel control volume (Figure 31). It is the parallel between:

- The conductive resistance across the rib:

$$R_{k1} = \frac{t_{eff,BP} + \frac{h_{ch}}{2}}{k_{gr} A_{k1}}$$

Where $t_{eff,BP}$ is the effective length of the bipolar plate, k_{gr} is the graphite conductivity and A_{k1} is the conductive heat exchange area referred to R_{k1}, defined as $A_{k1} = l_{rib}l_{ch}$ and h_{ch} is the height of the coolant channel;

- The series between a conductive resistance R_{k2} and a convective one R_c, defined as:

$$R_{k2} = \frac{t_{eff,BP}}{k_{gr}A_{k2}}$$

$$R_c = \frac{1}{h_{cool}A_{k2}}$$

Where A_{k1} is the conductive heat exchange area referred to R_{k2}, defined as $A_{k2} = w_{ch}l_{ch}$ and h_{cool} is the coolant convective heat transfer coefficient, calculated as:

$$h_{cool} = \frac{Nu\ k_{cool}}{d_h}$$

Where k_{cool} is the water conductivity, d_h is the hydraulic diameter and Nu is the Nusselt number. The thermal resistance can be evaluated as:

$$R_{th} = \left[\frac{1}{(R_{k2} + R_c)} + \frac{1}{R_{k1}}\right]^{-1}$$

Extending this analysis to the whole cell, the overall heat transfer coefficient can be written as:

$$UA = \frac{2n_{ribs}}{R_{th}}$$

The heated water exiting the fuel cell stack is cooled in the radiator and returns to a tank where it is pumped back into the fuel cell stack, closing the coolant loop. The coolant inlet temperature is controlled by means of a bypass valve, that splits the portion of the coolant flow which passes though the radiator with the coolant flow that bypasses it. Under the hypothesis of no losses, the following equation describes the by-pass valve behaviour:

$$\dot{m}_{by-pass} = \dot{m}_{cool,tot}\alpha$$

$$\dot{m}_{in,rad} = \dot{m}_{cool,tot}(1 - \alpha)$$

where α represents the percentage of the by-pass valve opening. When the cooled water exits the radiator, it enters the mixer together with the uncooled by-pass flow. The temperature out of the mixer is simply calculated as:

$$T_{cool,in\ stack} = \frac{\dot{m}_{in\ rad}c_pT_{out,rad} + \dot{m}_{bypass}c_pT_{out,stack}}{\dot{m}_{cool}c_p}$$

When the amount of thermal energy to remove is consistent, a fan in needed so to increase the air velocity across the radiator and thus the convective heat coefficient of the air side. In this section the radiator model and the vehicle air flow model, including the fan, are presented, while the discussion on the thermal control strategy is addressed in the chapter 5.

3.8 Radiator model

The liquid radiator has been modelled as a one-dimensional cross flow louvered fin heat exchanger, the hot side is the cooling fluid exiting the fuel stack cooling system (deionized water), while the cold side is forced air at ambient temperature. The approach proposed by [42] has been adopted.

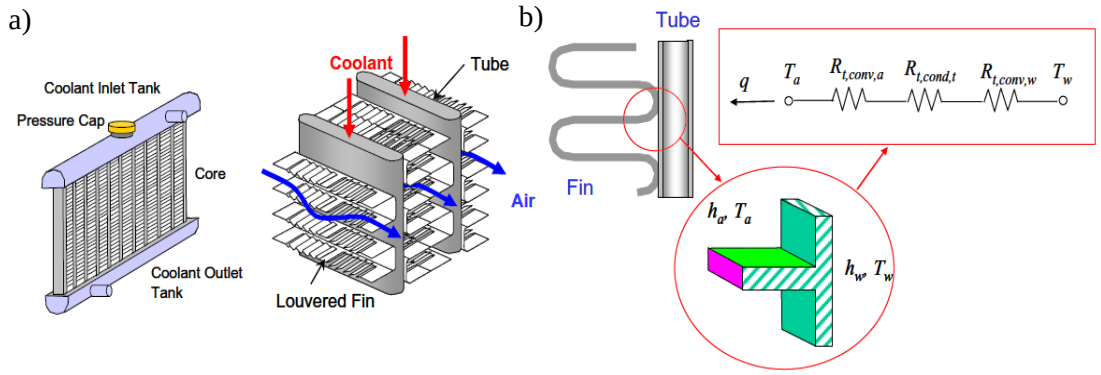

Figure 32 Radiator model scheme (a) and equivalent electrical circuit (b) [42]

Geometry used refers to a typical radiator for FCEV application. Values are shown in Table 10:

Parameter	**Value**
Fin Pitch	2.5 mm
Louvre Pitch	1.14 mm
Fin length	8.59 mm
Tube height	2.5 mm
Tube depth	21.58 mm
Tube thickness	0.32 mm
Louvre length	6.74 mm
Fin thickness	0.1 mm
Louvre height	0.32 mm
Louvre angle	28°

Table 10 Geometrical parameters of a typical radiator for FCE vehicle application

The model solves the following equation:

$$\rho c_w \frac{dT_{rad,out}}{dt} = \dot{m}_w c_w \left(T_{w,in} - T_{w,out}\right) - UA\Delta T_{ml}$$

Where UA is the overall heat transfer coefficient and ΔT_{ml} is the mean logarithmic temperature difference. Temperature increase on the air side has been neglected in this work, and air is assumed to be at constant temperature, equal to ambient temperature.

To evaluate the overall heat transfer coefficient, the model takes $\dot{m}_w$ and u_{air} as inputs.

By assuming that the flow in each coolant tube is the same, the coolant mass flow rate in each channel and Reynolds number are evaluated as:

$$\dot{m}_{w,tube} = \frac{\dot{m}_w}{n_{tubes}}$$

$$Re_w = \frac{\dot{m}_{w,tube} d_{h,tube}}{A_{CSA}\mu_w}$$

Where n_{tubes} , $d_{h,tube}$, A_{CSA} are respectively the number of parallel cooling tubes, the hydraulic diameter and the cross-section area.

Nusselt number is found by using the Gnieliski equation[40], then the heat transfer convective coefficient is determined as:

$$h_w = \frac{Nuk_w}{d_{h,tube}}$$

The air side convective heat transfer coefficient is calculated by using an empirical correlation for louvered fins suggested by Chang and Wang[43] :

$$j = Re_{Pl}^{-0.49} \left(\frac{\theta}{90}\right)^{0.27} \left(\frac{P_f}{P_l}\right)^{-0.14} \left(\frac{L_f}{P_l}\right)^{0.29} \left(\frac{D_t}{P_l}\right)^{-0.23} \left(\frac{L_l}{P_l}\right)^{0.68} \left(\frac{P_t}{P_l}\right)^{-0.28} \left(\frac{t_f}{P_l}\right)^{-0.05}$$

$$h_a = j\rho_a V_a c_{p,a} Pr^{2/3}$$

Where j is Colburn Factor. This correlation is valid for $100 < Re_{Pl} < 3000$.

The overall surface efficiency of the fin is defined as:

$$\eta_o = 1 - \frac{A_f}{A_o}\left(1 - \eta_f\right)$$

By assuming that the temperature differences between the tubes are negligible, the fin can be considered as insulated at the center. Thus, the fin efficiency is calculated as:

$$\eta_f = \frac{\tanh(mL_f/2)}{\frac{mL_f}{2}}$$

Where

$$m = \sqrt{\frac{h_a P_f}{k_f A_{CRS,f}}}$$

Finally, the overall heat transfer coefficient is calculated as:

$$UA = \left(\frac{1}{h_w A_t} + \frac{t_t}{k_t A_t} + \frac{1}{\eta_o h_a A_o}\right)^{-1}$$

Radiator has been sized to meet the Power disposal required at the nominal conditions of the operation of the system.

3.9 Vehicle air flow and fan model

The air vehicle air flow and fan model are used to evaluate the velocity of the air flowing across the radiator, which affects the heat transfer between the air and the liquid water flowing through the radiator tubes. The air velocity is not the same as the speed of the vehicle because of the restrictions to flow of the under-bonnet geometry and the possible presence of a fan. The approach proposed by [16] has been used. A typical passenger vehicle with a fully fan shrouded radiator has been modelled in this thesis. 8 different sections have been considered, such as (1) ram air, (2) radiator grille, (3) expansion behind grille, (4) contraction before fan, (5) radiator fan, (6) expansion after fan, (7) radiator, (8) air exit.

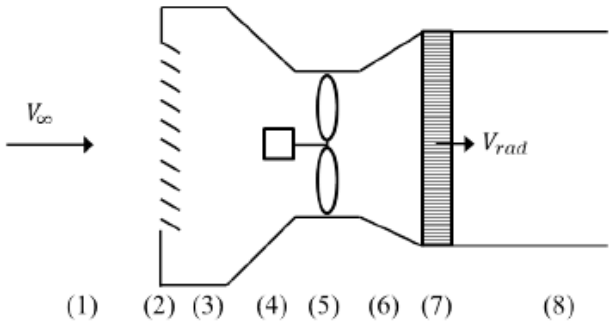

Figure 33 vehicle air model scheme

Following the approach presented by [16], a pressure coefficients method has been used. The pressure drops occurring at each section can be expressed as:

$$\Delta P_i = \frac{1}{2}\rho k_{p,i} V_i^2$$

Where $k_{p,i}$ and V_i are the pressure coefficient and the velocity in the section i, respectively. The internal flow pressure loss is given by the sum of the eight contributes:

$$\Delta P_{int} = \frac{1}{2}\rho \sum_{i=1}^{8} k_{p,i} V_i^2$$

Since no air is leaving the system, the volumetric air flow rate is constant along the sections; in this way it possible to express the air velocity in the section i symply as:

$$V_i = V_{rad}\frac{A_{rad}}{A_i}$$

Thus, the internal flow pressure loss can be evaluated as:

$$\Delta P_{int} = \frac{1}{2}\rho (V_{rad}A_{rad})^2 \sum_{i=1}^{8} \frac{k_{p,i}}{A_i^2}$$

The overall pressure loss is reduced by the presence of a fan, that increases the air flow rate across the radiator. The pressure increase of the fan is expressed using the empirical method of [16], who suggests the following relation:

$$\Delta P_{fan} = c_1 (V_{rad}A_{rad})^2 + c_2 (V_{rad}A_{rad}) \left(\frac{N_{fan}}{2100}\right) + c_3 \left(\frac{N_{fan}}{2100}\right)^2$$

Where N_{fan} is the fan speed and c_1, c_2 and c_3 are experimental constants. The total pressure loss of the system can be evaluated by means of the following equation. ΔP_{fan} is negative since it represents an increase of pressure and not a loss.

$$\Delta P_{tot} = \Delta P_{int} - \Delta P_{fan}$$

Where ΔP_{tot} can be expressed as a function of the vehicle speed V_∞, always using the pressure coefficients method:

$$\Delta P_{tot} = \frac{1}{2}\rho k_{p,t} V_\infty^2$$

Once the fan speed N_{fan} has been fixed, the only unknown term is the air radiator velocity, that can be easily obtained. The pressure coefficients and the cross-sectional area values used in this model are reported in Table 11:

Location	$k_{p,i}$	**Cross sectional area** A_i $[m^2]$
Ram air (1)	1.0	0.5
Grille (2)	2.0	0.5
Expansion behind grille (3)	1.0	0.5
Contraction for fan (4)	0.2	0.13
Radiator fan (5)	-	-
Expansion after fan (6)	1.0	0.13
Radiator (7)	4.0	Defined from the radiator geometry
Air exit (8)	1.0	1.5
Whole system (relative to V_∞)	0.2	-

Table 11 fan speed model geometric parameters

Chapter 4. Model results

The aim of this chapter is to present the main dynamic phenomena involved in the cell, by means of galvanostatic simulations.

- First, 1D model, at high anode/cathode stoichiometry, has been investigated. A base case has been studied, showing the behaviour of the principal parameters that characterize the cell, such as the oxygen CCL activity, the medium water content and the water fluxes crossing the membrane.
- Then, the influence of the geometry in the cell operation and dynamic has been analysed, without the influence of the channel, since the analysis has been performed at very high stoichiometry. The variation of both cathode GDL and membrane thickness has been commented, focusing on the oxygen and water dynamics.
- Then the case with low stoichiometry (1D+1D model), typical of the automotive sector, has been studied, showing how the channel transient effect influences the main quantities describing the cell operation. Moreover, some simulations with different values of inlet cathode RH and temperature have been performed, in order to evaluate the influence of the external conditions on the cell operation, mainly in the water management. The fitted functions for the ORR cathode kinetic constant K_r, oxygen GDL diffusivity $D_{O2,gdl}$, membrane conductivity σ and ORR transfer coefficient α_{ORR} presented in the chapter 2 have been adopted.

The input current load implied for the simulations presents the following profile, reported in Figure 34:

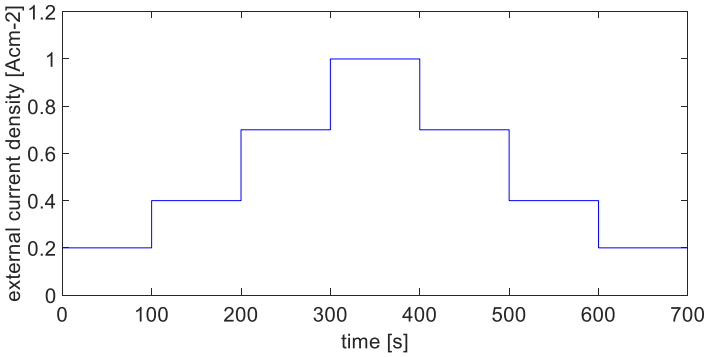

Figure 34 external current density cycle

4.1 1D cell model

This paragraph has been divided in 3 sections:

- In the first section, a static analysis has been performed, with the aim to study the effect of change in current density to the main parameters. Since no hysteresis phenomenon is predicted in this work, the attention has been focused just on the first part of the cycle, from 0 to 400 seconds.
- In the second section, a dynamic analysis is conducted, focusing on the dynamic behaviour of the principal parameters involved in the water management, when a step change in current density occurs.
- In the third section, a sensitivity analysis is performed, showing how the GDL and membrane thickness variation influence the oxygen and water dynamics respectively.

All the simulations have been performed under the assumptions reported in Table 12:

Parameter	value
T_{cell}	80 $°C$
P_{cell}	2 bar
$RH_{in,cath}$	30 %
membrane thickness	10 μm
GDL thickness	200 μm

Table 12 Assumptions used for 1D model analysis

The model is run at very high stoichiometry, so it is reasonable to state that the evolution of all the quantities considered is negligible along the channel length: the attention has been focused just on a block, representative for the whole channel: the channel 3 has been chosen for this analysis.

4.1.1 1D cell model static analysis

The following profiles are reported and commented later:

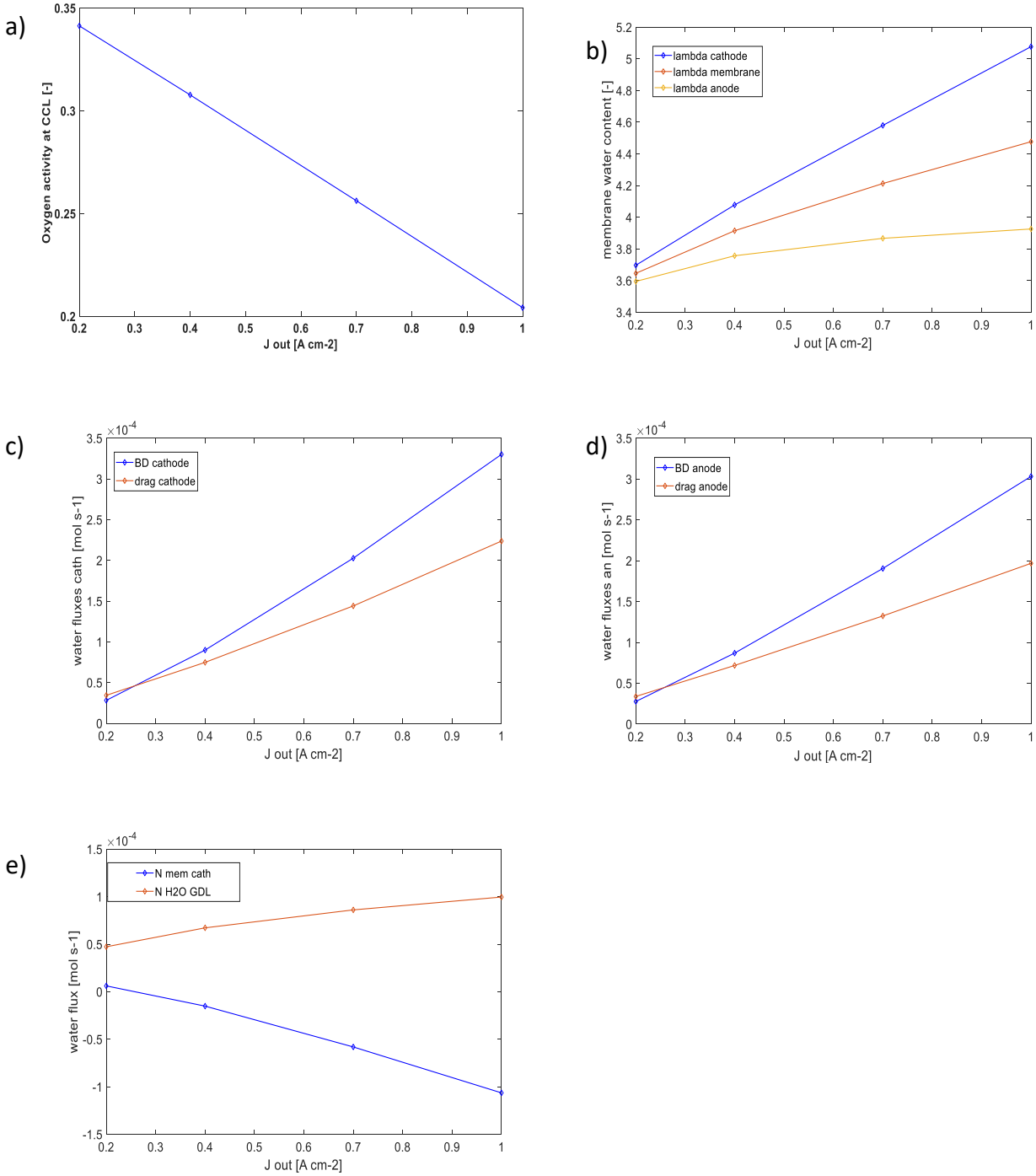

Figure 35 Effect of increasing current on oxygen activity, membrane water content and water transfer across the membrane at operating conditions of Table 13

In Figure 35.a, the CCL oxygen activity is reported: as it is expected, $a_{O_2,CL}$ decreases increasing the current density and vice-versa, since more oxygen is required by the ORR at high currents to occur. In Figure 35.b, the profiles of λ_m, λ_{cath} and λ_{an} are presented. It can be noticed that for each current the following relation is satisfied:

$$\lambda_{cath} > \lambda_m > \lambda_{an}$$

This means that the water concentration gradient is directed from cathode to anode, which is responsible for the back-diffusion transport mechanism. The relative difference between these values becomes more relevant when the current increases, so the 1D model suggests that the back-diffusion fluxes are favoured at high currents.

In Figure 35.c and Figure 35.d the difference between the drag and back diffusion fluxes, at cathode and anode side respectively, are shown, while in Figure 35.e, a comparison between $\dot{N}_{memb,an}$, $\dot{N}_{memb,cath}$ and $\dot{N}_{H2O,GDL}$ is performed. It can be observed that:

- Both drag and back diffusion fluxes increase with the current density. The first one is directly dependent on J_{out}, while the second one is related to the water vapor concentration gradient through the membrane, which is enhanced at high currents, as previously explained in Figure 35.b
- Back diffusion is globally the dominant mechanism, except at 0.2 Acm-2. At this range the drag flux is higher despite the low current, due to the decreased water concentration gradient. According to the chosen convention, $\dot{N}_{memb,an}$ and $\dot{N}_{memb,cath}$ are positive where the drag is predominant: the net water flux in membrane flows in the cathode-anode direction when j is higher than the threshold of 2 Acm-2.
- $\dot{N}_{H2O,GDL}$ is positive and increases with the current density, even if $\dot{N}_{memb,cath}$ shows the opposite trend. This indicates that the amount of water produced at the CCL is higher than the one flowing towards the anode side; this is the reason why λ_{cath} increases with the current density more than λ_{an}, making the back diffusion the dominant water transport mechanism in almost all the current ranges.

4.1.2 1D model dynamic analysis

To better understand how the water dynamic works in the 1D model, the attention has been focused on the step change in current density from 0.4 to 0.7 Acm-2. The aim of this analysis is to study how the main parameters involved in the fuel cell water management description behave when an instantaneous variation in current occurs. All the simulations have been performed under the assumptions reported in Table 12.

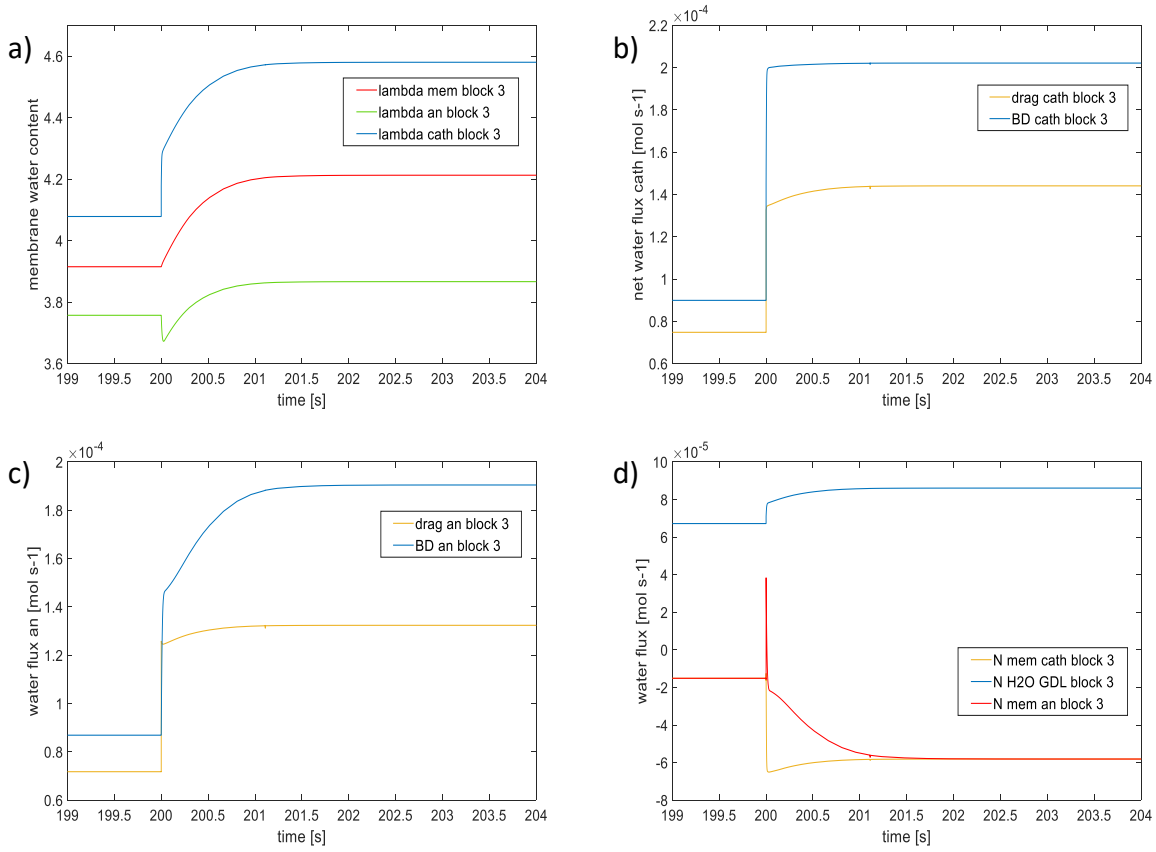

Figure 36 Dynamic effect of current step increase on membrane water concentration and water fluxes across membrane at operating conditions of Table 12;

It can be noticed that increasing the current density, $\dot{N}_{drag,an}$ instantaneously increases, being directly dependent on J_{out}, and so λ_{an} decreases. At the same time even $\dot{N}_{drag,cath}$ immediately arises, as well as the water produced at the cathode side, so even λ_{cath} instantaneously increases, more than λ_{an} thanks to the water production term, as explained in [44]. Water vapor concentration gradient immediately rises, leading to an increase of the back-diffusion fluxes. The global growth of all the water fluxes involved can be observed in the Figure 36.b and Figure 36.c, where it is also possible to notice that the cathode back-diffusion flux experiences a more consistent rise than the anode one when the current change, and that the λ_{cath} relative growth is more relevant than the λ_{an}.

Since $\dot{N}_{drag,an}$ and $\dot{N}_{drag,cath}$ grows immediately after the step change are very similar (the drag coefficient are slightly different, but this variance is not so relevant), $\dot{N}_{mem,an}$ will be higher than $\dot{N}_{mem,cath}$ just after the step change, leading to a dis-equilibrium in the membrane water management, as can be observed in Figure 36.d. So, λ_m tends to increase, as shown in Figure 36.a. As an effect of drag flux, even λ_{cath} increases, as shown in Figure 36.c. At the anode side, the back-diffusion mechanism is the predominant, so water tends to

reach the anode channel, leading to an increase of λ_{an}. It can be noticed that before and after the step change in current density $\dot{N}_{mem,an}$ is negative, indicating that the back-diffusion is the dominant transport mechanism, while, precisely when the current variation occurs, $\dot{N}_{mem,an}$ becomes positive thanks to the instantaneous increase of $\dot{N}_{drag,an}$. Two different time scales be recognized:

- The first is due to the instantaneous variation of the current;
- The second one is due to the water dynamics in the membrane;

4.1.3 GDL thickness variation

The following figures represent the different behaviour of the $a_{O_2,CL}$ varying the GDL thickness, from 200 μm to 300 μm. The membrane thickness is kept equal to 10 μm. The other operating parameters are reported in Table 12. The graphs show the $a_{O_2,CL}$ and the voltage profile near 200 seconds, just after the step change in current from 0.4 to 0.7 Acm-2, so to better understand the difference in the transients:

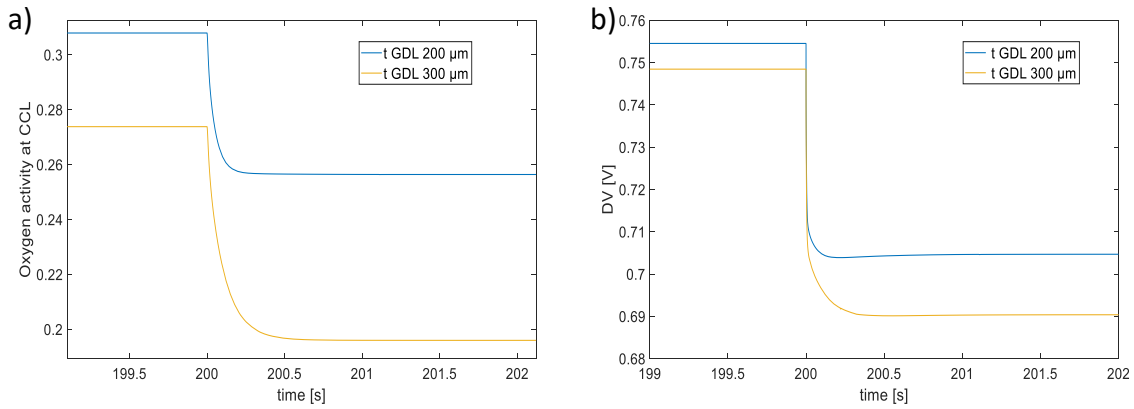

Figure 37 Effect of GDL thickness variation on oxygen activity at CCL and cell voltage at op. conditions Table 12

It possible to notice in Figure 37.a that, increasing the GDL thickness, $a_{O_2,CL}$ globally decreases, as shown even in [45]: this is a consequence of the increased oxygen transport resistance, which linearly depends on GDL thickness. The difference between the two profiles becomes more relevant at high current density. It can be noticed that the oxygen dynamic is faster for thinner thickness, because of the reduced mass capacity, which is linearly dependent on δ_{gdl}. Globally the model predicts a time-scale for the oxygen dynamics about 0.01-0.05 seconds, as confirmed by [46]. Figure 37.b shows the variation in the cell potential, where the influence of the O2 dynamics is clear: the voltage is higher for

thinner GDL thickness, while the transient is faster, because of the better oxygen diffusion process.

4.1.4 Membrane thickness variation

The second case study has been performed with the aim of investigating the water transport across the cell, varying the membrane thickness from 10 μm to 30 μm, and its effect on the cell potential. The GDL thickness is maintained equal to 200 μm. The following graphs represent the profile of the medium water content and the cell voltage increasing the membrane thickness, after the step change in current density from 1 to 0.7 Acm-2, so to better notice the difference among the transients.

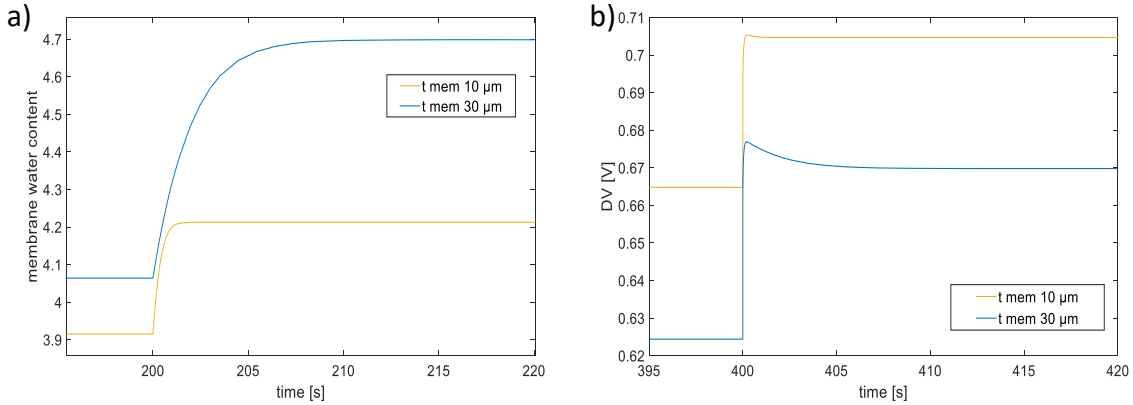

Figure 38 effect of membrane thickness on membrane water content and cell voltage

Observing the two figures it is possible to notice that:

- Increasing t_m the value of the water content globally increases, showing that a thinner membrane tends to be less hydrated than a larger one, since the water fluxes passing throughout it will be higher. The λ_m dynamic is slower for larger membrane, since the mass capacity increases with t_m, with a time scale between 1-10 seconds, as observed in literature.
- The voltage is lower for larger membranes, because of the ohmic losses through the electrolyte [47]. The transient is slower in the case of membrane thickness equal to 30 μm, presenting an initial overshoot, which decreases with time until the potential reaches its stationary value.

4.2 2D cell model

This paragraph has been divided in 2 sections:

- The first one is a static analysis, which aims to give a general description on how the considered parameters vary along the whole input current cycle, focusing on their variation along the channel length. Looking at the membrane water content evolution along the channel, increasing the current density, the presence of a water recirculation across the cell is suggested.
- In the second section a local dynamic analysis is conducted about the influence of the channel dynamics on oxygen and water transport, when a step change in current density occurs.

4.2.1 2D cell model static analysis

Feeding the cell with low stoichiometry, typical of the automotive sector, the channel effects are no longer negligible. In this way the model shows a 2D evolution, both along the through plane direction and along the channel length. The aim of this section is to study how the channel effects influence the cell operation. The follow parameters have been used:

Parameter	**value**
T_{cell}	80 $°C$
P_{cell}	2 bar
$RH_{in,cath}$	30 %
membrane thickness	10 μm
GDL thickness	200 μm
λcath/λan	1.5/1.2

Table 14: 2D model operating parameters

Channel effect is expected to affect all the phenomena occurring within the cell, such as the currents produced by each block, the water fluxes across the membrane and the anode/cathode RH values. Globally the difference of these variables along the channel length becomes more evident, as it is expected to happen in a 2D model. In the following figures some relevant profiles are presented and later commented, focusing mainly on the water fluxes and their directions.

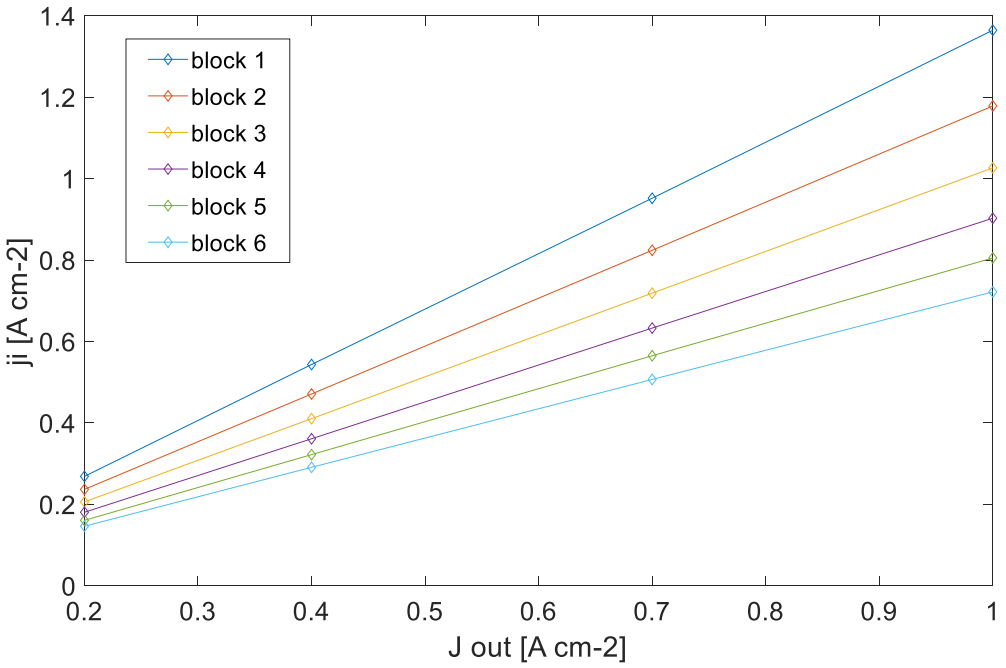

Figure 39 Current density profile along channel layers with increasing external currents

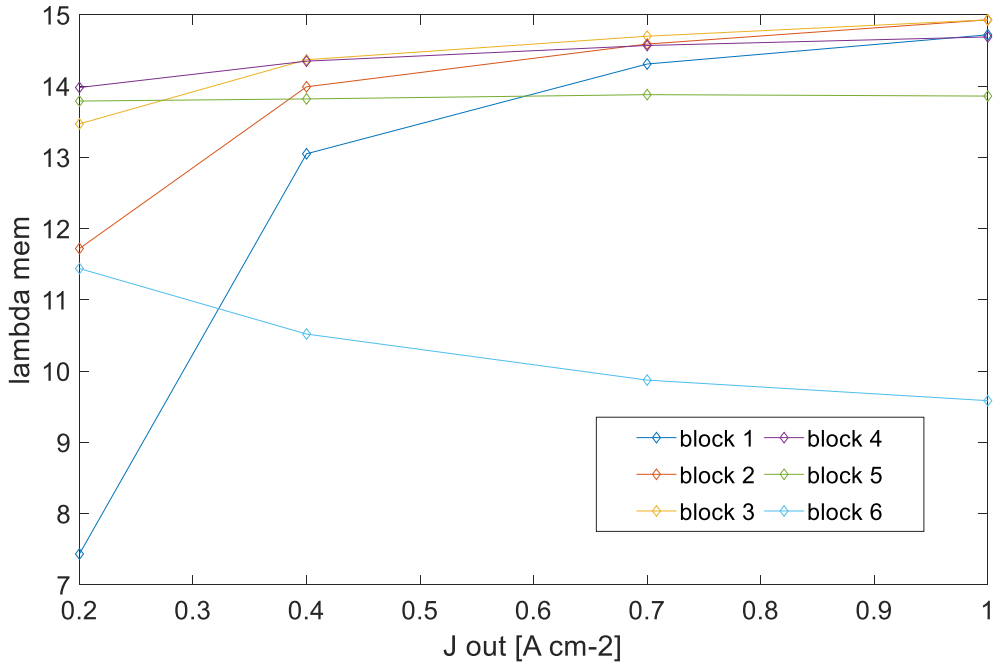

Figure 40 membrane water content profile along channel layers with increasing external current density

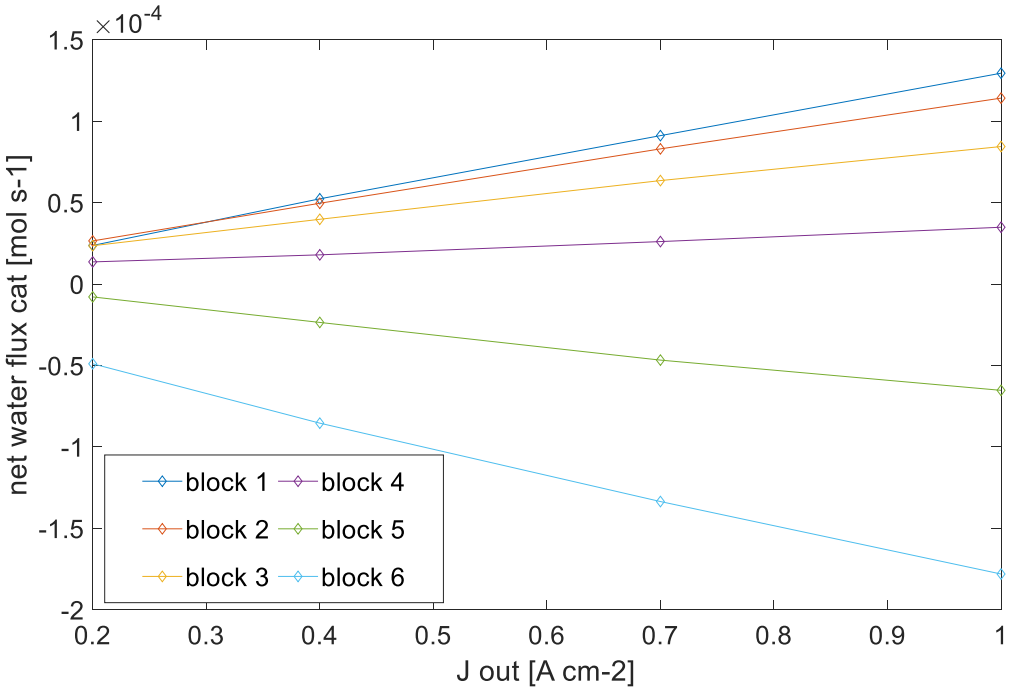

Figure 41 net water fluxes from membrane to cathode with increasing external current density

In Figure 39 the profile of the current density produced by each block is presented. Given these operating conditions, reported in Table 14, it can be noticed that, for each J_{out} externally imposed, the current density produced by each block is lower than the previous one. The variance between the current density produced is higher at high currents, where the channel effects become more relevant: between 300 and 400 seconds, where the cell is asked to produce 1 Acm-2, the first block generates approximately 1.4 Acm-2 (about 40% more than the average) while the last one 0.7 Acm-2.

In Figure 40, the membrane medium water content profile is shown, while in Figure 3, water flow rate transferred across membrane is reported. Globally it can be seen that the water content rises globally as the current density increases, except for the cathode outlet blocks (5 and 6), corresponding to the anode inlet, that present a decreasing water content with current, as observed in [5]. This suggests that there is a sort of water recirculation in the cell, as demonstrated in Figure 41: the anode inlet tends to become dryer, when the other channel blocks tend to become more wet. This behaviour is more evident at high currents, when the water transfer rises.

It can be noticed that the central zone of the cell (block 4 at low currents and block 3 at high current) is the more hydrated, as it expected to happen in a counter-flow logic. At the same

time, these blocks are the ones experiencing the lowest water content change since water concentration gradients are very low.

The anode inlet (channel 6) presents a value of λ_m higher than the cathode inlet, because of higher RH at anode side with respect to cathode side. Moreover, at low current, water quantity moving through membrane is not so relevant. Successively, as the current increases, water content of anode inlet block decreases, until it becomes the dryer one.

Moreover, because of the first current step, the membrane water content of the first channel block takes more time with respect to the others, since its variation is larger, and more water is accumulated. The same occurs at low current region, since membrane needs to desorb a lot of water.

Focusing on Figure 41, it can be noticed that:

- $\dot{N}_{memb,cath}$ is positive in the blocks 1, 2, 3, 4. This indicates that the net water flux is directed from the anode side to the cathode one; so, the drag transport is dominant, and this is due to the high currents experienced in these blocks. Increasing the current density more water is produced at the CCL, and so a higher quantity of water is circulating in the cell.
- $\dot{N}_{memb,cath}$ is negative in the blocks 5 and 6. This suggests that the principal water transport mechanism is the back diffusion, and so the net water flux is directed from the cathode to the anode side. This is the effect of the lower currents produced in the final blocks, since the lower oxygen concentration at CCL, combined with the water transport along the channel, ensures high water concentration in the final blocks at cathode side, beneficial for the back-diffusion mechanism.

Figure 42 and Figure 43 presented below, shows the behaviour of $\dot{N}_{H2O,GDL}$, the sum between $\dot{N}_{memb,cath}$ and the water produced at the CCL, and of the outlet cathode RH along the channel length.

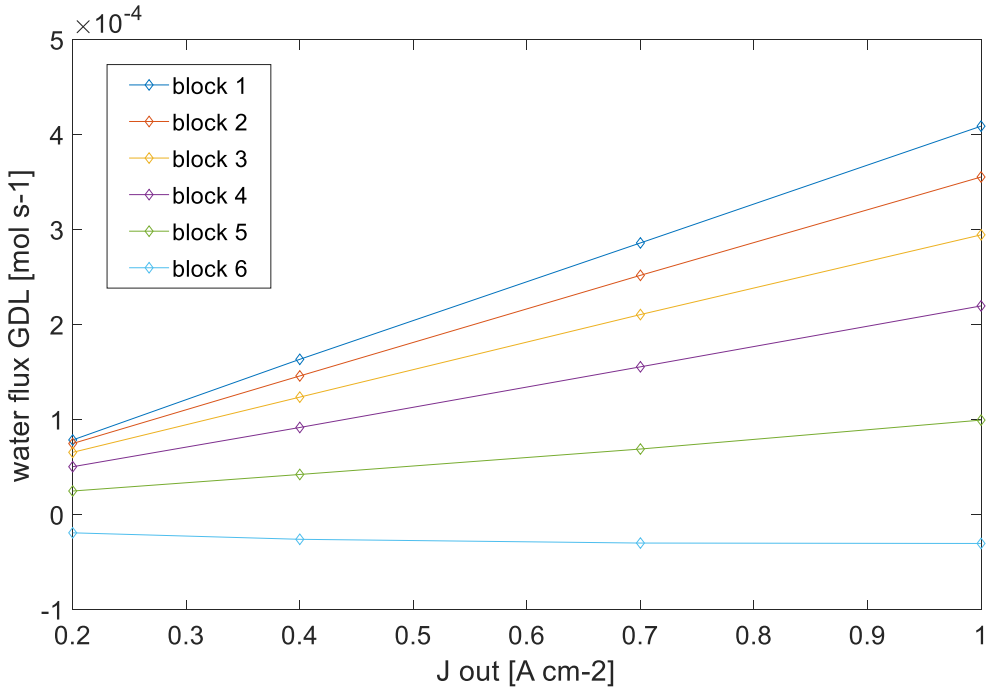

Figure 42 water flux profile across channel layers with increasing external current density

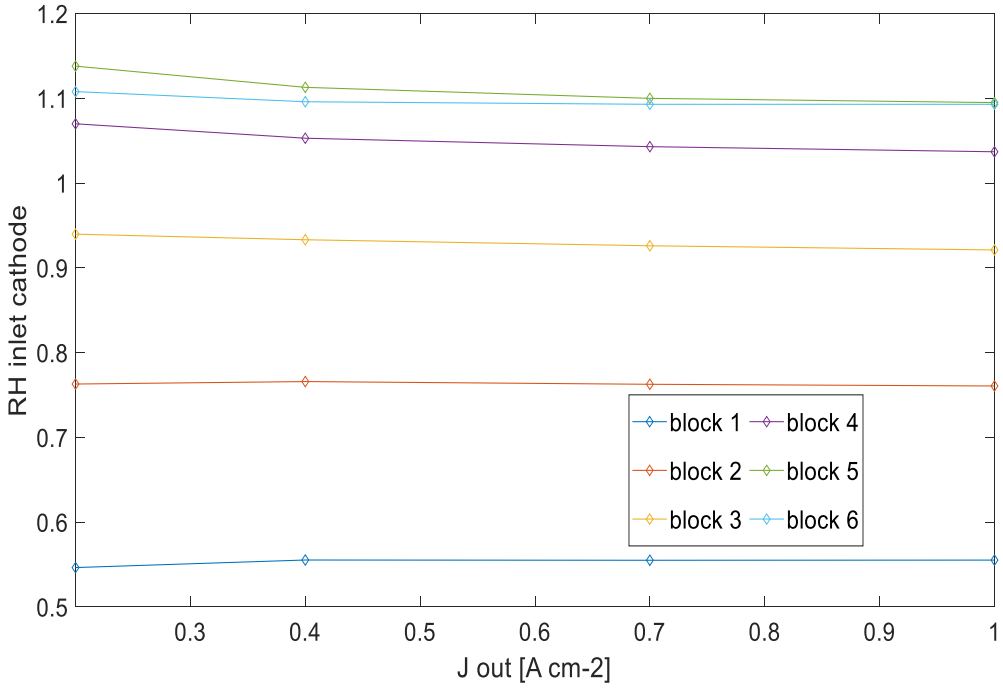

Figure 43 RH profile across channel layers with increasing current density

As it can be noticed, all blocks experience an increase of $\dot{N}_{H2O,GDL}$ when the current density arises, except for the block 6, where the water flux directed to the cathode GDL slightly decreases; moreover, it is negative for the whole range of current densities simulated. This means that $\dot{N}_{memb,cath}$, which is negative in the final block (anode inlet) since the back diffusion in dominant, prevails the water generation term, leading to a negative value of

$\dot{N}_{H2O,GDL}$. Thus, water is taken from cathode channel and, through membrane, it is transported to the anode side. Cathode RH profile is constantly growing along the channel length, except for the last block. The higher values are reached in the fifth block, both because water is produced at the CCL and because of the water transport along the channel. In the block 6, cathode channel RH is lower, as confirmed by the negative GDL-water-flux trend. The increase of relative humidity, combined with the low currents produced in the last blocks, are beneficial for the back- diffusion mechanism, that is the dominant one in the final blocks.

Effect of cathode inlet relative humidity

The influence of different external condition has been investigated. The aim of this study is to perform a static analysis, observing the variation of the main magnitudes characterizing the fuel cell operation when the inlet cathode RH is turned to 50% and then 70%. The cell parameters are kept constant, while the other operating conditions are (Table 15):

Parameter	**value**
T_{cell}	80 $°C$
P_{cell}	2 bar
$RH_{in,cath}$	$variable$
membrane thickness	10 μm
GDL thickness	200 μm
λcath/λan	1.5/1.2

Table 15 Influence of cathode inlet RH analysis operating parameters

The variation in the oxygen activity at the CCL, in the medium water content and in the water fluxes involved, with different inlet cathode RH values, is presented and commented. To make the figures clearer, just the evolution on the blocks 1, 3 and 6 has been analysed.

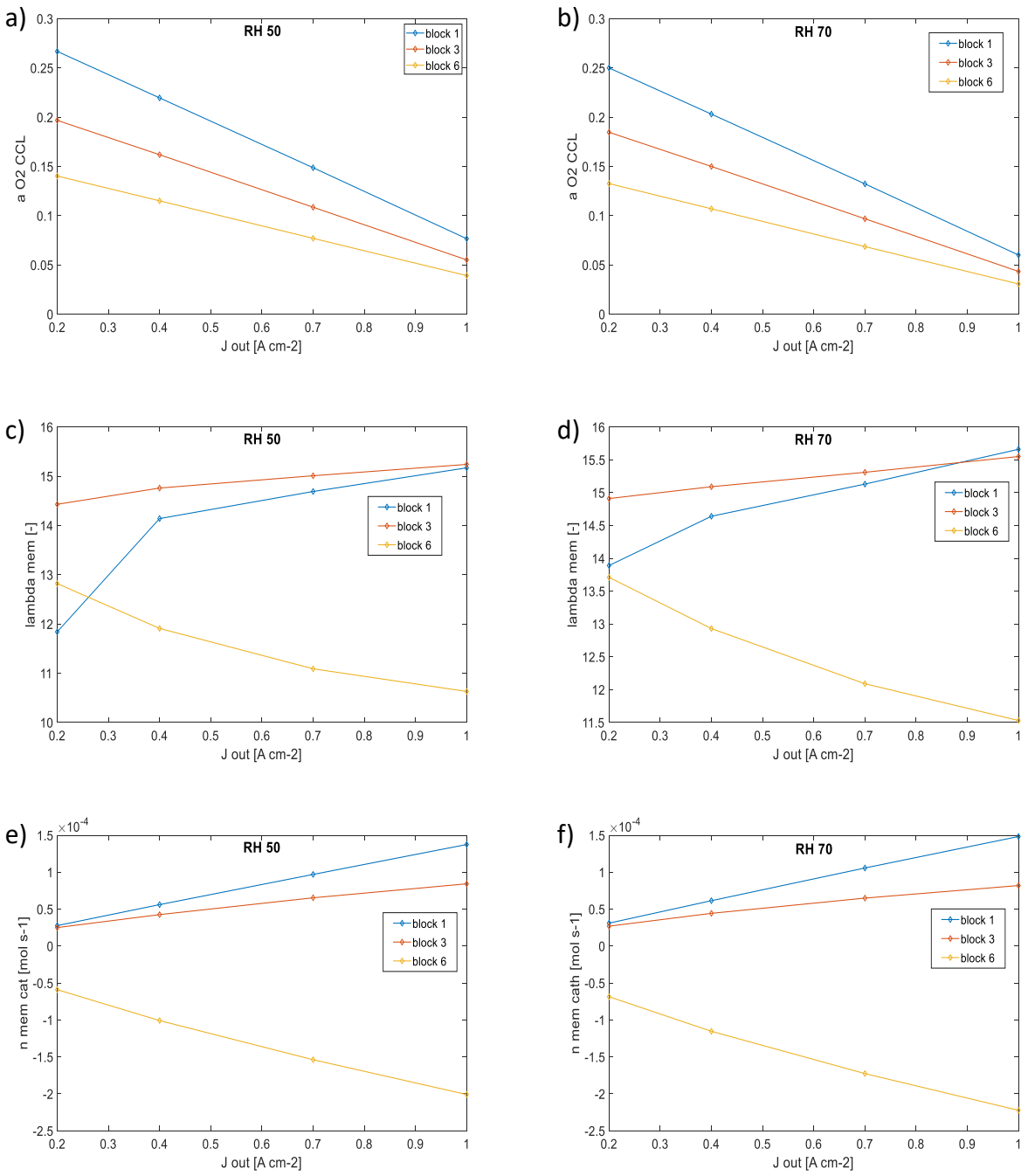

Figure 44 Effect of inlet cathode RH on oxygen concentration on CCL, water content in the membrane and membrane water flux at the operating conditions reported in Table 15

As it can be observed in Figure 44.a and Figure 44.b, increasing the inlet cathode RH, the oxygen activity at the CCL tends to reduce; this trend is valid per each current density of the input cycle. This behaviour is due to the oxygen GDL diffusivity function, obtained in by fitting process in the proper chapter: $D_{O2,gdl}$ deceases increasing the medium RH in the cathode channel, which clearly arises when the air flow entering the cell is more humidified.

Moreover, increasing the inlet cathode RH, the water molar fraction in the channel growths, leading to a decrease in the oxygen partial pressure along the channel.

In Figure 44.c and Figure 44.d, the profiles of the medium water content in membrane, for different inlet cathode RH, is shown. As it can be observed λ_m of each block is higher in the case at RH = 70 %, with respect to the case at RH = 50 %; is interesting to notice that the greatest λ_m variation occurs in the first block at low current, since it is the block directly in contact with the inlet air flow. The trend of λ_m along the channel length is the same as presented in the case with inlet cathode RH = 30 %; in the blocks from 1 to 4 the drag fluxes are predominant, while in the blocks 5 and 6 the back diffusion in the prevailing water transport mechanism. The global increase of λ_m suggests that the membrane is more humidified, since all the water fluxes involved in the cell tend to be more relevant, as can be observed looking to Figure 44.e and Figure 44.f, where it can be noticed that the net water flux at the cathode side increases when the inlet cathode RH gets higher.

Effect of stack temperature

The influence of the cell temperature is now investigated. The case at $T_{cell} = 60\ °C$ is presented and compared with the base case at $T_{cell} = 80\ °C$. The other assumptions are:

Parameter	**value**
T_{cell}	$variable$
P_{cell}	$2\ bar$
$RH_{in,cath}$	30%
membrane thickness	$10\ \mu m$
GDL thickness	$200\ \mu m$
λcath/λan	1.5/1.2

Figure 45 Influence of cell temperature analysis operating parameters

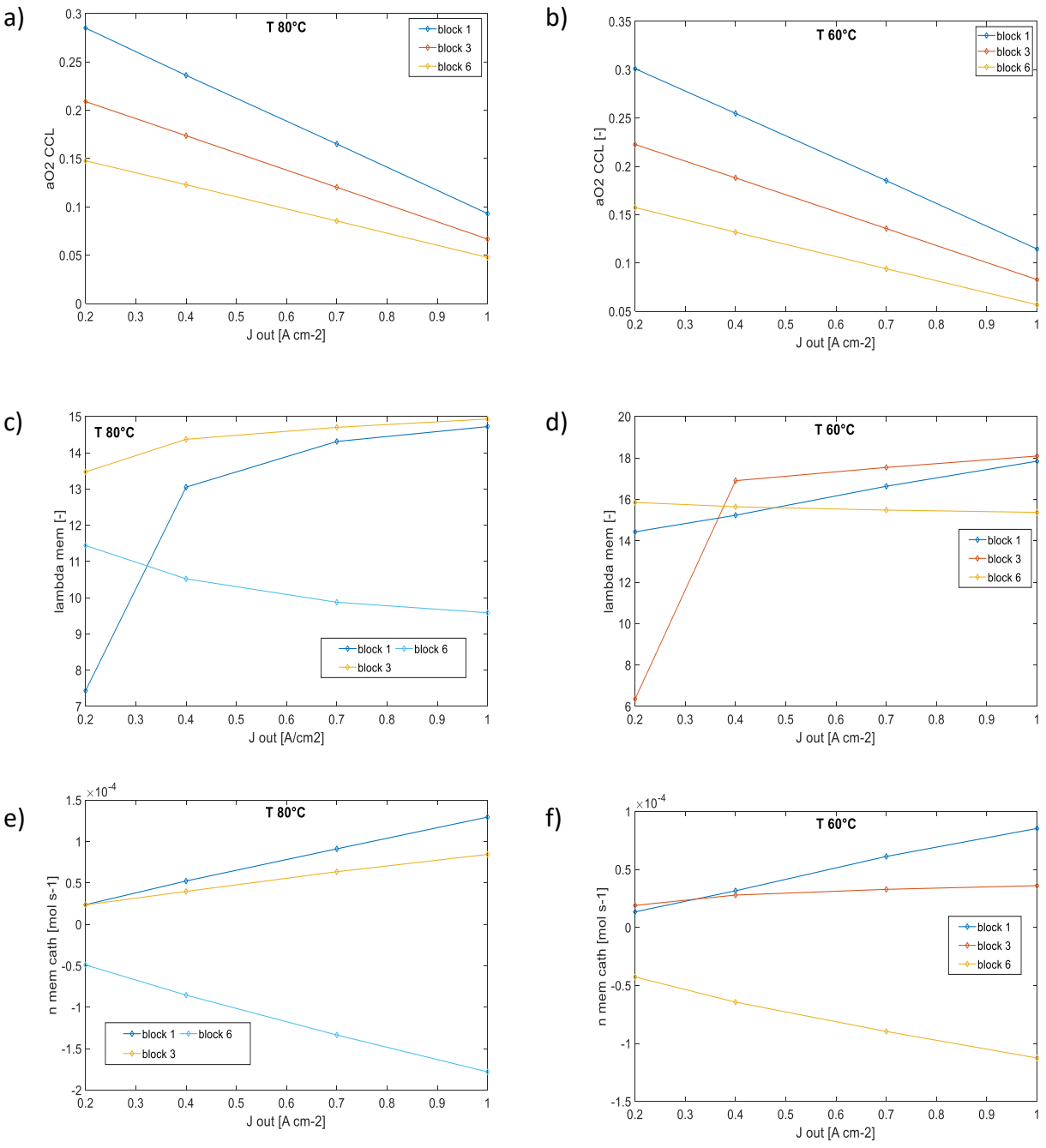

Figure 46 Effect of operating temperature on O2 activity at CCL, membrane water content and membrane water fluxes at operating conditions of Table 15

The graphs above show the behaviour of the oxygen activity at CCL, of the medium water content and of the net cathode water flux in membrane, both at $T_{cell} = 80\ °C$ and $T_{cell} = 60\ °C$. As in the inlet cathode RH variation analysis, just the blocks 1, 3 and 6 have been considered.

It can be noticed that decreasing the cell temperature:

- For all the currents simulated, and for all blocks considered in this analysis, $a_{O_2,CL}$ increases (Figure 46.a and Figure 46.b); this because the lower cell temperature means lower saturation pressure and so, with a fixed value of inlet cathode RH, a lower inlet water partial pressure in the cathode channel. So, the inlet oxygen partial pressure is higher, leading to an increase of $a_{O_2,CL}$.
- Globally λ_m are higher, as Figure 46.c and Figure 46.d show, since the saturation pressure is lower, and so $\lambda_{cath}$and λ_{an} will be higher, leading to a general improve of the membrane medium water content.
- $\dot{N}_{mem,cath}$, in absolute value, is lower. This means that the drag fluxes at the block 1, as well as the back-diffusion ones at block 6, are less relevant; this means that globally the water fluxes circulating in the cell are lower. This can the result of the lower inlet water partial pressure, both at the anode and at the cathode side. (Figure 46.d and Figure 46.e)

4.2.2 2D cell model dynamic analysis

To better understand how the channel effect influences the dynamics of the main magnitudes involved in the fuel cell description, the step change from 0.4 to 0.7 Acm-2, near 200 seconds, has been analysed. Operating parameters are reported in Table 16:

Parameter	**value**
T_{cell}	$80\ °C$
P_{cell}	$2\ bar$
$RH_{in,cath}$	30%
membrane thickness	$10\ \mu m$
GDL thickness	$200\ \mu m$
λcath/λan	1.5/1.2

Table 16 2D cell model dynamic analysis operating parameters

The profiles across the channel length of the membrane water content and of the oxygen activity at the CCL are presented and commented below.

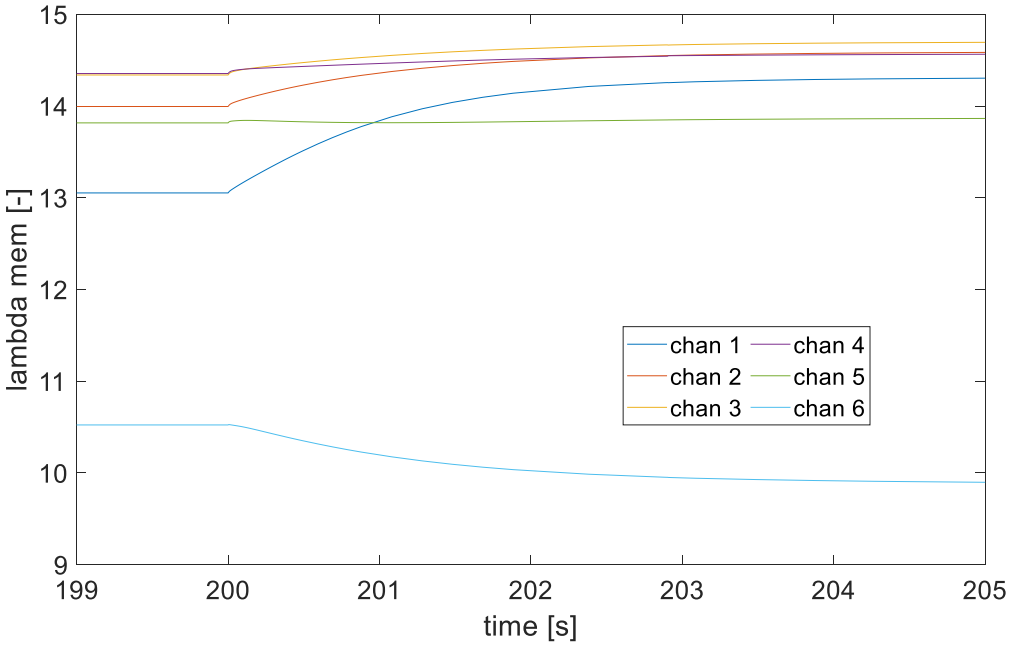

Figure 47: membrane water content profile at low stoichiometries

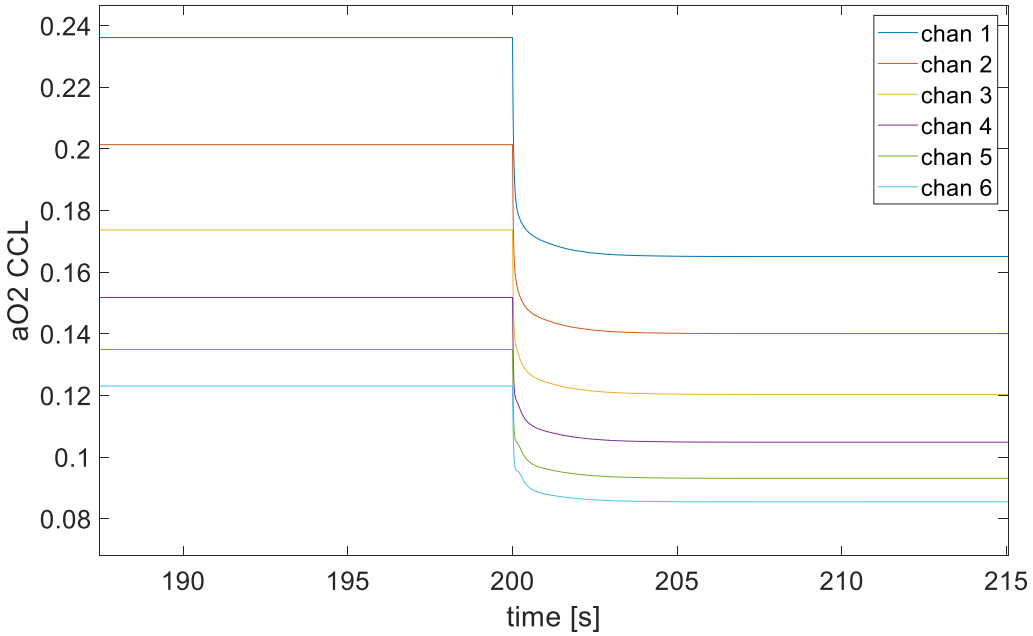

Figure 48 oxygen activity in the CCL profile at low stoichiometry

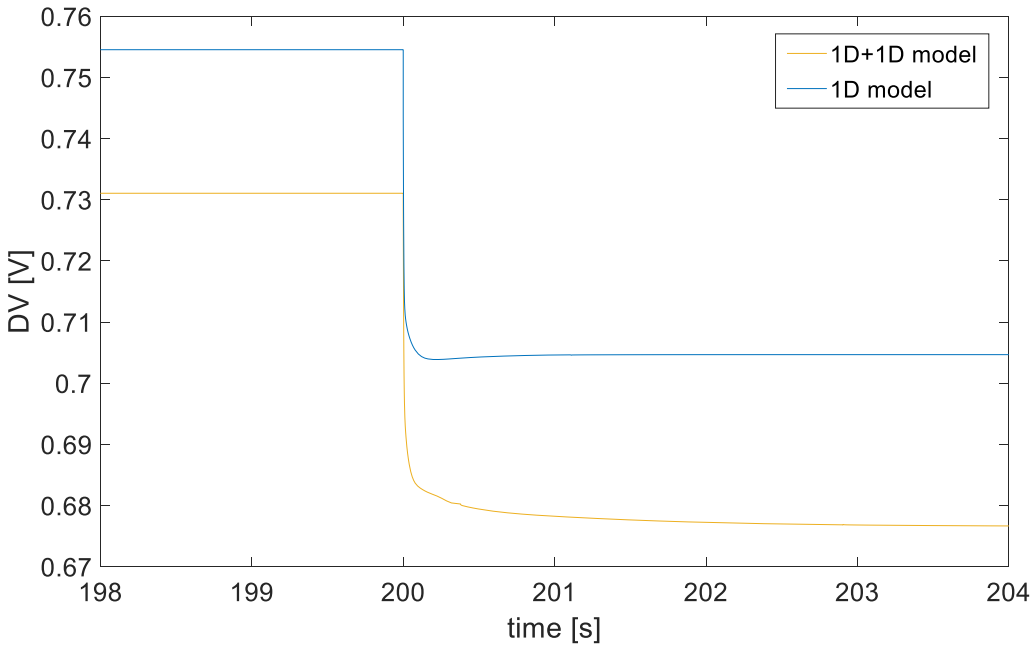

Figure 49 comparison of voltage dynamics at low and high stoichiometry

It can be noticed that:

- λ_m dynamics varies along the channel length, as it influenced by the water transport along the channels. Figure 47 shows that in the block 1 and 6 the water fluxes involved are more relevant than in the central blocks, leading to a greater variation of λ_m, that results in a slower dynamic. As it has been previously shown, since the high currents involved, the block 1 requires a great quantity of water, provided by the anode that gets dryer; for this reason, the λ_m slope in the block 1 is positive, while in the block 6 it is negative.
- The $a_{O_2,CL}$ transients are globally longer than the one predicted by the 1D model, because of the influence of the channel dynamic. It can be noticed in Figure 48 that for the last channel blocks, a sharp decrease is visible because of the delay in mass transport. Thus, the time scale of oxygen transport is affected by the dynamics of the preceding channel blocks.
- The channel effect influences even the voltage transient profile, which becomes slower in the 1D+1D case, because of the delay due to the mass transport (Figure 49).

4.3 Humidifier model

The following section is focused on the evaluation of the effect of matching the humidifier model with the FC stack model.

- First, an analysis of the performance of the static humidifier model is presented, which aims to roughly size the component with respect to PEM stack requirements and to understand the effect of the change of the performance of the humidifier with respect to the change of external conditions;
- Second, an analysis of the dynamics of humidifier has been conducted, with the aim to understand the extent of the change of the time scale of the humidifier with respect to the change of external conditions.
- Third, the effect of the dynamics of the humidifier on the performance of the PEM stack has been investigated.

4.3.1 Humidifier static model

The variables affecting the performance of the humidifiers are mainly geometric variables, membrane properties and flow conditions. The change of humidifier geometry contributes to humidifier performance in terms of heat transfer and water transport:

- Cross sectional area of each channel: it affects heat coefficients, the dynamic behaviour of the flow and the flow rate per channel;
- Number of plates and channels: it affects the flow rate per channel;
- Channel length: it determines the usable membrane area and the capacity of the flow and the dynamic behaviour of the flows.

The performance of the humidifier has been estimated by looking at the RH out of the dry side and the water recovery ratio. WRR describes how much water is transferred to the dry outlet compared to the amount of water supplied, which would be the maximum amount of transferrable water:

$$WRR = \frac{\dot{m}_{H_2O\ dry,out} - \dot{m}_{H_2O\ dry,in}}{\dot{m}_{H_2O\ wet,in}}$$

Literature suggests average WRR of 30-40%[22].WRR of the static model has been computed at different conditions in order to understand the extent of the assumptions on the performance of the modelled humidifier and to perform a roughly sizing of the component.

Humidifier performance has been firstly estimated by considering a dPoint Technologies humidifier, consisting of 40 plates and 35 channels per plate. The channels are 3 mm wide and high and 322 mm long, which correspond to a membrane area of 1.35 m^2. [48]

First, all the variables were taken fixed except for the RH in wet and wet flow rate. Fixed values are reported in Table 17

Variable	**Value**
λ_{cath}	1.5
$T_{in,wet}$	80 °C
$T_{in,dry}$	50°C
P_{hum}	2 bar
$\dot{N}_{tot\ in,dry}$	0.57 mol/s [j cell=0.8 Acm-2]

Table 17 Sizing analysis of the humidifier operating parameters

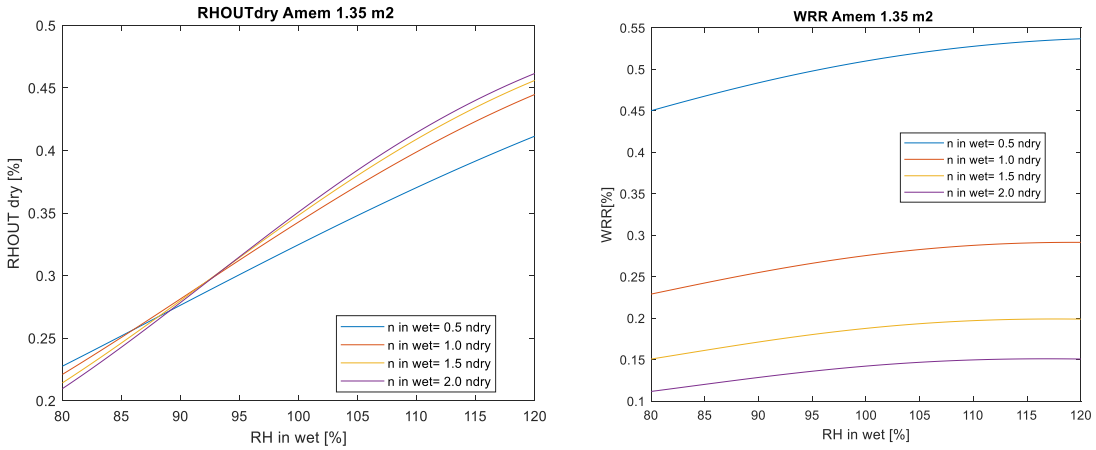

Figure 50 RH out dry side and WRR at low equivalent membrane area humidifier

As it was expected (Figure 50), $RH_{out,dry}$ increases with increasing the flow rate at the wet side and the $RH_{in,wet}$, except for low $RH_{in,wet}$. On the contrary, the WRR is higher at lower wet flow rates as the absolute amount of recoverable water is the lowest one. Moreover, WRR is not increasing linearly, but is seems to reach a maximum. In fact, at very high $RH_{in,wet}$ the term at the denominator increases more than the amount of water at the outlet of the dry side, which results in a decrease of the WRR.

In order to obtain comparable performance of the model with respect to experimental results, it has been decided to increase the membrane area up to 3 m^2. This choice can be explained by considering that:

- membrane humidifiers are usually made by five layers: the Nafion© membrane is sandwiched between two PTFE layers, which give higher strength and a better water diffusivity. In this model only the membrane diffusion has been considered, thus the water diffusion capability through the membrane is worsened with respect to experimental values.
- the presence of the support layer improves water diffusion as it enhances heat transfer. In this model, its effect has been neglected.
- 2D effect linked with the geometry of the channels has not been investigated.

Figure 51 shows how the WRR computed with $A_{mem} = 3\ m^2$ at the same conditions as before improves and reaches the typical conditions found in literature.

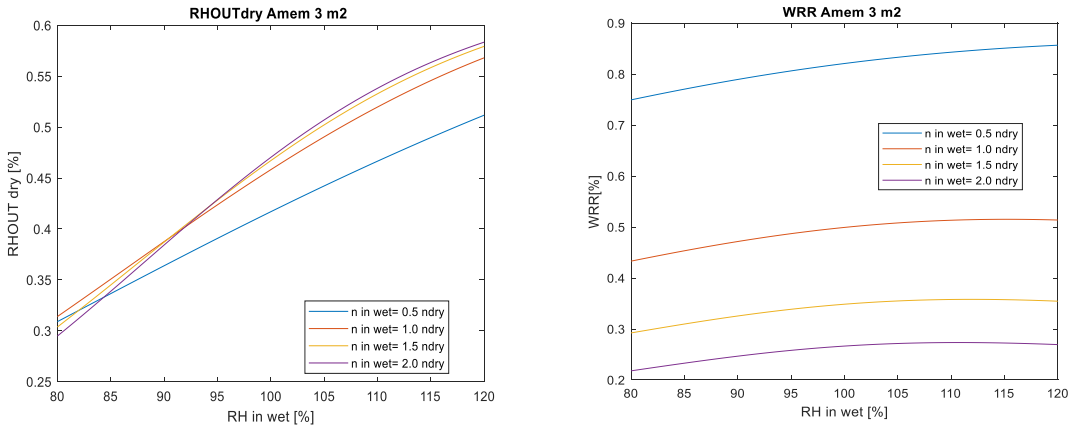

Figure 51 RH out dry side and WRR at equivalent membrane area humidifier

4.3.2 Effect of operating parameters

Several external conditions have been investigated in order to understand which external parameter plays a larger role on water transfer. In particular, the aim of this section is to define whether the difference of temperature between the inlet of the wet and dry side, respectively or the difference of flow rates play a key role on water transfer.

Operating conditions for this study are contained in Table 18

Variable	Value
$T_{in,wet}$	80 °C
$T_{in,dry}$	variable
P_{hum}	2 bar

$RH_{in,wet}$	100%
$RH_{in,dry}$	0%
$\dot{N_{in,wet}}$	$4 \cdot 10^{-4} \frac{mol}{s}$

Table 18 Effect of inlet dry Temperature and flow rates on humidifier operating parameters

Model results are reported below in Figure 52, and trends are validated by comparing the trends with experimental results found in [49].

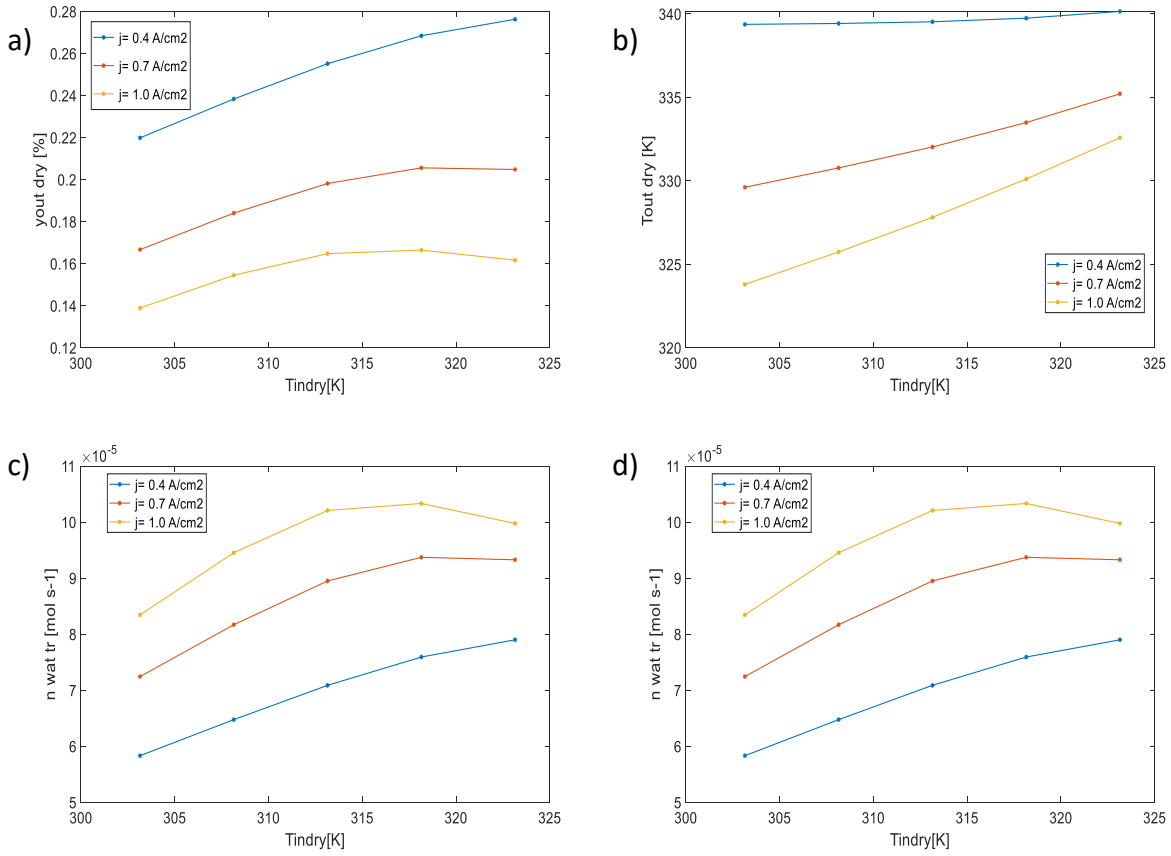

Figure 52 Performance humidifier at different inlet dry air temperature and flow rate

By increasing the molar flow rate at the dry inlet:

- The molar concentration of water at dry side outlet decreases. *Ref* suggests this is due to a decrease in residence time of air in the channel;
- The Temperature at the dry side outlet decreases;
- WRR increases by increasing the flow rate at the dry side both inlet and outlet conditions gets closer in terms of temperature and flow rate. It leads to higher water vapor concentration gradient across membrane which enhances the water transfer through the membrane.

By increasing the $T_{in,dry}$:

- The $T_{out,dry}$ increases because of higher inlet temperature, as it can be expected;
- WRR, as well as the water stream transferred across membrane, tends to reach a maximum which is different per each flow rate condition. The WRR maximum corresponds to the condition in which the wet stream is maintained close to inlet flow rate and Temperature and dry side does not approach saturation. Two effects are involved and counteracting on water transfer capacity:
    - At the dry side, as $T_{in,dry}$ increases, water relative humidity gets lower, because of higher P_{sat}, thus inducing a higher water content gradient through membrane;
    - At the wet side, instead, the increase of $T_{in,dry}$ leads to a lower heat exchange, which results in a higher T_{wet}, that, therefore, keeps P_{sat}, along wet channel, almost constant, inducing a lower water relative humidity; as a result, it affects negatively water concentration gradient across membrane.

4.3.3 Humidifier dynamics

The second part aims to assess an analysis of the dynamics of the component. Literature suggests average timescale of 3-5 sec. for water transport within the humidifier to reach a steady state condition.

Flow rates were changed by applying the same current cycle as the one used for the cell performance estimation: this allows to evaluate the performance of the component at different flow rates both at dry and wet side.

- The air entering at the dry side is assumed to be completely dry. It corresponds to the amount of air containing enough oxygen required by the reaction at the CCL.

$$\dot{N}_{tot\ in,dry} = \frac{j}{4F y_{O2,da}} A_{cell} \lambda_{cath} \frac{n_{cells}}{n_{plates} n_{ch,plate}}$$

- It is not possible to estimate the flow rate entering the wet side of the humidifier ex-ante: it depends on the kinetics, mass transport, external parameters (e.g. RH in both at cathode and anode sides) and dynamics of each cell. In this analysis, an average ratio between the outlet and the inlet air has been determined from the fuel cell model. Thus,

$$\dot{N}_{tot\ in,wet} = \frac{j}{4F y_{O2,da}} A_{cell} \lambda_{cath} \frac{n_{cells}}{n_{plates} n_{ch,plate}} \left(1 + \frac{y_{O2,da}}{\lambda_{cath}}\right) = 1.15 \dot{N}_{tot\ in,dry}$$

The outlet conditions were estimated at different λ_{cath}, by keeping temperature difference constant. Operating parameters are reported in Table 19:

Variable	**Value**
λ_{cath}	1.5 – 4 – 10
$T_{in,wet}$	80 °C
$T_{in,dry}$	50 °C
P_{hum}	2 bar
$RH_{in,wet}$	100%
$RH_{in,dry}$	0%

Table 19 operating parameters dynamic analysis humidifier

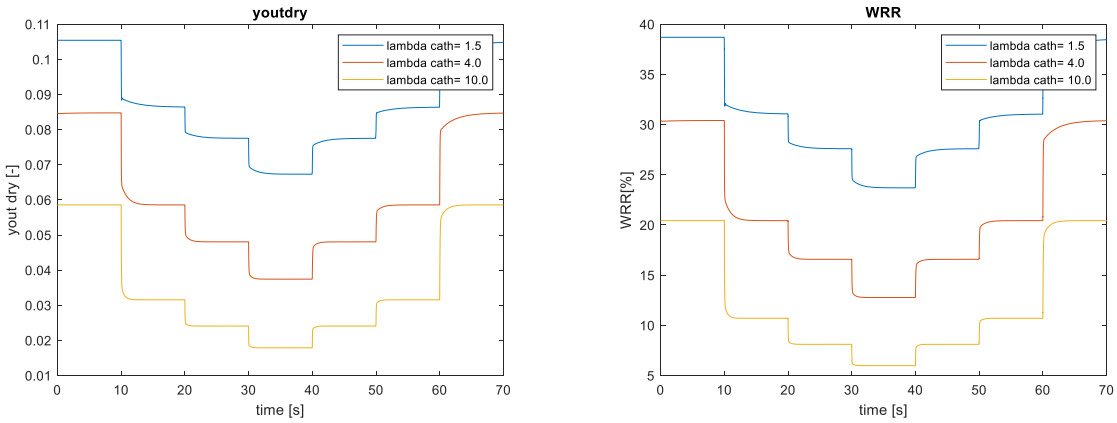

Figure 53 water molar fraction outlet dry side and WRR at different flow rates

The trends analysed in steady state are evident even in Figure 53: by increasing both flow rates, the performance of the humidification worsens, as the relative amount of water transferred though the membrane is much lower than the total flows through the channels. Time scale is in accordance with the reference value of 5 seconds found in the literature. Time needed to reach a steady state condition is higher at low flow rates, passing from less than 2 seconds at high stoichiometry, high current density, to almost 8 seconds at low stoichiometry, low current density.

4.3.4 Humidifier and stack model

The third part of the investigation aims to evaluate the effect of the dynamics of the humidifier to the performance of the FC stack.

- Temperature of the stack, equal to the inlet temperature at the wet side, has been kept constant, at stack boundary;

- The transient effect given by the compressor and manifolds has not been considered, and the dry air is assumed to adapt immediately after a step change in current density.
- In order to properly compare the FC stack model with the system model, the same $RH_{in,air}$ cycle as the one reached by the system at steady state has been applied to the FC stack system;
- Following the same principle, $\dot{n}_{in,wet}$ at the inlet of the wet side of the humidifier is equal to the $\dot{n}_{out,cath}$ once the steady state is reached.

Clearly, the dynamics of the two components interfere each other, causing global change in the performance of the system with respect to single-component analysis. The main differences between the single components model and the FC system model are:

- The air inlet at the cathode is not constant, neither the amount of water, as they depend on the outlet conditions of the humidifier. As it is shown in Figure 54, the presence of the humidifier causes a delay in the water molar fraction to reach steady state conditions of 3-4 seconds. Moreover, small overshoots and undershoots in the flow rate can be observed when external current instantaneously changes.

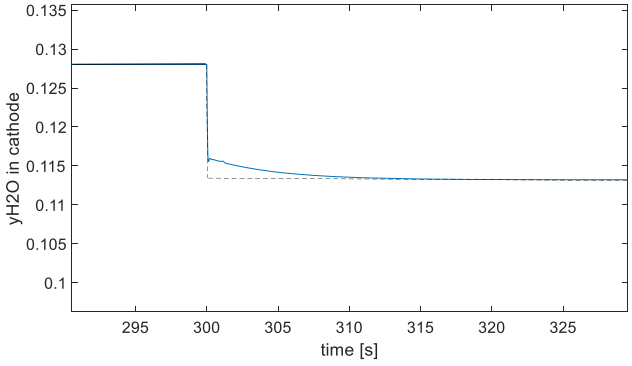

Figure 54 Effect of humidifier dynamics on air inlet stack

- The air inlet at the wet side of humidifier is not constant, as it depends on the outlet conditions of the stack. With respect to steady-state inlet, used to analyse the humidifier model, it is evident from Figure 55 that the system effect causes a very fast transient, concentrated in the first 2 seconds.

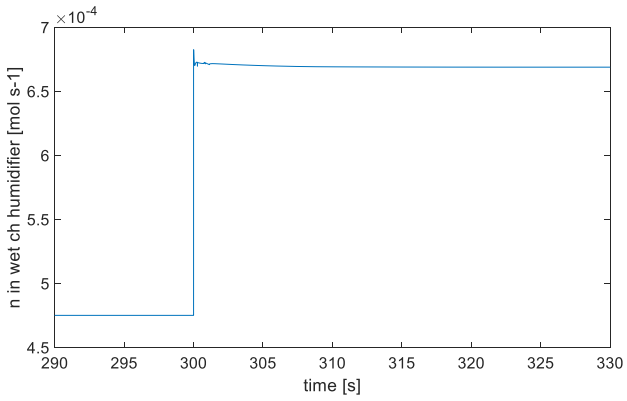

Figure 55 effect of stack dynamics on air inlet at the wet side of the humidifier

It can be said that both flow rate entering in the stack and in the wet side will be affected significantly by transport timescales of each component. Moreover, the system transients influence water transport through the membrane: the inlet water vapor is having a different transient evolution, because of the current step, to allow the humidifier to adapt to the new conditions. This effect can be clearly noticed by looking at the average membrane water content. For sake of clarity, only λ_m evolution at the cathode inlet and anode inlet are showed in Figure 56.

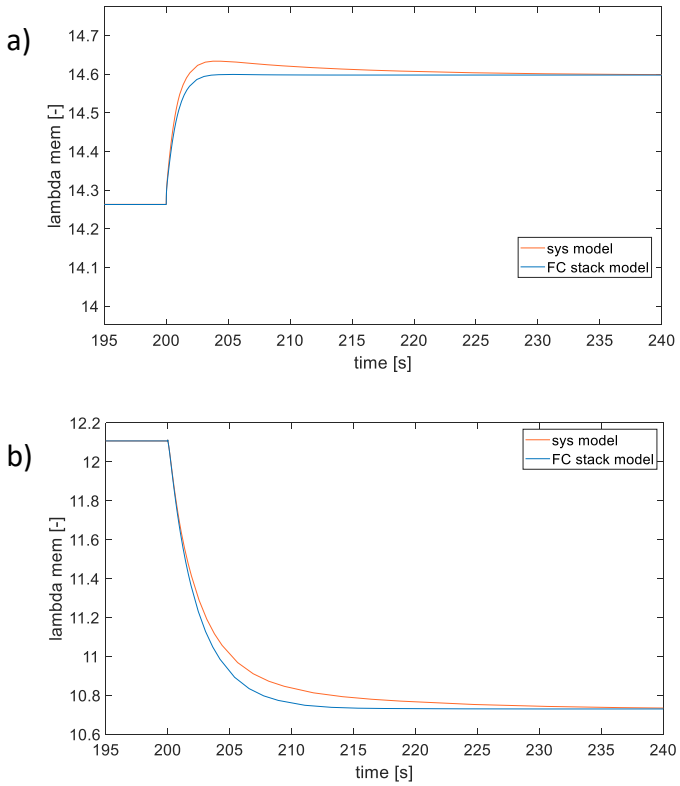

Figure 56 Effect of humidifier dynamics on membrane water content at inlet cathode(a) and outlet cathode (b)

As expected, the system changes the shape of the water content in the membrane, as well. The transient lasts 20 s, which is the usual time scale in the membrane to adapt to new conditions, at low current density, since it is not so hydrated. During a step upwards of current, water production at the cathode catalyst layer occurs immediately. Since the inlet air flow rate is still adapting to the new conditions, the concentration of water increases, and back diffusion is higher with compared to the FC stack model. The change in the shape is both related to the increasing inlet air flow rate in the next five seconds and water recirculation within the membrane.

The transient delay is even more evident by looking at membrane water content at the cathode outlet, which is also affected by the effect of channels transport delay.

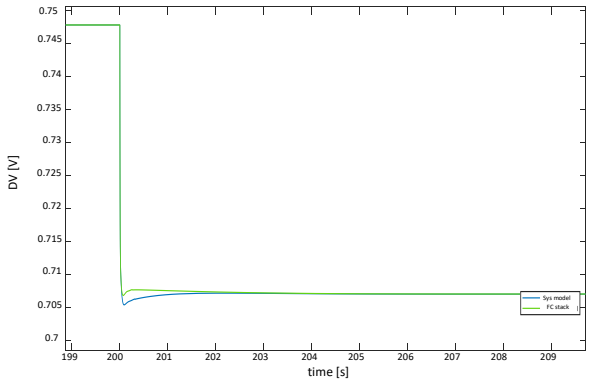

Figure 57 dynamics of combined humidifier and PEM stack voltage difference

By comparing the voltage of the FC stack model and the system model in Figure 57, the change is concentrated in the first five seconds. After current step change, flow rate at the dry side of the humidifier increases promptly, but it takes some time to reach cathode manifold. It determines a certain time period in which oxygen concentration is not enough to react, resulting into an additional voltage undershoot. When the dry flow rate immediately decreases, the delay effect linked with the transient of the humidifier, instead, enhances the overshoot as more oxygen than the steady state one is present at the reaction sites during the initial time-lapse.

4.4 Conclusions

The main results of this section are:

- First, the 1D cell model has been investigated. The attention has been mainly focused on water management, both static and dynamic simulations have been conducted. Moreover, a parametric study has been performed to show how the oxygen and water dynamics are influenced by the GDL and membrane thickness, respectively.
- Then, the effects due to the presence of the channels in the 1D+1D model have been analyzed. The static analysis predicts a water recirculation in the cell; as the current density increases the cathode inlet becomes more wet, while the anode inlet gets dryer. The influence of the external parameters, such as the inlet cathode RH and the cell temperature, on the water management is performed. Then, the influence of the channel dynamics over the CCL oxygen activity, the membrane water content and cell voltage has been studied.
- The humidifier model has been discussed; after a preliminary sizing to capture the real performances of the component, a parametric analysis is conducted with the aim of evaluating the influence of different inlet temperatures and flow rates on the performance of the humidifier; then, the humidifier dynamics has been investigated, fixing the inlet flow rate both at the dry side and the wet side.
- At the end, the fuel cell stack + humidifier system has been studied, analyzing how the two dynamics of the components are reciprocally influenced.

Chapter 5. Control strategies and system results

This section is organised as follow:

- First, after a brief explanation of the main control subsystems involved in a fuel cell system and an introduction of the PID controllers, the control strategies adopted in this work are presented in detail;
- Then, the main results of the fuel cell system are shown and discussed, considering a constant pressure regulation strategy;
- At the end, after the evidence of two relevant issues, an alternative control logic is proposed and commented.

5.1 Control loops and PID control

There are three major control subsystem loops in the fuel cell systems [13]:

1. The reactant control subsystem, which regulates the air/fuel supply, so to avoid reactants starvation;
2. The water management control subsystem, which aims to keep the stack within the desired value of humidity;
3. The thermal management control subsystem, which verifies and controls that the temperature of the stack is in the safe range.

This work is focused on the air subsystems control, on the water management control and on the thermal management control, while the fuel supply control has not been implemented. The regulation is achieved by means of self-tuning PID controllers, widely used in industrial control systems because of their simplicity and reliability, whose operating scheme is shown in Figure 58:

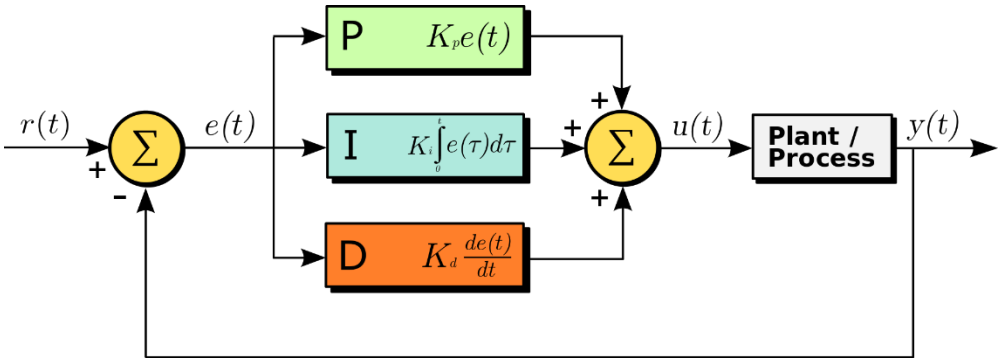

Figure 58 PID controller

A PID controller continuously calculates the error value as the difference between a desired setpoint and a measured process variable, and applies a correction based on proportional, integral and derivative terms (denoted P, I and D respectively). It is based on the following mathematical law:

$$u(t) = K_p e(t) + K_i \int_0^\tau e(\tau)d\tau + K_d \frac{de(t)}{dt}$$

Where $e(t)$ is the error function and $u(t)$ is the variable calculated by the PID. The effectiveness of the controller depends on the values of the three constants K_p, K_i and K_d, which must be found by means of the so-called loop tuning, so to obtain the desired response time. In this work the *MATLAB-Simulink self-tuning* toolbox has been used.

5.1.1 Air control subsystem

As already explained, the aim of the air control subsystem is to provide the required quantity of air at the cathode side. A compressor voltage control is used to achieve this task. In the following Figure 59 a general scheme of the subsystem is represented.

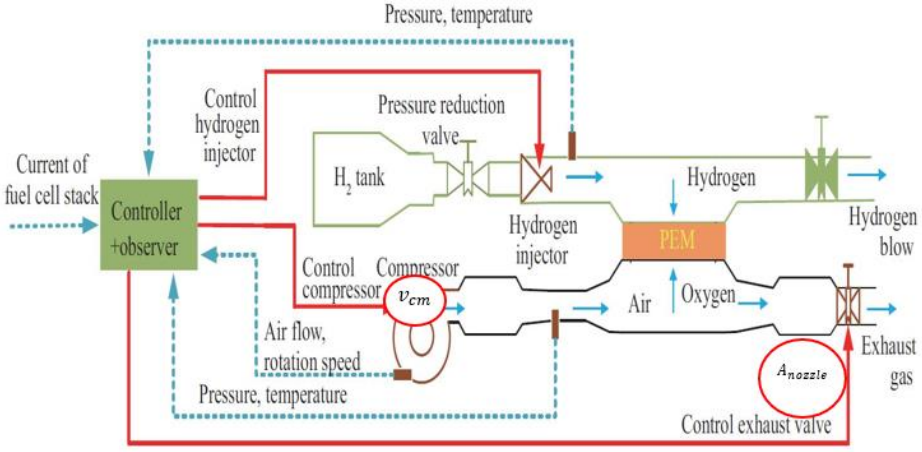

Figure 59 Air control subsystem

Compressor voltage control

The first controller aims to regulate the compressor motor voltage V_{cm}, so that the air mass flow developed by the compressor is equal to the one required by the stack, directly dependent on the current density J_{out}. This task needs to be achieved fast and efficiently to avoid excessive reduction of the stack voltage and slow net power response [30]. In Figure 60 a schematic representation is shown:

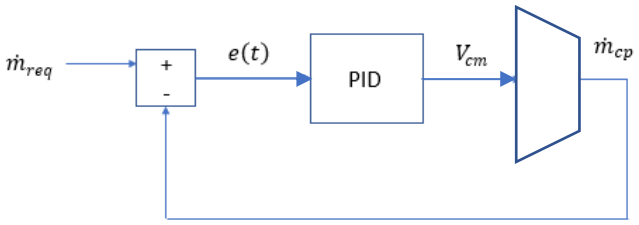

Figure 60 compressor motor voltage PID controller

5.1.2 Water management control subsystem

The purpose of the water management subsystem is to ensure the requested level of inlet RH to the air entering in the cathode side. The regulation is achieved by the exhaust valve control in the return manifold, which regulates the pressure of the system, as observed in Figure 59.

Exhaust valve control

The aim of the exhaust valve control (or back-pressure control) is to regulate the nozzle area of the exhaust manifold A_t, so to achieve the desired pressure level in the system. Working at high pressures is beneficial for the humidifier operation, since the water exchange mechanism is enhanced, as well as for the stack, whose performances increase with high-pressure operation. This regulation is connected to the compressor voltage control, since the air mass flow rate developed by the compressor depends on the compression ratio. A schematic representation of the exhaust valve control is shown in Figure 61:

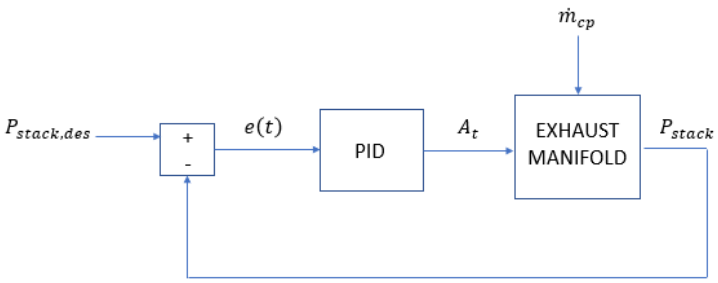

Figure 61 back-pressure PID control

At the same time working with high pressures, especially at low loads, negatively affects the compressor consumption, and so the system efficiency. It has been decided to give priority to the humidifier and stack operation, so the back-pressure valve keeps a constant system pressure, equal to 2 bar. This type of regulation is named *constant- pressure regulation*. Without this type of control, the pressure of the stack would be free to vary, depending on the power requested. This alternative regulation strategy, instead, is called *variable pressure regulation.*

5.1.3Thermal management control subsystem

The thermal management control subsystem aims to keep the stack temperature in the safe range. This purpose is achieved by means of two different controllers, highlighted in red in Figure 62; the first one controls the opening fraction of the bypass valve [16], while the second one controls the fan speed.

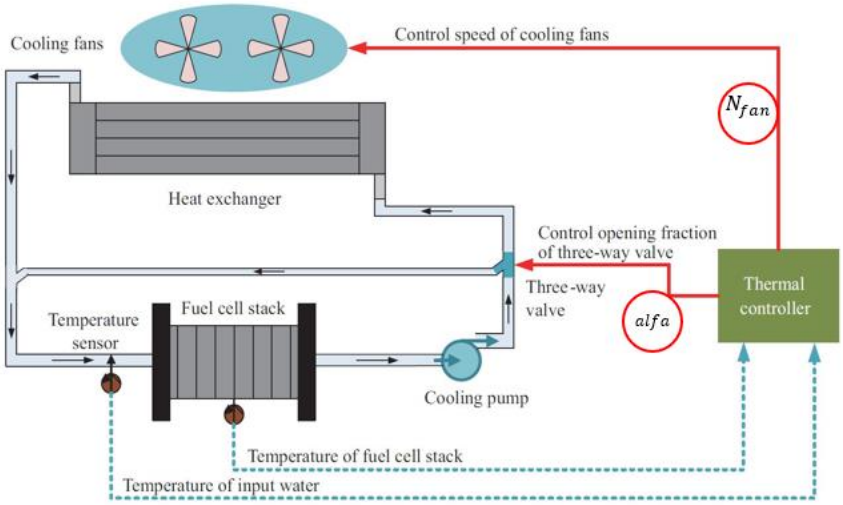

Figure 62 Thermal management control

Three-way valve opening fraction control

The aim of this controller is to vary the opening fraction of the bypass valve α, so to keep the coolant inlet temperature equal to a desired valued at $70\ °C$.[16] The coolant entering the fuel cell derives from the mixing between the coolant flow exiting the radiator, and the coolant that bypasses it. At high load operation the cooling load required by the stack is relevant, so α will be low. At low load operation, instead, the thermal energy produced by the stack is lower: hence, the opening fraction will be higher, and most of the coolant will tend to bypass the radiator. The Figure 63 shows a schematic representation.

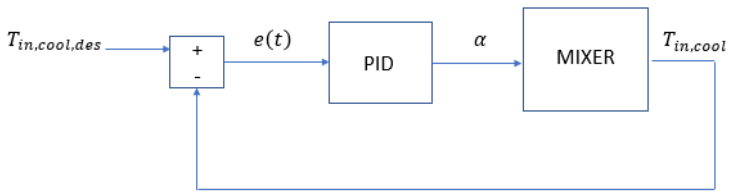

Figure 63 Three-way valve opening fraction PID control

Fan speed control

The fan speed control is different from the previous ones, since it has not been implemented by a PID. When the coolant temperature difference between the outlet and the inlet of the stack ΔT_{cool} overpasses a fixed threshold, the fan speed instantaneously arises to increase the air speed flowing through the radiator. In this way the coolant temperature at the outlet

of the radiator will get lower, leading to a reduction of ΔT_{cool}. Two different fan speeds have been set:

$$N_{fan} = 500\ RPM \qquad if\ \Delta T_{cool} < 10\ °C$$
$$N_{fan} = 1000\ RPM \qquad if\ \ \Delta T_{cool} > 10\ °C$$

5.2 System results

This section includes all the most relevant system results. The solver ODE 15s has been used for the simulations, so to achieve a good balance between model accuracy and computational time. The analysis has been organized as follow:

- After a brief introduction over the NEDC cycle, the velocity, net power and gross power profiles are shown;
- The stack performance is analyzed; so, the stack voltage-current profile is presented, as well as the oxygen activity towards the CCL, and later commented;
- The behavior of the main variables involved in the water management is discussed;
- The stack efficiency is evaluated, showing two fundamental problems that affect the performances of the system, because of the constant pressure regulation system.
- At the end, a comparison between constant pressure regulation and variable pressure regulation is performed, focusing of advantages and disadvantages of each configuration.

5.2.1 NEDC cycle and stack power

The New European Driving Cycle (NEDC) is a driving cycle, designed to assess the emission levels of car engines and fuel economy in passenger cars. It lasts 1180 seconds and it composed by two parts[50]:

- The Urban Driving Cycle **ECE-15** (or just **UDC**), designed to represent typical driving conditions of busy European cities, characterized by low engine load, low exhaust gas temperature, and a maximum speed of 50 km/h. The cycle is repeated four times, each 195 seconds long, for a total duration of 780 seconds; the average speed of 18.35 km/h [51].
- The Extra-Urban Driving Cycle **EUDC**, designed to represent more aggressive, high speed driving modes. The maximum speed of the EUDC cycle is 120 km/h. It globally lasts 400 s, with an average speed of 62.6 km/h [51].

Table 20 reports the main operating conditions the following analysis has adopted.

Parameter	**Value**
λ_{cath} [-]	1.5
λ_{an} [-]	1.2
$T_{stack,in}$ [K]	353.15
A_{cell} $[cm^2]$	237
t_{mem} [µm]	10
t_{GDL} [µm]	200
P_{stack} [Pa]	controlled
$RH_{in,stack}$ [-]	controlled
$RH_{in,an}$ [-]	50 %

Table 20 operating parameters used for the NEDC simulation

In Figure 64 and Figure 65 the car velocity profile required by the NEDC cycle and the power requested by the stack are presented. The net power profile considers just the velocity-power conversion by means of the vehicle model, while the gross power considers even the auxiliary consumptions.

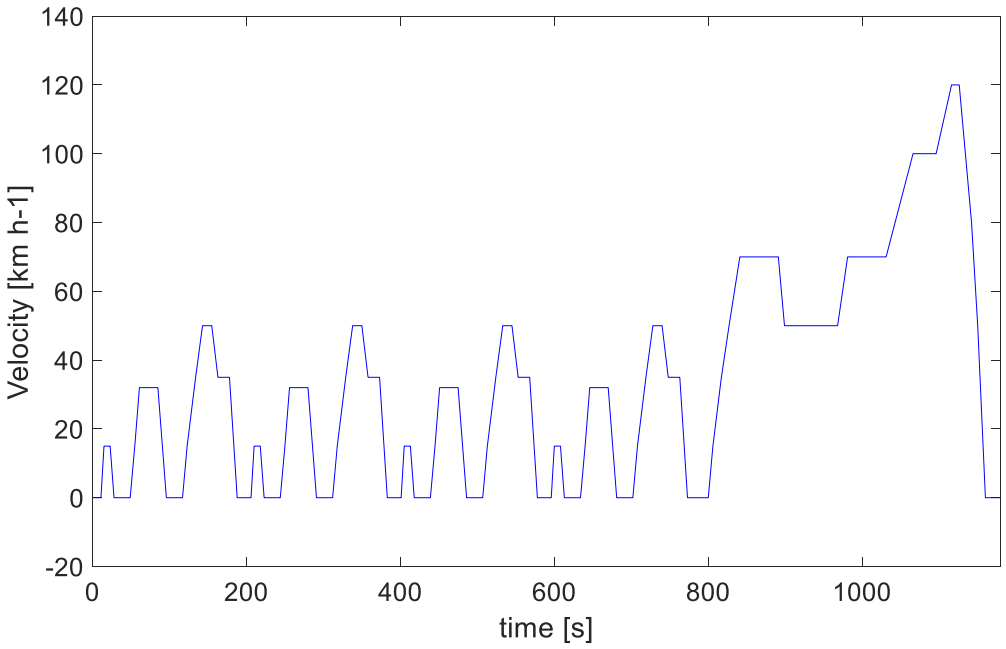

Figure 64 NEDC velocity

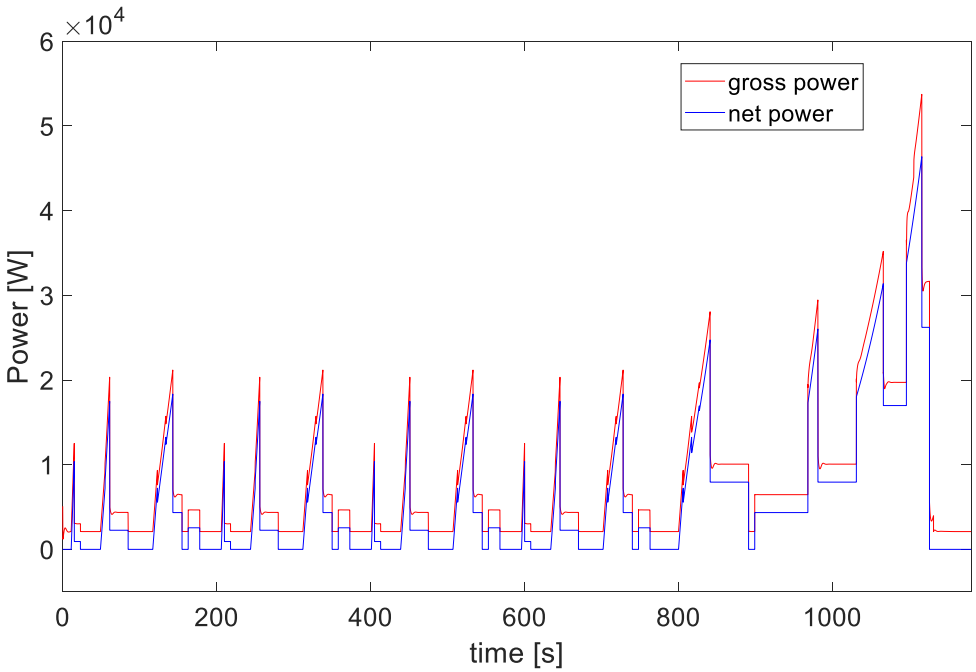

Figure 65 NEDC net and gross power

As already explained in the vehicle model description, the auxiliaries included in this work are the compressor, the fan, and a constant share power of 500 W, which accounts for all the other consumptions. As it can be observed in Figure 66, the auxiliary consumption increases in the high-power zone of the cycle, mainly due to the increase of the power absorbed by the compressor, since a higher air flow rate is required by the stack. The power consumption of the compressor is reported below. The maximum power peak, about 4,9 kW, occurs at 1116 seconds, when the velocity reaches its maximum value of 120 km/h. It can be noticed that in the low-power zone, the power absorbed by the compressor is lower, since the lower air flow required by the stack, but still relevant. This because of the control exhaust valve control system, which aims to keep the pressure of the stack equal to 2 bar.

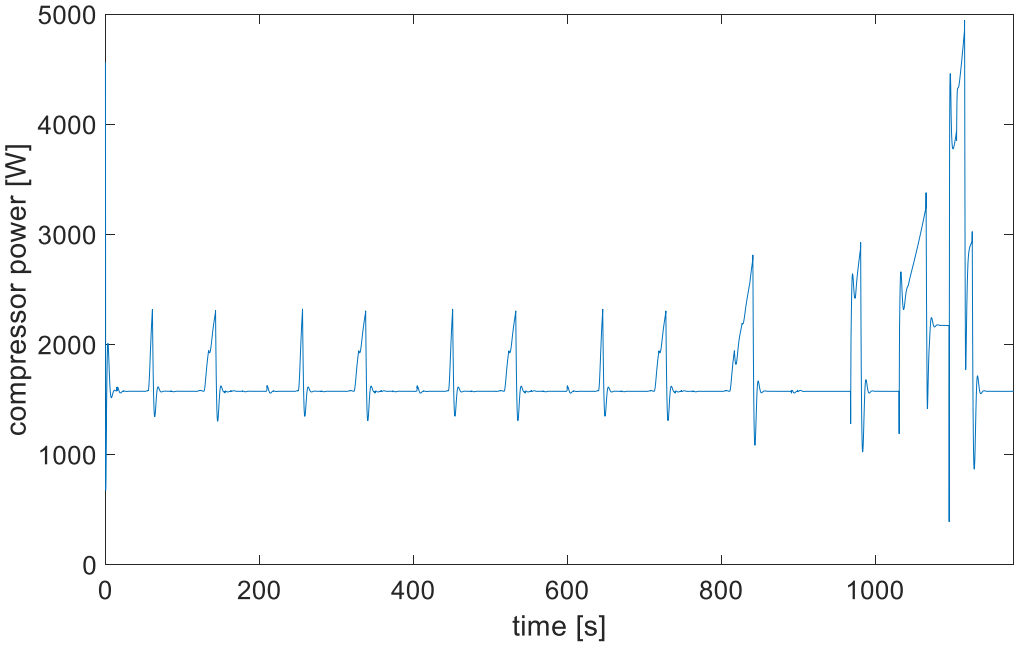

Figure 66 NEDC compressor power

5.2.2 Stack performance

In this section the stack voltage-current and the oxygen activity towards CCL profiles are presented. The stack voltage has been obtained multiplying the cell voltage by the number of the cells, equal to 370, while the stack current is the product between the cell current and the cell area, equal to 237 cm2 in this work.

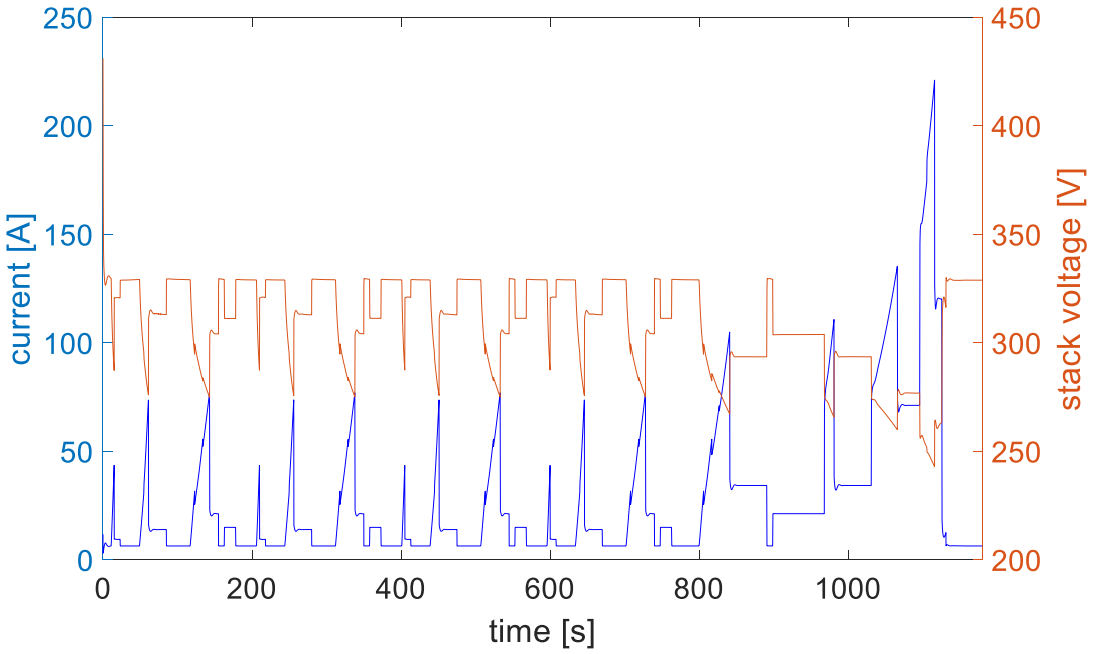

Figure 67 NEDC current and stack voltage

As it is shown in Figure 67, the current-voltage peaks are the opposite; when the power required by the cycle increases, the current increases as well, and the voltage gets lower. The voltage lies in the typical automotive range, between 0.9 and 0.65 V per cell approximately. The minimum is reached at 1116 seconds, where the current reaches it maximum point, around 0.95 A/cm2. This is also the point where the CCL oxygen consumption is the greatest, as observed in Figure 68, which shows the $a_{O2,cl}$ behavior in the channels 1, 3 and 6 respectively.

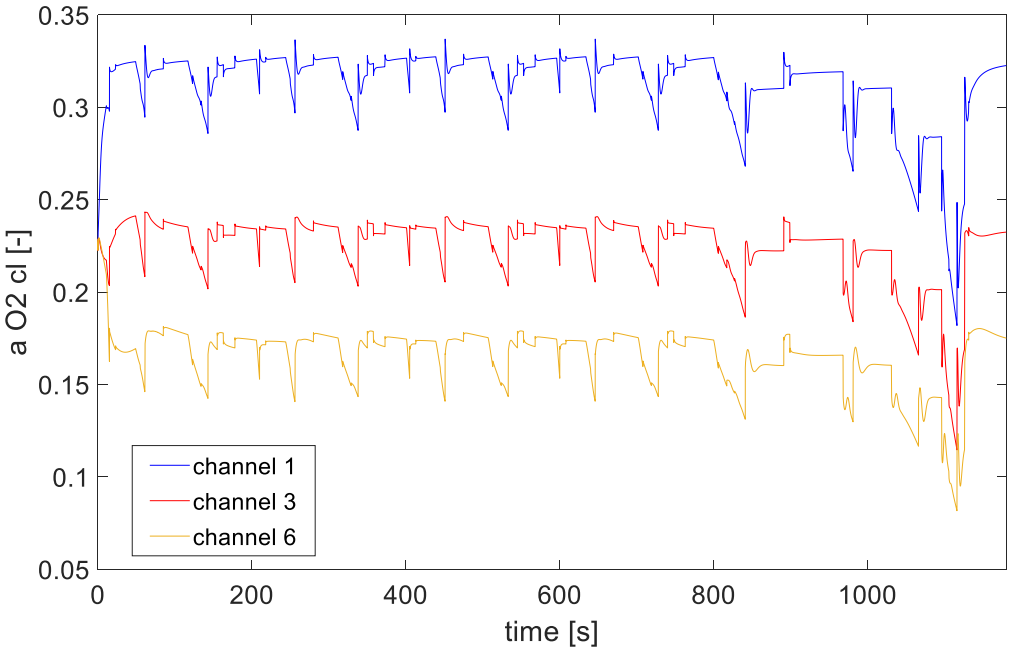

Figure 68 NEDC oxygen activity at CCL profile

The channel effect, analyzed and discussed in the fuel cell model simulation chapter, is still evident. In fact, the peaks get mellower passing from the channel 1 to the channel 6, because of the oxygen transport along the cathode channel. Two explicative examples are shown in Figure 69, where the ranges between 620 and 680 seconds, and between 1020 and 1080, are considered.

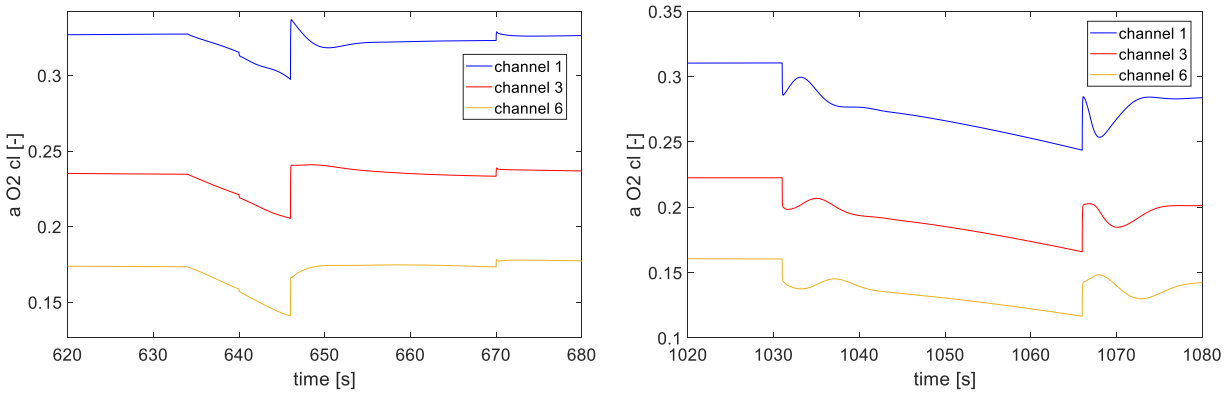

Figure 69 NEDC oxygen activity at CCL inlet and outlet cathode

5.2.3 Water management

The profile of the net water flux in membrane, as well as the medium water content, are shown in Figure 70 and Figure 71. In both cases the analysis has been restricted to the channels 1, 3 and 6.

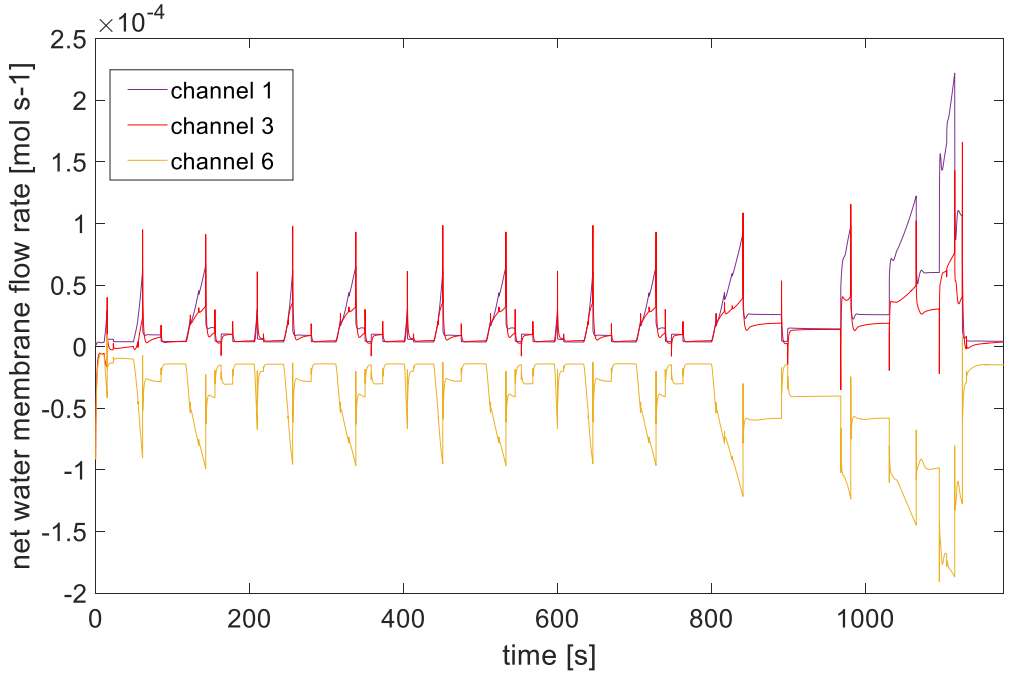

Figure 70 NEDC net water membrane flow rate

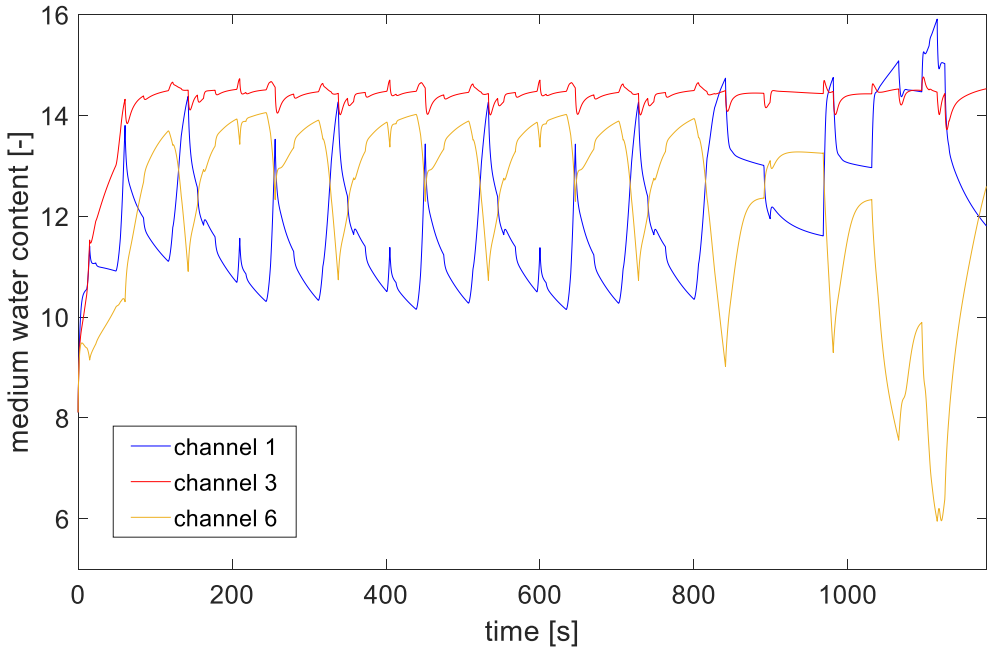

Figure 71 NEDC membrane water content

Observing Figure 70, it can be noticed that, both at low-load operation and at high-load operation, the net membrane water flux is positive for the channels 1 and 6, while it is negative for the channel 6. This indicates that the drag transport is predominant in the channels 1 and 3, while at the anode inlet (channel 6), the back diffusion is the winning water transport mechanism; this trend is the same as the one observed in the 1D+1D model, in the fuel cell model simulation chapter. Increasing the power required by the stack, the relative difference between these fluxes increases, meaning that the quantity of water circulating in the stack is higher. The behavior of the net membrane water flux influences the medium water content profile, presented in Figure 71. As it expected, the cathode and the anode inlet experience the greatest water flux variations, leading to a consistent variation of λ_m along the driving cycle. The water content of the channel 3 is more stable than the one at the cathode/anode inlets, meaning that the center of the stack does not suffer from such relevant water flux variation. Moreover, it can be noticed that at each power peak corresponds peak in the net membrane water flux, and consequently a local maximum for λ_m in the channel 1 and a local minimum for λ_m in the channel 6 is reached. This trend becomes even more evident at high-load operation, where the anode inlet becomes considerably dehydrated. This is also because the channel 6 experiences higher temperature with respect to the other channel blocks, as can be observed in Figure 72.

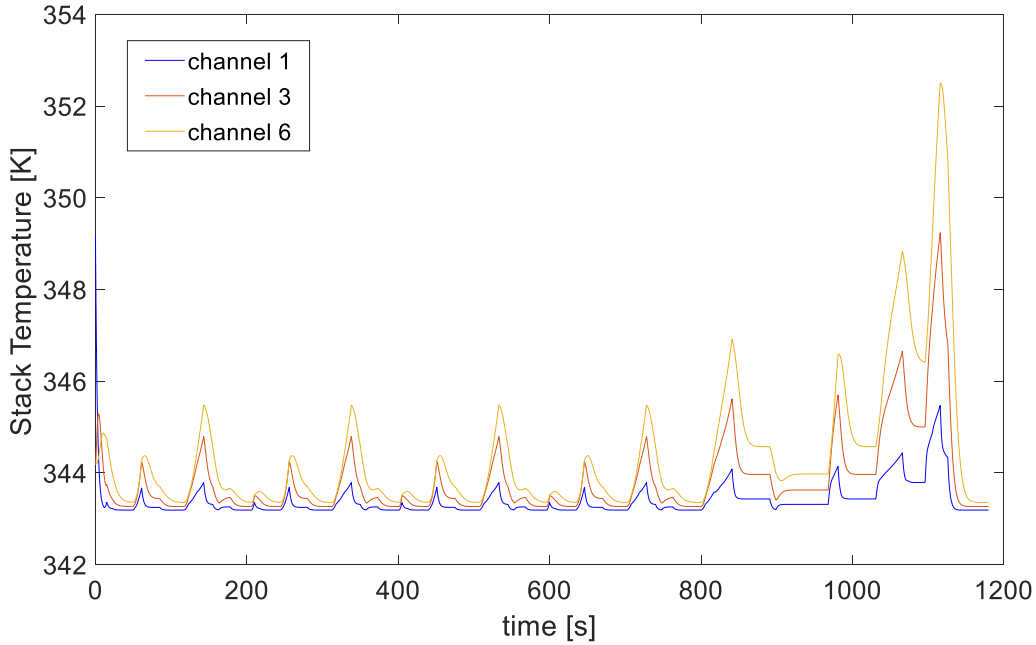

Figure 72 NEDC stack temperature

As expected, even the temperature profile follows the power peaks (Figure 72); it increases along the channel length because of the co-flow configuration between the coolant and the air flowing in the cathode side. The maximum temperature peak is reached in the channel 6 at 1116 seconds, when the power required by the stack is the highest one.

5.2.4 System efficiency

The system efficiency is evaluated as follow [52]:

$$\eta_{sys} = \eta_{stack}\eta_{fuel}\eta_{peripheral}$$

Where, under the hypothesis of homogeneity among all the cells composing the stack:

$$\eta_{stack} = \frac{V_{cell}}{1.253}$$

$$\eta_{fuel} = \frac{1}{\lambda_{an}}$$

$$\eta_{peripheral} = \frac{P_{net}}{P_{gross}}$$

The stack and the system efficiency are reported in Figure 73:

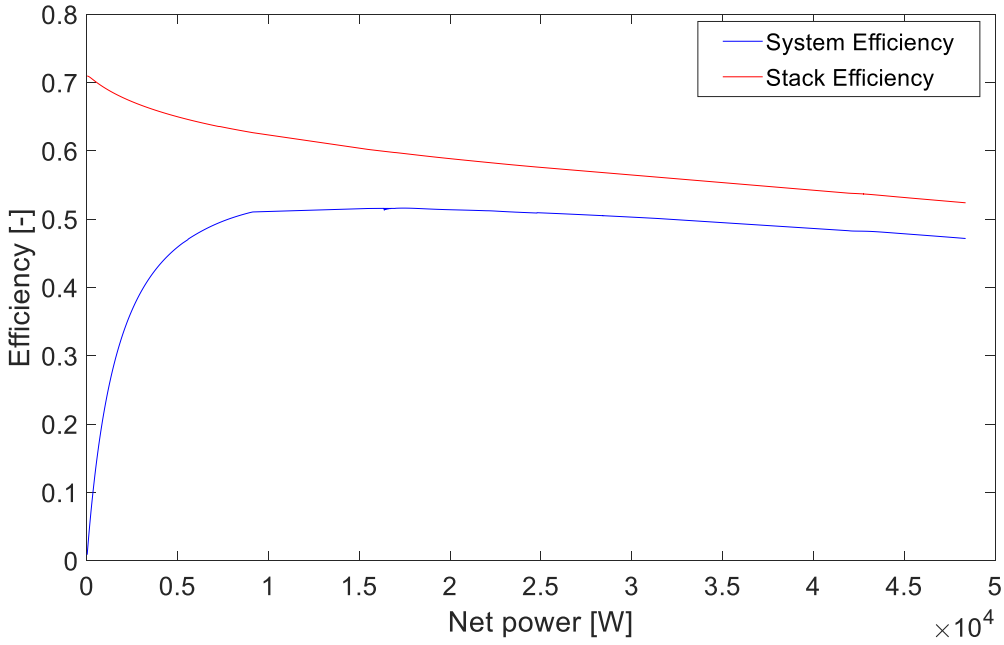

Figure 73 NEDC stack and system efficiencies

The stack efficiency η_{stack} decreases as the net power increases, being directly dependent on the cell voltage. It lies in between 0.7 and 0.58 approximately, typical values found in literature. It can be noticed that in the low-load operation range, η_{sys} is very low: this because, as previously observed, the compressor consumption is relevant even when the power produced by the stack is very low, due to the exhaust valve control strategy adopted. After a rapid increase, the system efficiency reaches a maximum of 0.52, around 18 kW of net power produced; then it slightly decreases, both because of the increase of the auxiliary consumption, and because of the reduced stack efficiency at high-load operation range.

So, from this analysis two essential issues have been revealed:

- At low-load operation the system efficiency is very low, due to the high share of auxiliary consumption;
- At high-load operation the anode inlet (channel 6) becomes consistently dehydrated, leading to an increase of the ohmic losses, and so a reduction of the cell voltage. This is due both to the increase of the back-diffusion mechanism at high-load operation, since the increase of the water fluxes involved, and to the increase of the stack temperature, because of the coolant flow configuration mainly.

5.3 Variable pressure alternative solution analysis

An alternative solution is presented, with the aim of trying to overcome the two criticisms individuated in the constant-pressure regulation. The back-pressure valve cross-sectional are is kept fixed equal to 0.010864 m2 so that the pressure is free to vary along the driving cycle; at low-load operation the pressure of the system will be low, while it will tend to increase at high-load operation. This solution presents advantages and disadvantages:

- Especially at low load operation the compressor consumption is expected to be low, since the low compression ratio required. This is beneficial for the system efficiency;
- Lower pressure worsens the humidifier operation, leading to a lower stack inlet RH.
- Lower stack inlet RH, combined with low system pressure, negatively affect the fuel cell stack performances, leading to a reduction of the stack efficiency.

So, after this primarily analysis, it is not evident if a variable pressure regulation is beneficial or not for the system efficiency. The aim of this section is to analyze the effectiveness of the variable pressure regulation with respect to the constant-pressure one, focusing on its influence on the compressor, humidifier and stack operation. At the end, a comparison between the stack and system efficiencies of the two regulation strategies is performed.

5.3.1 Compressor operation

As mentioned above, the variable pressure regulation is beneficial for the compressor, especially at low load operation. The following graphs (Figure 74, Figure 75) report the stack pressure and the compressor consumption, both with constant and variable pressure regulation.

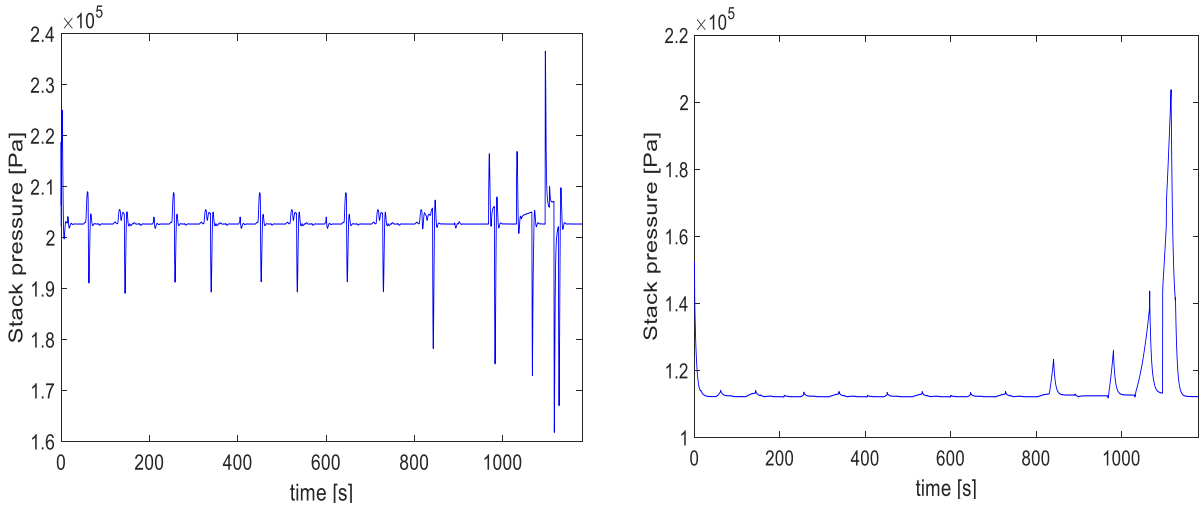

Figure 74 NEDC stack pressure comparison

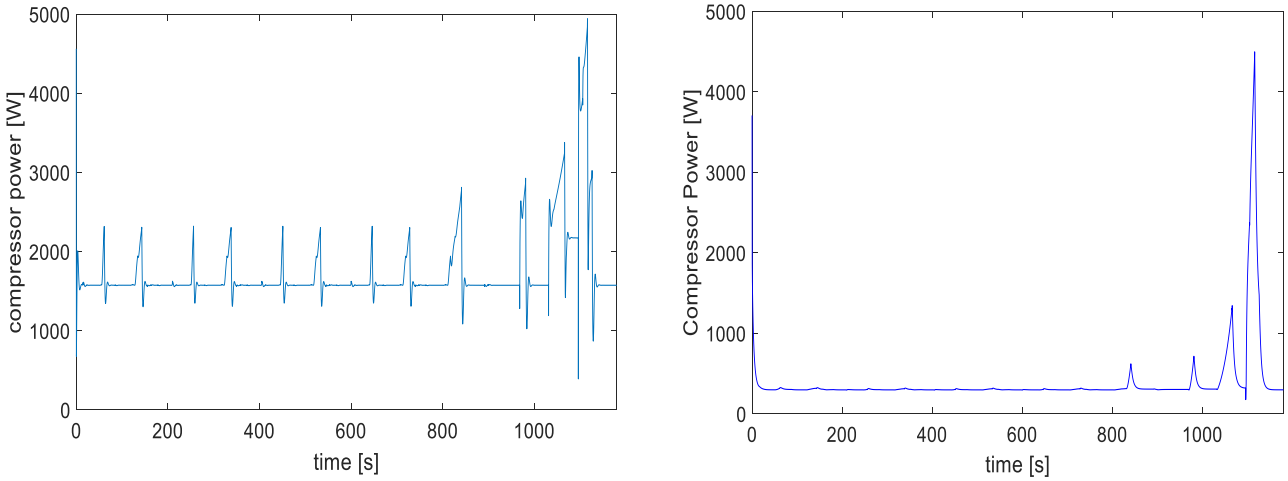

Figure 75 NEDC compressor power comparison

As expected, the differences between the two cases are evident mainly in the low-power zone. In the case of variable pressure regulation, the pressure is very low, about 1.2 bar (Figure 74). The influence of the PID controller can be observed: the variable pressure regulation requires a constant cross-sectional area of the exhaust valve, so the PID controller is not needed. Consequently, the stack pressure and compressor power profiles (Figure 75) are less variable in low load operation, since the system does not have to adapt to same pressure level. At high load operation, the differences among the two regulation strategies are much less relevant, as observed in the figures. So, $\eta_{peripheral}$ is expected to be similar when the power required by the stack is high.

5.3.2 Humidifier operation

A lower system pressure negatively influences the humidifier operation, since the water exchange mechanism gets worse. The profiles of the stack inlet RH, both for the constant and variable pressure regulation strategy, are shown below.

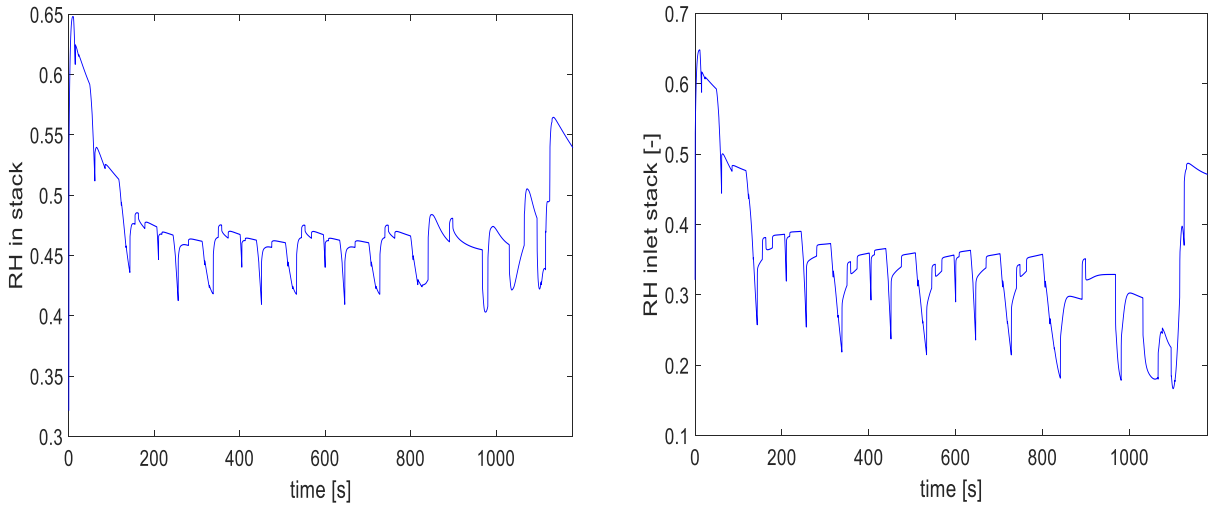

Figure 76 NEDC RH inlet cathode comparison

As it can be observed in Figure 76, the adoption of the variable pressure regulation leads to lower stack inlet RH values. This affects the operation of the fuel cell stack, mainly at high powers, where the RH inlet variation becomes more relevant.

5.3.4 Fuel cell stack operation

The current-voltage profile using the variable pressure regulation is presented, and later the stack voltage only is compared with the one obtained adopting the constant pressure solution, explaining the main differences among the two cases.

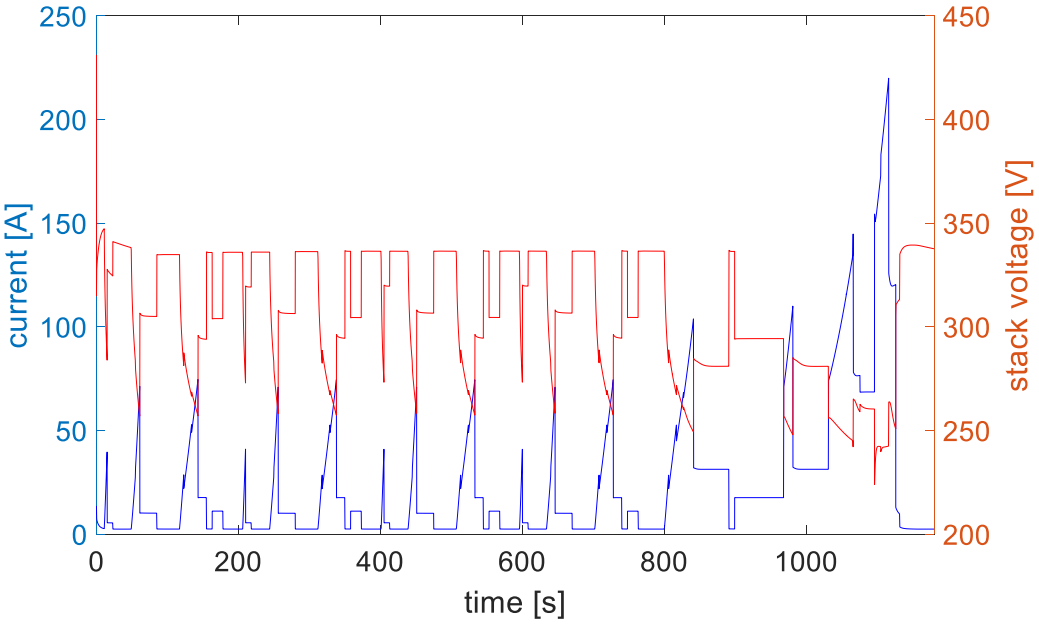

Figure 77 NEDC voltage at variable pressure

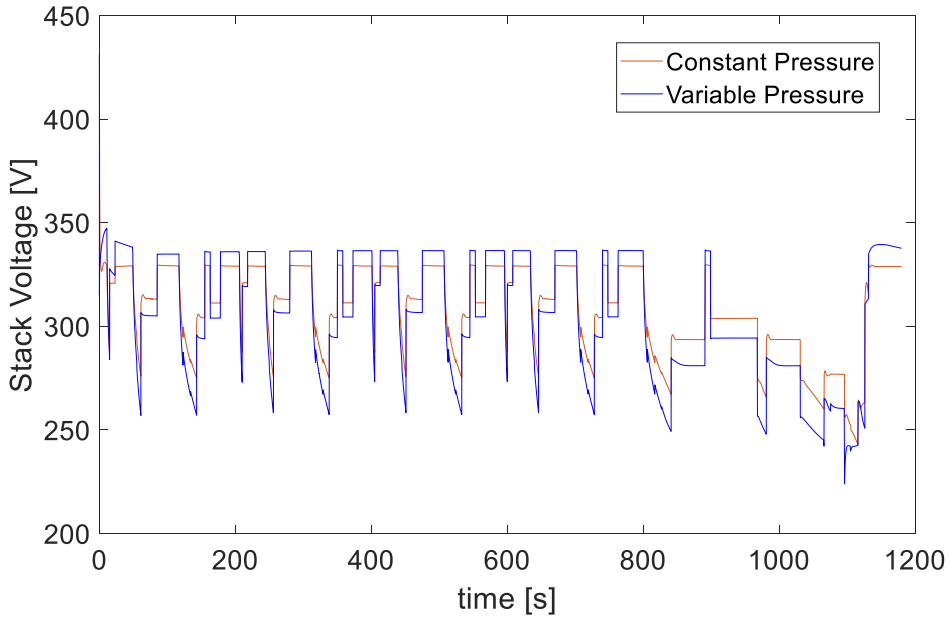

Figure 78 NEDC voltage comparison

As it can be noticed, two different trends are evident: at very low load, the voltage produced adopting the variable pressure regulation is higher, while in all the other operating point is lower. This suggest that two different conflicting phenomena occurs:

- On one side, the reduction of the compressor consumption occurring at low pressures leads to a decrease of the gross power produced by the stack; the current generated by the stack is lower, hence the voltage tends to be higher;
- On the other side, low pressure operation, combined with low stack inlet RH,

worsens the stack performances, leading to a reduction of the stack voltage.

So, observing figure Figure 78 it can be observed that at very low load, the first phenomenon is more relevant, as the stack voltage adopting the variable pressure regulation is higher. In all the other operating points, the trend is the opposite; this indicates that the second phenomenon is prevailing. At high loads, it has been noticed that the stack pressures are closed, among the two regulation strategies analyzed. So, the reduction of stack voltage is mainly due to the lower performance of the humidifier; a lower stack inlet cathode RH leads to a lower membrane water content, hence to higher ohmic losses. In the following figures the membrane water content profiles, for both regulation strategies, are shown.

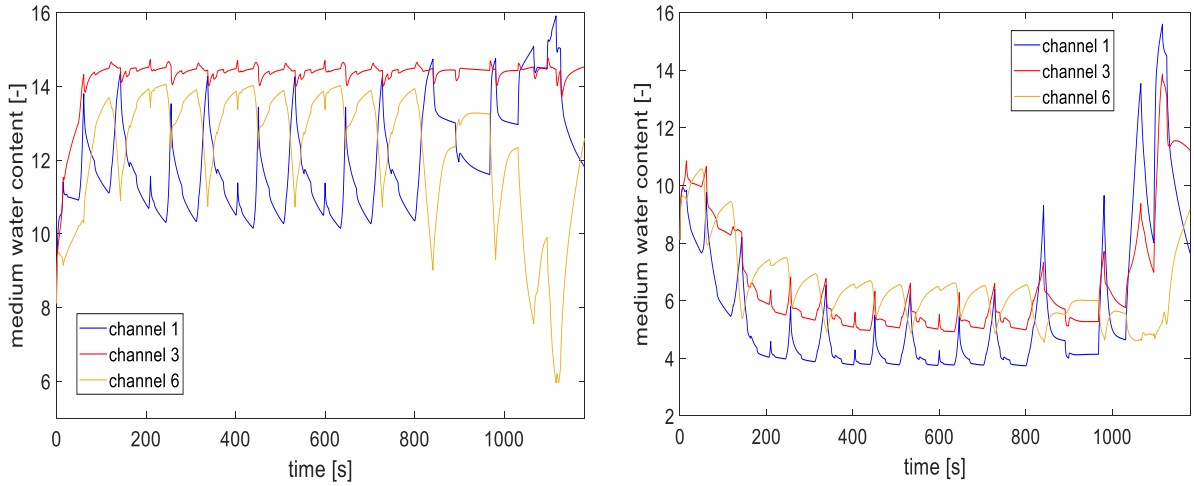

Figure 79 NEDC membrane water content comparison

It can be noticed that lower stack pressures lead to lower membrane water content, as expected. With respect to the constant regulation strategy, the medium water content variation in the channel 6 is less severe at high load.

5.3.5 Stack-system efficiencies comparison

Finally, a comparison between the stack and system efficiencies between the two regulation strategies is performed. Results are reported in Figure 80:

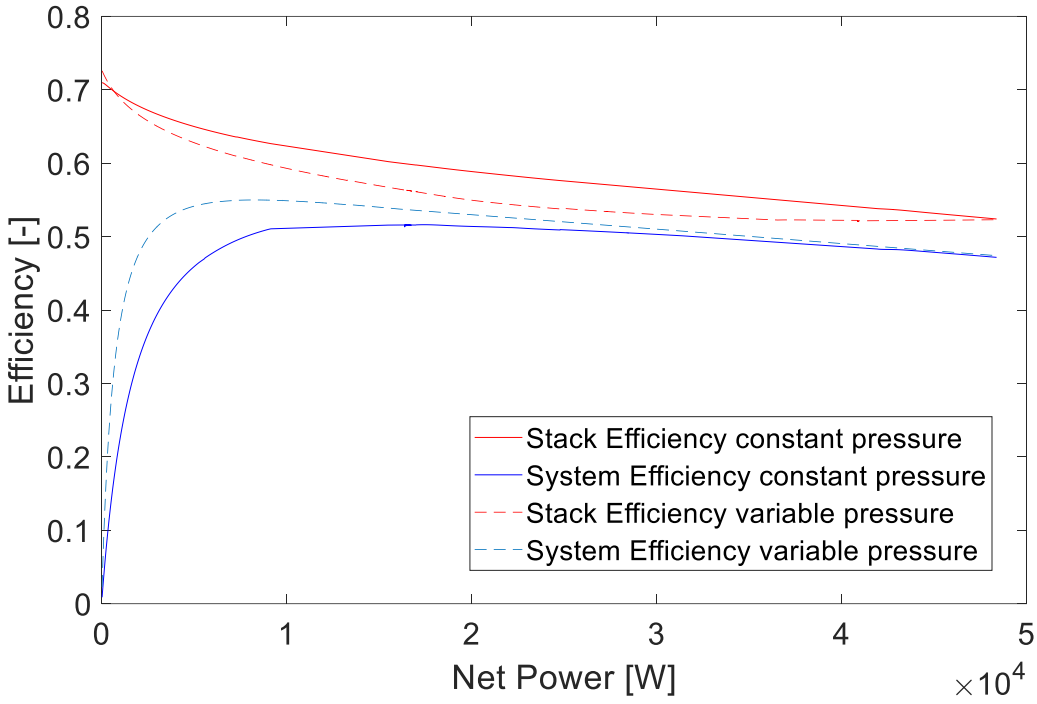

Figure 80 NEDC efficiency comparison

It can be noticed that, using a variable pressure regulation with respect to a constant one:

- The stack efficiency is globally lower, since the voltage produced is lower. This is not true at very low load operation, as previously observed, since the voltage produced is higher. At very high load operation, the stack pressure is around 2 bar, hence the stack efficiencies are very close.
- The system efficiency is globally higher, especially at low load operation. So, the benefits derived from the lower compressor consumption overcome the negative effects on the stack and humidifier operation due to the low pressure of the system. Increasing the load, the reduction of the stack efficiency becomes more relevant, and so the advantages of the variable pressure regulation are less evident.

5.4 Conclusions

- A brief analysis of the main control adopted in the system is performed; to give priority to the stack-humidifier operation, it has been decided to regulate the back-pressure valve so to maintain the pressure of the system equal to 2 bar;
- The main results obtained with a constant pressure regulation, are presented; the attention has been focused on the stack power and on the stack performances, showing how the water management is affected. Then, the stack and system

efficiency profiles are discussed. Two problems connected with this regulation strategy have been individuated: a high compressor consumption at low loads, and a severe inlet anode dehydration at high loads.

- To overcome these problems, a variable pressure regulation strategy has been implemented; the results have been compared with the constant pressure strategy. Using this regulation, the compressor consumption at loads considerably decreases, but the stack-humidifier performances get worse. The stack inlet RH gets lower, and this, combined with low pressures in the system, contributes to keep the membrane globally more dehydrated, accelerating the degradation phenomenon.
- Finally, stack and system efficiencies obtained with the two different pressure regulation strategies have been compared; the variable pressure regulation strategy leads to lower stack performances, but to higher system efficiency. For this reason, this preliminary analysis suggests that this regulation is the more effective than the constant pressure one.

Conclusions and Future Work

A PEM fuel cell dynamic system model focused on the air loop, with a 1D+1D fuel stack model, has been modelled. The model takes approximately 15 hours to perform the NEDC with Simulink. The Ode15s has been used, so to achieve a good level of accuracy maintaining an acceptable computational time.

First, the fuel cell dynamic model has been studied by means of galvanostatic step simulations to investigate the main dynamic phenomena involved. The relevance of the cell geometrical parameters has been highlighted, as they influence both performances and time-scale dynamics. From the 1D model to the 1D+D one, substantial differences have been noticed: the anode dehydration, as well as the variation of the time-scale of the main variables influencing the performance of the cell due to the mass transport delay in the channels are not visible in a 1D FC model. Then, the importance of the humidifier has been discussed, showing how it influences the stack dynamics.

In the last chapter the NEDC has been simulated. Because of the 1D+D fuel cell dynamic model implementation, the anode inlet dehydration at high-load operation is revealed and analyzed. Then, the relevance of the control strategy adopted is demonstrated. A comparison between the constant pressure regulation and the variable pressure regulation is conducted; the performances of the system considerably change, indicating that the selection of the proper control strategy is crucial for the system operation. Moreover, it has been demonstrated that the variable pressure regulation is globally better than the constant pressure one from a system efficiency point of view; on the other side, the 1D+1D fuel cell model has revealed that the cell membrane, in case of variable pressure regulation, is more dehydrated than the previous case: this can accelerate the degradation phenomenon.

This is one of the strength points of this model: the ability to perform a system analysis, but without losing accuracy on the PEM cell unit, with a focus on the 1D+1D evolution of the water fluxes, as well as water management, oxygen distribution and local temperature. Several improvements are suggested to increase model precision and complexity:

- *Fuel cell-battery hybridization*: as already said, the battery has not been modelled in this work, even if it covers a great importance in the real operation. A battery model, as well as a power management control system, is needed to better simulate the real operation of PEMFC stack in automotive application.
- *Liquid saturation*: presence of liquid water in the cell has been neglected in this work,

even if it heavily affects stack performances in real operations; a liquid saturation model is highly suggested to increase the level of accuracy and precision of the model.

- *Hydrogen loop model and anode model improvement*: the hydrogen loop has not been modelled, even if the importance of proper anode hydration has been captured in the present work. Hydrogen level of hydration, in fact, highly affects water transport through the membrane, thus the overall performance of the stack.
- *Control strategy improvement:* the selection of proper control strategy is crucial for system operation and different alternative regulation should be analyzed and compared.
- *Experimental validation:* the model has not been fully validated. Experimental data can be used to calibrate the main variables to achieve a high-fidelity model.

Bibliography

[1] W. R. W. Daud, R. E. Rosli, E. H. Majlan, S. A. A. Hamid, R. Mohamed, and T. Husaini, "PEM fuel cell system control: A review," *Renew. Energy*, vol. 113, pp. 620–638, 2017.

[2] J. T. Pukrushpan, "Modeling and control of fuel cell systems and fuel processors," *Mech. Eng.*, p. 133, 2003.

[3] B. Wu, "Fuel Cell Hybrid Electric Vehicle Powertrain Modelling and Testing," p. 243, 2014.

[4] T. E. Springer, T. A. Zawodzinski, and S. Gottesfeld, "Technical In-formation Bulletins 465-223,465-225, 465-246. 6. P. Wagner," *J. Electrochem. Soc*, vol. 138, no. 8, p. 208, 1991.

[5] T. F. Fuller, "Water and Thermal Management in Solid-Polymer-Electrolyte Fuel Cells," *J. Electrochem. Soc.*, vol. 140, no. 5, p. 1218, 2006.

[6] J. C. Amphlett, "Performance Modeling of the Ballard Mark IV Solid Polymer Electrolyte Fuel Cell," *J. Electrochem. Soc.*, vol. 142, no. 1, p. 9, 1995.

[7] Y. Wang and C. Y. Wang, "Ultra large-scale simulation of polymer electrolyte fuel cells," *J. Power Sources*, vol. 153, no. 1, pp. 130–135, 2006.

[8] "Amphlett_1996_Journal-of-Power-Sources.pdf." .

[9] M. Ceraolo, C. Miulli, and A. Pozio, "Modelling static and dynamic behaviour of proton exchange membrane fuel cells on the basis of electro-chemical description," *J. Power Sources*, vol. 113, no. 1, pp. 131–144, 2003.

[10] J. Jiao, F. Chen, Y. Yu, J. He, and X. Chen, "Modeling and simulation of PEMFC stack dynamic performance," *Proc. - 2017 Chinese Autom. Congr. CAC 2017*, vol. 2017-Janua, pp. 2871–2876, 2017.

[11] P. R. Pathapati, X. Xue, and J. Tang, "A new dynamic model for predicting transient phenomena in a PEM fuel cell system," *Renew. Energy*, vol. 30, no. 1, pp. 1–22, 2005.

[12] W. Yu, X. Sichuan, and H. Ni, "Air Compressors for Fuel Cell Vehicles: An Systematic Review," *SAE Int. J. Altern. Powertrains*, vol. 4, no. 1, pp. 115–122, 2015.

[13] J. T. Pukrushpan, A. G. Stefanopoulou, and Huei Peng, "Modeling and control for PEM fuel cell stack system," no. November 2014, pp. 3117–3122 vol.4, 2003.

[14] A. C. Rojas, G. L. Lopez, J. F. Gomez-Aguilar, V. M. Alvarado, and C. L. S. Torres, "Control of the air supply subsystem in a PEMFC with balance of plant simulation," *Sustain.*, vol. 9, no. 1, pp. 1–23, 2017.

[15] A. Pilloni, A. Pisano, and E. Usai, "Observer-Based Air Excess Ratio Control of a PEM Fuel Cell System via High-Order Sliding Mode," *IEEE Trans. Ind. Electron.*, vol. 62, no. 8, pp. 5236–5246, 2015.

[16] A. Fly and A. Fly, "Thermal and water management of evaporatively cooled fuel cell vehicles c by."

[17] Z. Liu, J. Chen, S. Chen, L. Huang, and Z. Shao, "Modeling and Control of Cathode Air Humidity for PEM Fuel Cell Systems," *IFAC-PapersOnLine*, vol. 50, no. 1, pp. 4751–4756, 2017.

[18] "Effect of Direct Liquid Water Injection and Interdigitated Flow Field on," 1997.

[19] S. Yun *et al.*, "Numerical analysis on the dynamic response of a plate-and-frame membrane humidifier for PEMFC vehicles under various operating conditions," *Open Phys.*, vol. 16, no. 1, pp. 641–650, 2018.

[20] D. Bhatia, M. Sabharwal, and C. Duelk, "Analytical model of a membrane humidifier for polymer electrolyte membrane fuel cell systems," *Int. J. Heat Mass Transf.*, vol. 58, no. 1–2, pp. 702–717, 2013.

[21] S. Kang, K. Min, and S. Yu, "Two dimensional dynamic modeling of a shell-and-tube water-to-gas membrane humidifier for proton exchange membrane fuel cell," *Int. J. Hydrogen Energy*, vol. 35, no. 4, pp. 1727–1741, 2010.

[22] R. K. Ahluwalia, X. Wang, W. B. Johnson, F. Berg, and D. Kadylak, "Performance of a cross-flow humidifier with a high flux water vapor transport membrane," *J. Power Sources*, vol. 291, pp. 225–238, 2015.

[23] M. Solsona, C. Kunusch, and C. Ocampo-Martinez, "Control-oriented model of a membrane humidifier for fuel cell applications," *Energy Convers. Manag.*, vol. 137, pp. 121–129, 2017.

[24] J. Larminie and A. Dicks, *Fuel cell types*. 2003.

[25] G. Zhang and S. G. Kandlikar, "A critical review of cooling techniques in proton exchange membrane fuel cell stacks," *Int. J. Hydrogen Energy*, vol. 37, no. 3, pp. 2412–2429, 2012.

[26] S. M. H. Hashmi, "Cooling Strategies for PEM FC Stacks," *Von der Fak. Maschinenbau der*, 2010.

[27] S. Yu and D. Jung, "A study of operation strategy of cooling module with dynamic

fuel cell system model for transportation application," *Renew. Energy*, vol. 35, no. 11, pp. 2525–2532, 2010.

[28] J. D. Rojas, C. Kunusch, C. Ocampo-Martinez, and V. Puig, "Control-Oriented Thermal Modeling Methodology for Water-Cooled PEM Fuel-Cell-Based Systems," *IEEE Trans. Ind. Electron.*, vol. 62, no. 8, pp. 5146–5154, 2015.

[29] A. Rabbani and M. Rokni, "Dynamic characteristics of an automotive fuel cell system for transitory load changes," *Sustain. Energy Technol. Assessments*, vol. 1, no. 1, pp. 34–43, 2013.

[30] J. T. Pukrushpan, H. Peng, and A. G. Stefanopoulou, "Control-Oriented Modeling and Analysis for Automotive Fuel Cell Systems," *J. Dyn. Syst. Meas. Control*, vol. 126, no. 1, p. 14, 2004.

[31] A. Z. Weber and J. Newman, *Modeling transport in polymer-electrolyte fuel cells.*, vol. 104, no. 10. 2004.

[32] S. Shi, A. Z. Weber, and A. Kusoglu, "Structure/property relationship of Nafion XL composite membranes," *J. Memb. Sci.*, vol. 516, no. June, pp. 123–134, 2016.

[33] Q. Yan, H. Toghiani, and H. Causey, "Steady state and dynamic performance of proton exchange membrane fuel cells (PEMFCs) under various operating conditions and load changes," *J. Power Sources*, vol. 161, no. 1, pp. 492–502, 2006.

[34] B. Larbi, W. Alimi, R. Chouikh, and A. Guizani, "Effect of porosity and pressure on the PEM fuel cell performance," *Int. J. Hydrogen Energy*, vol. 38, no. 20, pp. 8542–8549, 2013.

[35] A. A. Abd El Monem, A. M. Azmy, and S. A. Mahmoud, "Effect of process parameters on the dynamic behavior of polymer electrolyte membrane fuel cells for electric vehicle applications," *Ain Shams Eng. J.*, vol. 5, no. 1, pp. 75–84, 2014.

[36] I. S. Hussaini and C.-Y. Wang, "Transients of Water Distribution and Transport in PEM Fuel Cells," *J. Electrochem. Soc.*, vol. 156, no. 12, p. B1394, 2009.

[37] P. Moraal and I. Kolmanovsky, "Turbocharger Modeling for Automotive Control Applications," *SAE Tech. Pap. Ser.*, vol. 1, no. March 1999, 2010.

[38] J.-P. Jensen, A. F. Kristensen, S. C. Sorenson, N. Houbak, and E. Hendricks, "Mean Value Modeling of a Small Turbocharged Diesel Engine," *SAE Tech. Pap. Ser.*, vol. 1, 2010.

[39] M. Casey and C. Robinson, "A Method to Estimate the Performance Map of a Centrifugal Compressor Stage," *J. Turbomach.*, vol. 135, no. 2, p. 021034, 2012.

[40] F. P. Incropera, D. P. DeWitt, T. L. Bergman, and A. S. Lavine, *Fundamentals of*

Heat and Mass Transfer 6th Edition. 2007.

[41] "1." .

[42] D. Jung and D. N. Assanis, "Numerical Modeling of Cross Flow Compact Heat Exchanger with Louvered Fins using Thermal Resistance Concept," *SAE Tech. Pap. Ser.*, vol. 1, no. July 2016, 2010.

[43] Y. J. Chang and C. C. Wang, "A generalized heat transfer correlation for louver fin geometry," *Int. J. Heat Mass Transf.*, vol. 40, no. 3, pp. 533–544, 1997.

[44] Y. Wang and C. Y. Wang, "Dynamics of polymer electrolyte fuel cells undergoing load changes," *Electrochim. Acta*, vol. 51, no. 19, pp. 3924–3933, 2006.

[45] J. H. Jang, W. M. Yan, and C. C. Shih, "Effects of the gas diffusion-layer parameters on cell performance of PEM fuel cells," *J. Power Sources*, vol. 161, no. 1, pp. 323–332, 2006.

[46] J. Cho, H. S. Kim, and K. Min, "Transient response of a unit proton-exchange membrane fuel cell under various operating conditions," *J. Power Sources*, vol. 185, no. 1, pp. 118–128, 2008.

[47] P. Kahroba, I. Mirzaee, and H. Shirvani, "The Influence of Membrane thickness on the PEM Fuel Cell Operation," no. October, 2009.

[48] R. Huizing, "Summary for Policymakers," *Clim. Chang. 2013 - Phys. Sci. Basis*, vol. 1, pp. 1–30, 2015.

[49] C. Dalet, O. Lottin, G. Maranzana, and M. Diny, "Criteria for Characterizing the Performances of Fuel Cell Humidifiers: Theoretical Approach and Experimental Results," no. September 2016, pp. 309–316, 2009.

[50] "New_European_Driving_Cycle @ en.wikipedia.org." .

[51] "Ece_Eudc @ Www.Dieselnet.Com." .

[52] A. Kabza, "Just another Fuel Cell Formulary," pp. 1–84, 2015.

List of Figures

List of Tables